Prompt Photon Production in Deep Inelastic Scattering at HERA

Mairi Siobhan Bell

Department of Physics & Astronomy
University of Glasgow
Glasgow

Thesis submitted for the degree of
Doctor of Philosophy

May 2003

Abstract

First measurements of cross sections for isolated prompt photon production in deep inelastic *ep* scattering are presented for photon virtualities above $35 GeV^2$. The measurements were made with the ZEUS detector at HERA using an integrated luminosity of 121 pb^{-1}. A signal for well-isolated photons in the transverse energy and pseudorapidity range $5 < E_T^\gamma < 10 GeV$, $-0.7 < \eta^\gamma < 0.9$ was observed, after the subtraction of the background from neutral mesons. Cross sections are presented for inclusive prompt photons and for those accompanied by one jet in the range $E_T^{\rm jet} \geq 6 GeV$, $-1.5 \leq \eta^{\rm jet} < 1.8$. Theoretical calculations made to $O(\alpha^2 \alpha_S)$ describe reasonably well the measured photon plus jet cross sections.

To Neil

Acknowledgements

There are many people without whom I could not have undertaken and completed the work in this thesis. In particular, I am grateful to PPARC for funding my work and giving me the opportunity to be involved with this project.

I would like to thank my supervisors, David Saxon and Peter Bussey for all the time they have invested in the work and for all the patient help and encouragement I have received throughout my PhD. I would also like to thank Anna Lupi for all her help on getting some of programs working.

While at DESY I have been greatly helped by the co-ordinators of the QCD physics group and in particular I would like to mention all the help received from Mark Sutton and Sergei Chekanov.

For many helpful discussions and suggestions as well their invaluable work on preparing the theoretical plots used, I would like to express my gratitude to Gustav Kramer and Hubert Spiesberger.

I am also grateful to Torbjorn Sjostrand and Gunnar Ingelman for help in producing a convincing prompt photon sample from the PYTHIA program. I'd also like to thank John Loizides for giving me a program to generate these events.

I have also been greatly helped by the ZEUS group at Glasgow and the wider UK ZEUS group.

Thesis Outline

This thesis extends the study of prompt photon production into the new area of deep inelastic electron-proton scattering, building on the previous extensive measurements made in the photoproduction region of ep scattering and observations of prompt photons at other detectors.

Chapter 1 provides a brief introduction to the world of prompt photons, and includes a summary of their interesting qualities and a description of current prompt photon studies. Chapter 2 extends this introduction giving more details of the production mechanisms and necessary theory, both for HERA physics and the prompt photon process itself.

The next chapter is a self-contained summary of the main features of the HERA accelerator and the ZEUS detector, providing some useful background detail and dwelling in more depth on those detector features which are particularly relevant to the analysis.

Chapter 4 begins the main body of new work on which this thesis is based. The chapter discusses in chronological order the event selection necessary to obtain the purest sample of prompt photon events available. Some methods were retained from the photoproduction analysis, most notably the use of the ELEC5 electron finder to look for the prompt photons but new techniques had to be developed to take account of the presence of both an electron and a photon.

Chapter 5 desribes the background subtraction performed to statistically extract the final prompt photon event sample from the neutral meson background using, virtually unaltered, the subtraction method developed in the photoproduction analysis.

Chapters 6 and 7 present the results of the analysis with cross section measurements of prompt photon production at ZEUS after correction to hadron level. Comparisons to standard Monte Carlo models and, where applicable, theoretical calculations are also presented.

Chapter 8 summarises the study undertaken and discusses the results obtained in some greater detail, presenting the conclusions reached.

An Appendix which summarises the use of Monte Carlo in the analysis is included, giving details of which types of Monte Carlo models are used and under which circumstances.

The work described in Chapters 4 to 8 is original work performed by this author. It includes the use of tools and methods developed by others.

Contents

List of Figures

List of Tables

Chapter 1

Introduction

Frequently, in studies of high energy physics involving quantum chromodynamics, QCD, effects, both theorists and experimentalists have to deal with the difficult and as yet not fully understood process of hadronisation; i.e. the process whereby a coloured object such as a quark or gluon which has been created in a hard scattering QCD subprocess becomes a shower of colourless hadrons prior to final state observation.

Various models exist to describe and parameterise this process and are used in Monte Carlo models to enable a more realistic description of data, but the basic mechanism remains something of a mystery. Thus, there is a loss of information between the hard scattering subprocess and the final state as observed and measured.

Conversely to these coloured objects any photons emitted in a hard scatter will proceed unaltered directly to the detector, carrying unchanged information relating to the original scatter. These photons reach the detection point rapidly and without interaction and are known as 'prompt' photons. As a result these prompt photons have been investigated in many experiments and by many groups of theorists.

The prompt photon area of study is a rich and diverse field with investigations undertaken by many large experiments and several different groups of theorists.

These photons provide a unique ability to study in the final state particles which have actually participated in hard scattering subprocesses and carry unaltered information about the scattering process. Hadronisation effects present in the study of prompt photons are significantly reduced from jet analyses.

1.1 Current Prompt Photons Studies

In previous years prompt photons have been widely studied in many areas of high energy physics. Observations and measurements have been made at both fixed target experiments and lepton colliders. Several experiments currently underway are involved in furthering the study of prompt photon behaviour including HERA, the Tevatron and RHIC.

1.1.1 Prompt Photons at Hadron Colliders

Tevatron

Isolated prompt photon production has been observed in hadron-hadron collisions at the Tevatron by both the CDF and D0 collaborations, [1]-[5]. Direct prompt photon production has been observed by the CDF collaboration and compared to NLO QCD predictions. Initial problems with the agreement were improved by additional gluon radiation in the theoretical model. Inclusive photon, photon plus one jet and photon plus two jet processes have also been studied at the Tevatron. Prompt photon production is important at hadron colliders for several reasons. The energy of the photon can be well measured compared to jet energies which provides a useful tool to improve understanding of QCD. It is also possible to use prompt photon measurements to investigate the gluon distribution inside the proton. The photon plus one jet process places constraints on this distribution. Photons are also a significant background to new physics.

Prompt Photons at RHIC

The Relativistic Heavy Ion Collider, RHIC has been operating at the Brookhaven National Laboratory since 2000. The accelerator collides beams of gold ions with the primary aim of detecting new physics in the form of Quark Gluon Plasma. Photons are produced in large numbers in RHIC collisions, with prompt photons from partonic hard scattering processes providing a large background to the signatures of new physics [6].

Prompt photons are also studied in polarised pp collisions by the PHENIX collaboration at RHIC where it is hoped they will provide a probe of the gluon density in the proton [7].

Large Hadron Collider

It is expected that the knowledge and expertise gained from prompt photon studies will play an important role in physics studies at the Large Hadron Collider, LHC, where photons are a significant background to searches for new physics and Higgs decays. The diphoton background is one of the most difficult to deal with in searching for Higgs decays.

1.1.2 Prompt Photons at HERA

Prompt photon production has been observed in electron-proton scattering at HERA by both the ZEUS, [8]-[10] and H1, [11] collaborations. Previous work has concentrated on the photoproduction region, where the statistics are high and the prompt photon process is easier to detect.

Results showing differential cross sections with respect to the pseudorapidity and transverse energy of the prompt photon have been presented. Prompt photon studies at ZEUS have been expanded to examine the possible effects of intrinsic momentum in initial state hadrons. Recent measurements indicate the presence inside the proton of this intrinsic k_T and prompt photons provide a means to investigate the issue.

Until recently, limited statistics have prevented the extension of the study of prompt photons into the higher Q^2 deep inelastic region of HERA physics. However, data gathered by the ZEUS detector during the running of HERA I between 1996 and 2000 now allow initial observations of the process to be made and the first measurements to be produced. The prompt photon process has never been measured in deep inelastic *ep* scattering before.

To further motivate the study of this unexplored region of HERA physics, theoretical calculations now exist describing the behaviour of prompt photon plus jet production at higher Q^2 values and in a kinematic regime suitable for HERA analysis.

Chapter 2

Theory

The HERA accelerator is the world's first and only electron-proton accelerator and therefore provides a unique opportunity to study inelastic collisions and the internal structure of the proton as well as giving an ideal testing ground for perturbative Quantum Chromodynamics, QCD. QCD is the study of the strong force of nature, which governs the interactions between particles carrying colour charge, quarks and gluons. The gluon is the mediating particle for the strong force, and has a role analagous to that of the photon in electromagnetic interactions.

The type of interaction is a unique opportunity to study the internal quark-gluon structure of the proton and by measuring cross sections of different event types allows theoretical perturbative QCD calculations to be tested.

Interactions in the ZEUS detector are asymmetric scattering events between electrons[1] of energy $27.5GeV$ and protons of energy $920GeV$, carried out via a virtual exchanged boson.

2.1 Lepton Nucleon Scattering

In the most general situation interactions between the opposing particles, the electron and the proton, occur via the exchange of a virtual boson. In the case

[1]The word electron is used here to mean either electron or positron

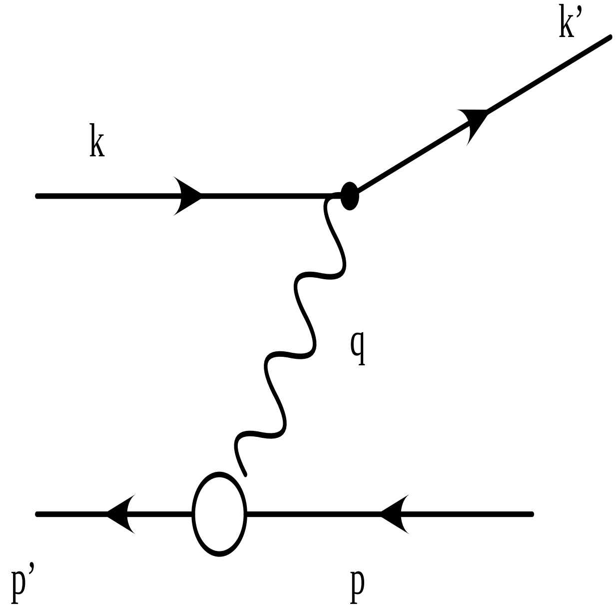

Figure 2.1: *Elastic ep scattering*

of asymmetric scattering like this the larger heavier proton is a target which is probed by the pointlike electron. In most cases the energy of the exchanged boson is not sufficient to break up the proton and the interaction is an elastic scatter. Elastic *ep* scattering is shown in Figure (2.1).

The exchange boson has a momentum $q = k' - k$ where k is the momentum of the initial state electron and k' is the momentum of the final state electron. For neutral current, NC, events the exchange boson is a virtual photon or a Z^0, although Z^0 exchange only becomes important at $Q^2 \approx M_Z^2$ where Q^2 is equal to the negative square of the momentum of the exchange boson, i.e. $Q^2 = -q^2 = (k' - k)^2$. For photon exchange, Q^2 is known as the virtuality of the exchanged photon.

As Q^2 increases the exchanged boson moves off the mass shell and becomes more and more virtual. This virtual boson has the ability to resolve the internal quark structure of the proton, and can even knock one quark completely out of the proton. The proton here does not interact as a single unit. The resolved

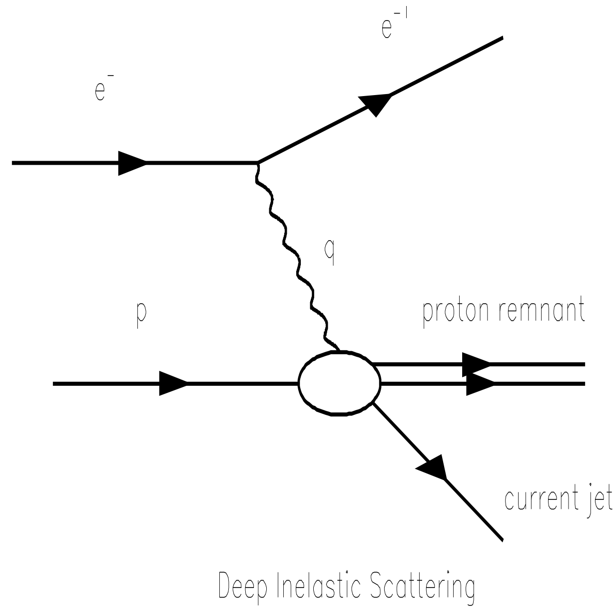

Figure 2.2: *Deep Inelastic Scattering in ep Collisions*

quark scatters off the boson and the proton remnant continues largely undeviated from its original direction. During electron-proton interactions at HERA, values of Q^2 between 0 and $40,000 GeV^2$ are currently achievable.

When the exchange boson interacts with a quark within the proton and the proton is broken up the process is known as deep inelastic scattering, DIS. The lowest order process, $ep \rightarrow eX$ is shown in Figure (2.2). The final state quark hadronises to a jet of particles, as coloured objects cannot exist independently.

Hence there are two types of scattering which can occur - elastic and inelastic. Elastic scattering occurs mostly at low Q^2. No quarks are resolved from the proton. The other type of scattering is known as Deep Inelastic Scattering, DIS, and occurs at high Q^2 values where one quark (or gluon) is resolved from the proton. The region of Q^2 close to 0 is known as photoproduction and extensive studies of prompt photon production have been performed in this region.

2.2 Kinematic Variables at HERA

Electron-proton scattering events are characteristically described in terms of their Q^2 and x values, where Q^2 is as previously defined and x is the dimensionless Bjorken scaling variable. The variable x is defined by the relationship in Equation (2.1).

$$x = \frac{Q^2}{sy} \tag{2.1}$$

In Equation (2.1), s is the total centre of mass energy squared and y is the fraction of energy transfer to the proton in its rest frame, defined in Equations (2.2) and (2.3).

$$s = (k + p)^2 = 4E_e E_p \tag{2.2}$$

$$y = \frac{p.q}{p.k} \tag{2.3}$$

In Equations (2.2) and (2.3) k and p are the initial state electron and proton 4-momenta, k' is the final state electron 4-momentum and $q = k - k'$. The variable, x, can be thought of as the fraction of the initial state proton momentum carried by the struck parton.

The Z-axis in ZEUS is along the beam pipe with positive Z in the direction of proton travel and the polar angle, θ, measured relative to positive Z. This means that an undeflected electron will proceed at $\theta = 180°$[2]. The kinematic parameters of the event can be calculated from either the scattered electron or the hadronic jet. The electronic system is most important as in DIS events there is always an easily measured electron present in the calorimeter which will lead to much more accurate conclusions than starting from the poorly defined quark jet,

[2]Further details of the ZEUS coordinate scheme can be found in Section 3.3.1.

whose scattering angle and energy cannot be as well known. However, in order to suppress calorimeter noise, the variable y as reconstructed using the Jacquet-Blondel method is used as it provides the best estimate of y at low values. This is defined in Equation (2.4).

$$y_{JB} = \frac{\Sigma_i E_i - p_{zi}}{2E_e} \tag{2.4}$$

In Equation (2.4) the sum runs over all the final state particles in the hadronic system.

Substituting for the 4-momenta of the particles and rearranging the equations leads to expressions for Q^2 and y in terms of the scattered electron energy, E'_e and scattering angle, θ_e. These are given in Equations (2.5) and (2.6).

$$Q^2 = 2E_e E'_e (1 + \cos\theta_e) \tag{2.5}$$

$$y = 1 - \frac{E'_e}{2E_e}(1 - \cos\theta_e) \tag{2.6}$$

Typical variables which are used extensively in ZEUS analyses in general and specifically in this present work are the transverse energy and pseudorapidity of particles. The transverse energy is the energy perpendicular to the original beam direction and is given by Equation (2.7).

$$E_T = E * \sin\theta \tag{2.7}$$

The pseudorapidity of a particle is calculated from its polar angle and is a Lorentz invariant quantity making it desirable to use. It is defined in Equation (2.8).

$$\eta = -\ln(\tan(\theta * 0.5)) \tag{2.8}$$

In the ZEUS detector a pseudorapidity of 0 is at 90°, with positive values in the forward region and negative values in the rear direction.

2.3 DIS and the Structure Function

Formally, the differential cross section for deep inelastic *ep* scattering as a function of x and Q^2 can be written as in Equation (2.9).

$$\frac{d^2\sigma^{e^\pm p}}{dQ^2dx} = \frac{2\pi\alpha^2}{xQ^4}\{[1+(1-y)^2]F_2(x,Q^2) \mp [1-(1-y)^2]xF_3(x,Q^2) - y^2F_L(x,Q^2)\} \tag{2.9}$$

The cross section expressed in Equation (2.9) involves three structure functions, F_2, F_3 and F_L of x and Q^2. Measurements of these structure functions as a function of Q^2 provides information on the internal quark-gluon structure of the proton, analagous to the role played by form factors in elastic scattering providing information about the proton size.

At the typical HERA range of $Q^2 << M_Z^2$ the contribution from xF_3 is negligible. Commonly, $F_L = 0$ is used. Thus, Equation (2.9) can be expressed in the simplified form given in Equation (2.10).

$$\frac{d^2\sigma}{dQ^2dx} \propto \frac{1}{Q^4}F_2(x,Q^2) \tag{2.10}$$

The cross section depends inversely on Q^4 leading to a large fall in the number of events found as Q^2 increases.

At very low values of Q^2 the exchanged photon sees only the size of the proton. Then as Q^2 is increased the structure the photon begins to detect the structure within the proton. The momentum of the exchanged boson can be increased until it is high enough to resolve one of the quarks within the proton. This effect can be approximated to the boson scattering off a free quark. The free quark is a point-like entity hence the structure function is independent of Q^2. This is known as *Bjorken Scaling*. If anything other than a single quark is resolved the structure function becomes dependent on Q^2 again.

The structure functions describing the proton are calculated from the experimentally measured quantities Q^2 and x. The measured quantities Q^2 and x may not be accurate so reconstruction techniques have to be applied to these variables to gain accurate information on the structure.

2.4 Neutral Current Deep Inelastic Scattering

In a typical NC DIS event one would expect to find the scattered electron somewhere in the calorimeter, most likely in the rear direction at a small angle from the initial direction of the incoming electron. Also one would expect the scattered quark to hadronise and a jet to be detected in the calorimeter. The signature of a jet of hadronic particles is a significant amount of hadronic energy in the calorimeter and a number of tracks pointing towards the energy deposit. In the particular case of prompt photon production the outoing quark emits a photon before hadronisation occurs. This photon is isolated both from the quark and from the scattered electron. The final state in the calorimeter consists of at Leading Order, LO, the scattered electron, an isolated photon and a hadronic jet. At Next-to-Leading Order, NLO, there may be additional jets from gluons present.

2.5 Prompt Photon Production

'Prompt' photons are high transverse energy final state photons which are emitted directly from the hard scattering process. They are of interest primarily for two reasons. They are easier to detect and measure cleanly than hadronic jets, and the final state photon is a particle which arrives in the detector having taken part in the actual scattering process and so can provide direct information on the

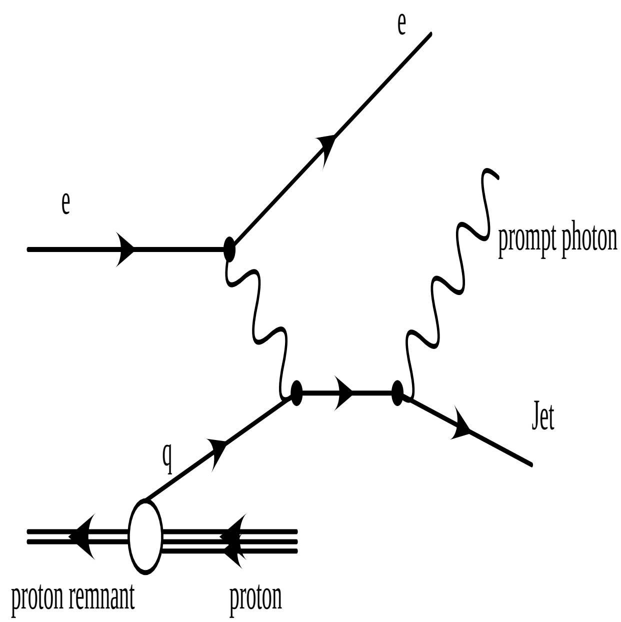

Figure 2.3: *Prompt photon production in ep collisions*

process.

The production of prompt photons in deep inelastic *ep* collisions at HERA is shown in Figure (2.3). The incoming lepton emits a virtual photon which interacts with a quark emitted from the proton in a hard scattering process. A quark and photon are emitted in the final state. In deep inelastic events no structure is resolved within the exchanged photon and therefore no information on the photon partonic structure is required.

The hard scattering subprocess, $\gamma^{*}+q \rightarrow \gamma+q$, which results in the production of high transverse energy final state photons is shown at leading order in Figure (2.4). A highly virtual photon interacts with a quark emitted from the proton in a hard scatter which produces an outgoing photon.

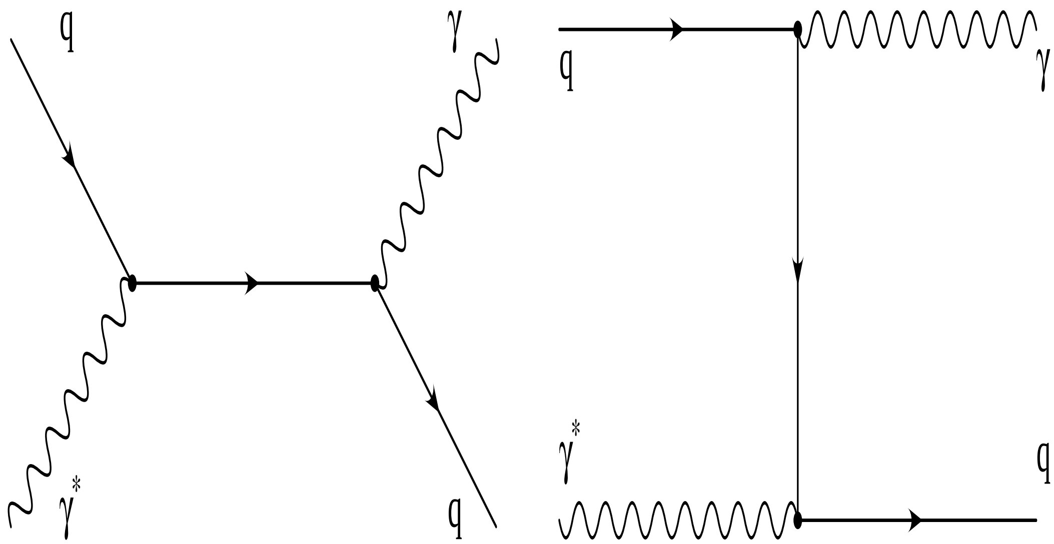

Figure 2.4: *Direct prompt photon production at leading order*

2.6 Background Processes

Photons identified as prompt photons can arise from other processes besides that of interest and events with isolated neutral mesons detected in the final state may also be misidentified as prompt photon events.

2.6.1 Initial and Final State Radiation

The majority of photons which are detected in the calorimeter come from beam gas or cosmic ray interactions which are suppressed by basic trigger requirements to select only events arising from electron-proton scattering. Of the processes remaining, those which contribute most significantly to the volume of photons detected are events with initial and final state radiation. In such events, a photon is radiated by either the incoming electron (Initial State Radiation, ISR) or the scattered electron (Final State Radiation, FSR). The cross section for these events is several orders of magnitude larger than for prompt photon events and the final state is often the same with an electron, a photon and a jet being detected. Therefore it is important to understand the nature of ISR and FSR events and

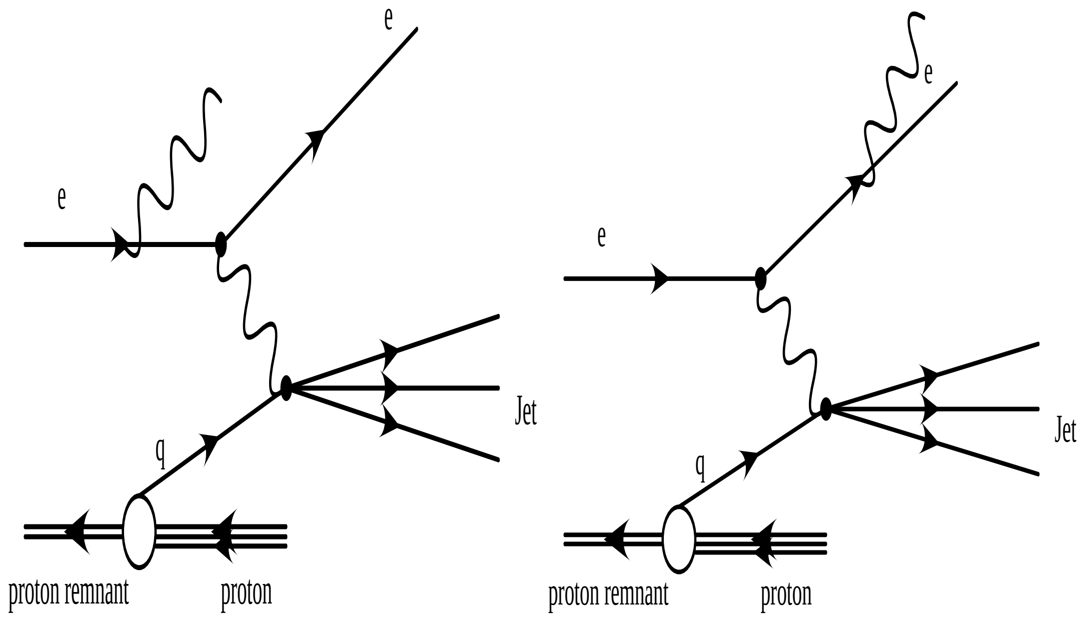

Figure 2.5: *Photons produced from a) the incoming electron line and b) the scattered electron line in NC DIS events*

establish the effectiveness of suppression cuts and the possible contamination effect.

Isolated direct photons are produced from either the quark line, quarkonic radiation, or from the electron line, leptonic radiation. It is expected that photons produced in ISR or FSR processes will usually be produced nearly collinear to the parent electron, so can in principle be suppressed by strict isolation criteria, in particular the distance between the electron and the photon. Initial and final state radiative processes in neutral current DIS events are shown at lowest order in Figure (2.5). Similarly to the prompt photon process the cross section for the process is $O(\alpha^2)$ times the main process.

These background processes are investigated using neutral current DIS Monte Carlo events with radiative corrections to obtain samples of ISR and FSR to see the typical event topology. The Monte Carlo used here is DJANGOH, which uses HERACLES and LEPTO. This is described in Appendix A. The total number of events generated with $Q^2 > 35GeV^2$ is 100,000 and of these the numbers which contained initial or final state leptonic radiation are summarised in Table (A.4).

The pseudorapidity and transverse energy distributions of initial and final state photons are shown in Figure (2.6).

It is observed in Figure (2.6) that photons from both ISR and FSR events are emitted with a pseudorapidity spectrum very strongly peaked in the backward region. This confirms prior suspicions that the photons would be emitted at a polar angle which does not greatly deviate from that of the parent electron. In Neutral Current events the Q^2 distribution can be loosely related to the scattered electron polar angle, with most scattered electrons ending up in the Rear Calorimeter, RCAL, at low Q^2 values. By imposing restrictions so that the electron is in the RCAL and the photon is in the Barrel Calorimeter, BCAL, the contribution from this process can be greatly suppressed. These detector components cover different angular ranges. Further description of the ZEUS calorimeter can be found in Chapter 3. It is also observed from Figure (2.6) that these photons are typically of very low transverse energies, significantly below the $5GeV$ cut imposed later on the prompt photon candidates.

The dominant selection cuts to be used in the analysis are applied to these hadron level events to ascertain the possible numbers of events of this type which may survive selection cuts. The list of cuts applied includes those relating to the energy and angle of the photon and electron and the separation between them. Without applying any further cuts the effect of the ISR and FSR processes is virtually removed with no simulated events surviving the cuts. However, the cross section for emission of photons from the electron line is much higher than photon production from the quark line so there still remains a significant possible contribution to the measured result. The effect of ISR and FSR is also taken into account in the NLO theory calculations of the $(\gamma + jet)$ process.

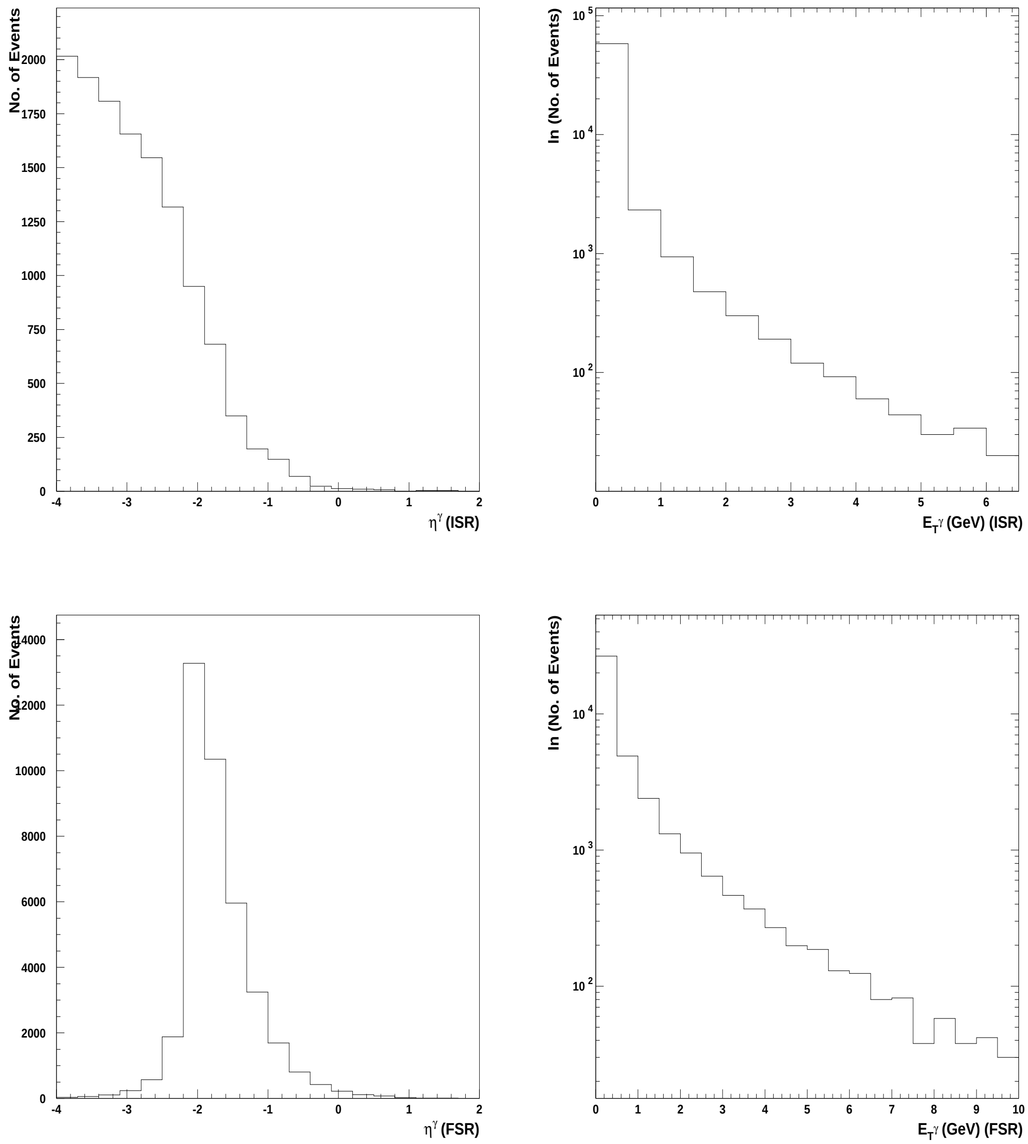

Figure 2.6: *Pseudorapidity and transverse energy distributions of photons from initial and final state radiation. a)* $\eta^{\gamma}(ISR)$ *b)* $E_T^{\gamma}(ISR)$ *c)* $\eta^{\gamma}(FSR)$ *d)* $E_T^{\gamma}(FSR)$

2.6.2 Neutral Meson Background

Events with jets in the final state can produce a significant background to prompt photon searches via two distinct mechanisms. The first situation is where events in which isolated neutral mesons such as π^0 or η are found in the final state and are misidentified as prompt photon events. Such events cannot be discounted as negligible but they can be somewhat suppressed by appropriate cuts, particularly on the energy surrounding the photon and later removed with a statistical extraction procedure.

2.6.3 Photons from Fragmentation

Photons can also arise from fragmentation processes occuring within jets. Thus, photons can be detected in the final state of any dijet process, should fragmentation have occured. As with the neutral mesons found in this type of event, the photons detected are generally produced nearly collinear to other particles from the surrounding hadronisation activity and will therefore be typically close to energy which is unassociated to the photon itself and possibly also to nearby tracks. Example of processes which may contribute to these events are the hard scattering subprocesses shown in Figure (2.7).

Both neutral meson misidentification and fragmentation processes can be suppressed by applying isolation cuts to the photon candidates, restricting the presence of tracks and unassociated energy near the photon.

2.6.4 QED Compton and Deeply Virtual Compton Scattering

Two further groups of events exist which have an electron and a possibly isolated photon in the final state. These are QED Compton events, shown in Figure (2.8) and Deeply Virtual Compton Scattering, DVCS, shown in Figure (2.9).

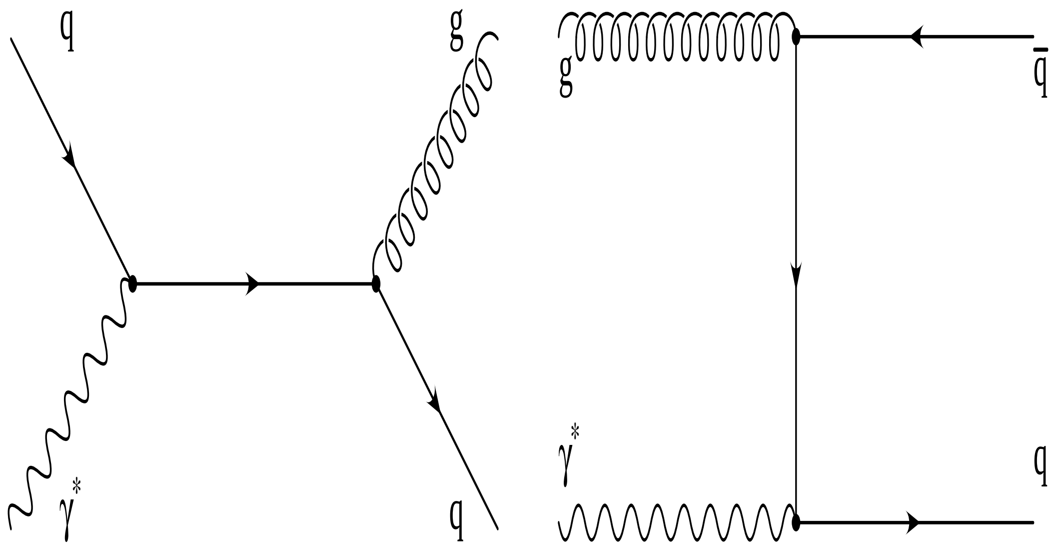

Figure 2.7: *Jets produced in these dijet events can fragment and yield photons in the final state.*

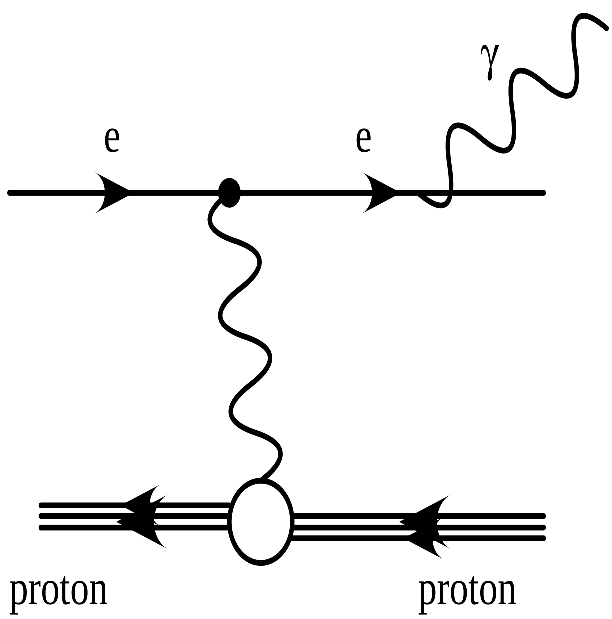

Figure 2.8: *Production of photons in QED Compton events*

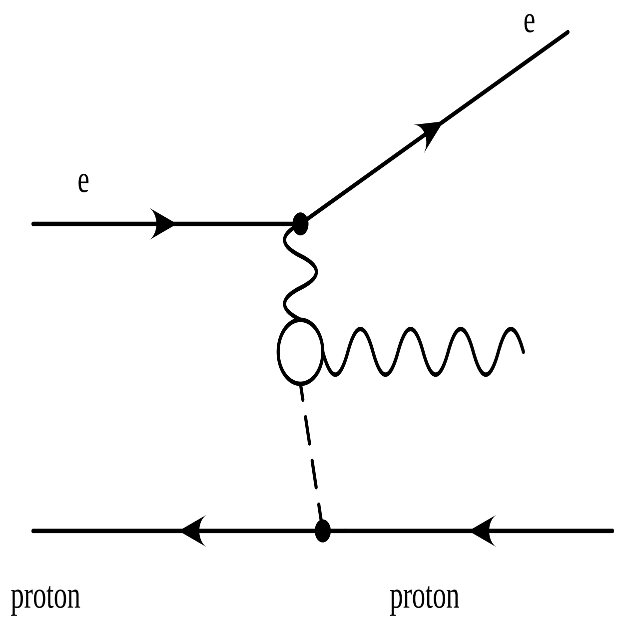

Figure 2.9: *Production of photons in Deeply Virtual Compton Scattering*

QED Compton events are basic electron-photon elastic scattering, as is shown in Figure (2.8) and there is no final state hadronic activity.

Figure (2.9) shows that the final state of DVCS events is an electron, a photon and no hadronic activity. In DVCS the photon is produced through the diffractive scatter of a virtual photon with the proton. Both QED Compton and DVCS events can be easily suppressed by demanding the presence of some hadronic activity in the calorimeter.

2.7 Theory Calculations at Order $(\alpha^2\alpha_s)$

The production of a hard final state prompt photon at $Q^2 > 35GeV^2$ accompanied by only 1 jet has been calculated by Gehrmann-de-Ridder, Kramer and Spiesberger [12] at next to leading order, ie order $O(\alpha^2\alpha_s)$. The calculations are based on the HERA kinematic regime and as such are ideal for comparison to data measurements. At this order, processes with an additional gluon must be

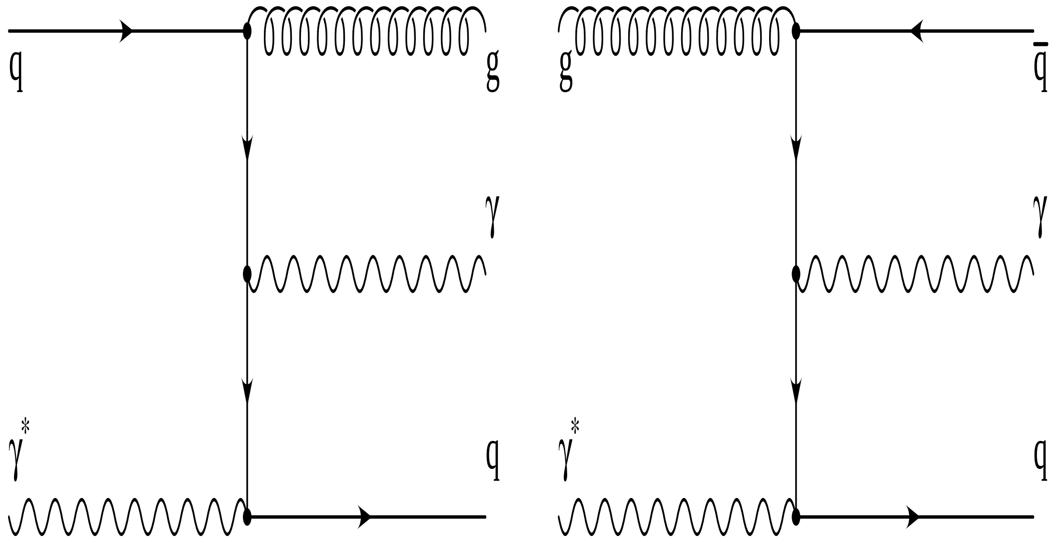

Figure 2.10: *Prompt photon production at order $O(\alpha^2\alpha_s)$ where processes with an additional gluon are considered.*

considered. The calculations are performed at the parton level with no hadronisation applied. Examples of the prompt photon subprocess at this order are shown in Figure (2.10).

To provide better agreement to data these NLO corrections are usually included in theoretical calculations. This is an important correction because although the final state may actually be a photon plus 2 jets, these individual jets may not be resolved separately in the detector leaving the process exactly resembling the LO process experimentally.

Theoretical distributions of the final kinematic description of the photon and jet are shown in Figure (2.11). The pseudorapidity and transverse energy are shown for both the photon and the jet.

It can be seen from Figure (2.11) that the prompt photon pseudorapidity spectrum is peaked towards negative values, corresponding to the more backward region of the ZEUS detector and the jet pseudorapidity spectrum is peaked in the forward direction. The transverse energy distribution of the prompt photon

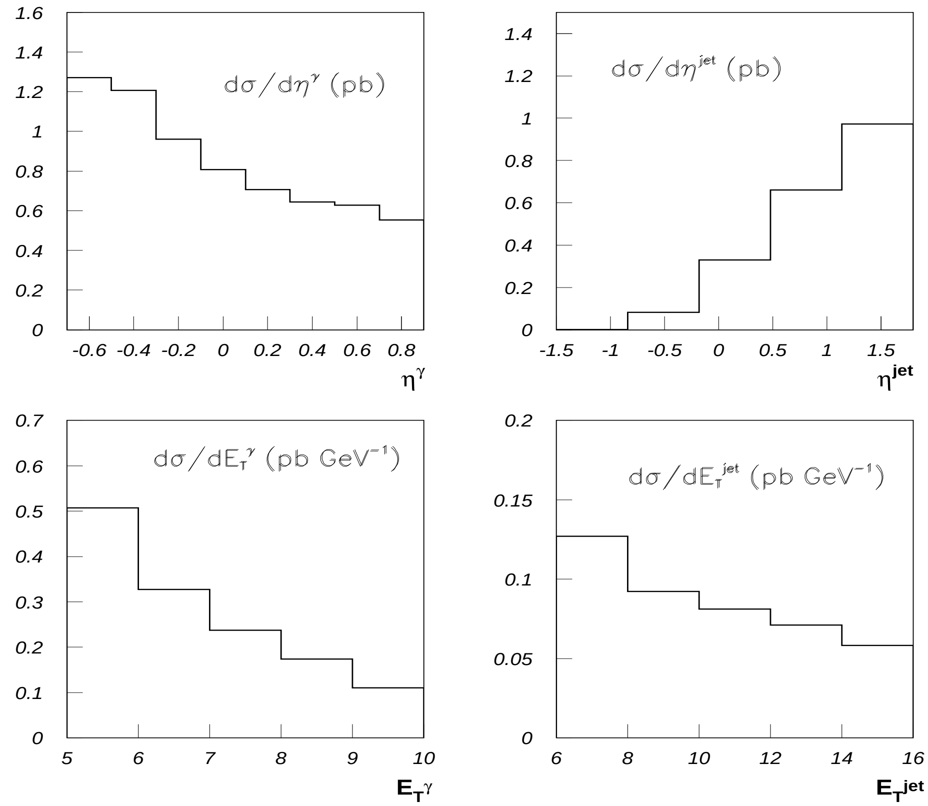

Figure 2.11: *Calculations of* $(\gamma + 1) + 1$ *final state at order* $\alpha^2\alpha_s$ *by G. Kramer and H. Spiesberger in the HERA laboratory frame. The notation* $(\gamma+1)$ *indicates that the final state is a photon plus one jet. The further + 1 refers to the proton remnant.*

displays a steeper gradient than that of the jet and is more strongly peaked at lower E_T values. In previous prompt photon studies in photoproduction at HERA a similar rapidity distribution has been observed, showing an enhancement to prompt photon production in the rear direction.

These calculations are from a private communication [13] based on the results from the published paper, DESY 00-039 [12].

2.8 Monte Carlo

It is necessary to use Monte Carlo simulations several times in order to perform the following analysis. Further details on all Monte Carlo used can be found in Appendix A.

Chapter 3

The HERA Accelerator and ZEUS Detector

3.1 The HERA accelerator

The Hadron Elektron Ring Anlage, HERA, accelerator, located at the Deutsches Elektron Synchotron, DESY, site in Hamburg, in Northern Germany is the world's only lepton-hadron collider, which makes it uniquely able to probe the internal quark-gluon structure of the proton and photon and discover more about the strong force and QCD.

The accelerator was constructed between 1984 and 1990, and measures 6.3km around its circumference. Four separate experiments are located around the ring in four large experimental halls which are at a depth of around 25 metres. There are two experiments studying collider physics, ZEUS and H1 which are situated at the interaction points where the separate lepton and hadron beams are brought together. Two further experiments, HERMES, which looks at polarisation effects using the lepton beam and a fixed target, and HERA-B, which uses the hadron beam to study CP-violation in B meson decay, are also situated on the HERA ring.

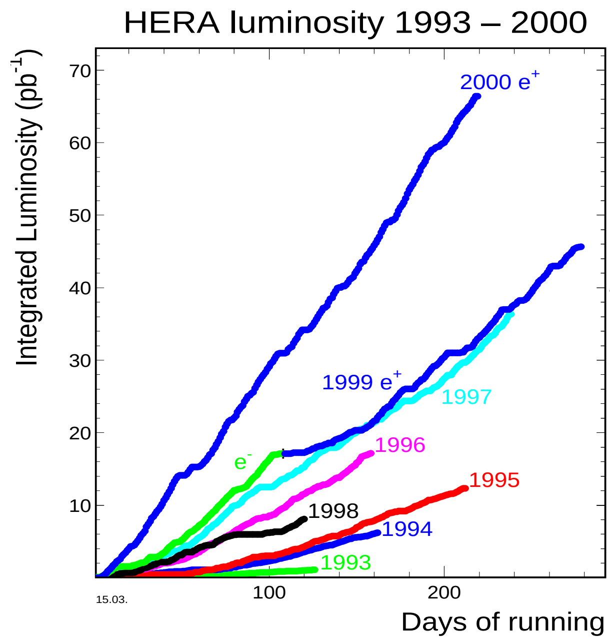

Figure 3.1: *Integrated Luminosity provided by HERA between 1993 and 2000*

The accelerator uses a proton beam and can use either electrons or positrons as the lepton source.

During the periods of running from 1993 until 2000 HERA has provided an integrated luminosity as shown in Figure (3.1).

During the period of data taking used for this work, 1996-2000, the ZEUS detector collected $121.3pb^{-1}$ of data. This was largely accumulated with a positron beam, apart from a period between 1998 and 1999 where an electron beam was used and $16pb^{-1}$ of data were collected.

3.2 Accelerator Operation

HERA is a two ring accelerator with the protons and electrons kept separately in different storage rings and only brought together at the interaction points. At these points, electrons of energy 27.5GeV are allowed to collide with protons of

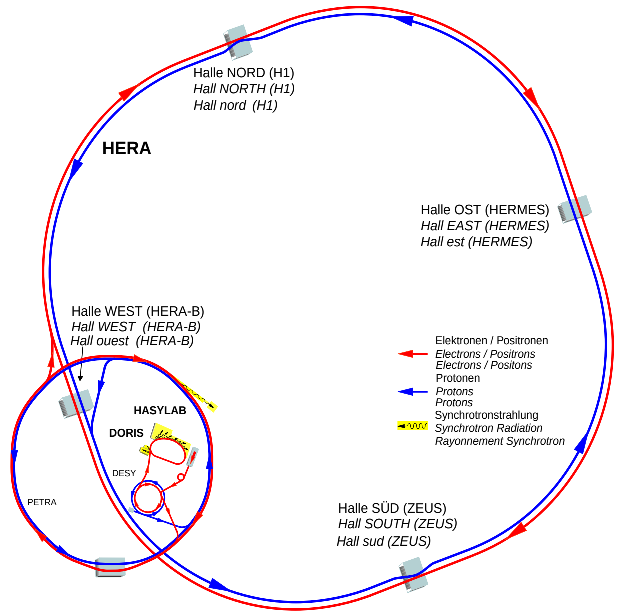

Figure 3.2: *The HERA Accelerator Complex showing the main accelerator rings*

energy 820 GeV (1996-1997) or 920GeV (1998-2000).

A schematic diagram of the accelerator complex is shown in Figure (3.2) which shows the main accelerator ring and a further smaller accelerator ring, PETRA, and indicates the position of the four experiments around the ring.

3.2.1 Beam Injection

Electrons and protons are accelerated separately in stages before being injected into the main ring in bunches which are then accelerated up to their interaction energies. Positrons are accelerated to 500 MeV in a linear accelerator and held in a storage ring, PIA, Positron Intesity Accumulator. When a bunch of current 60 mA has been accumulated, it is transferred to DESY II. In DESY II the positrons are accelerated to 7.5 GeV before transfer to PETRA. In PETRA 70 bunches of positrons are collected and accelerated to 14 GeV and then the bunches are finally injected into HERA before being accelerated to their maximum energy of 27.5 GeV.

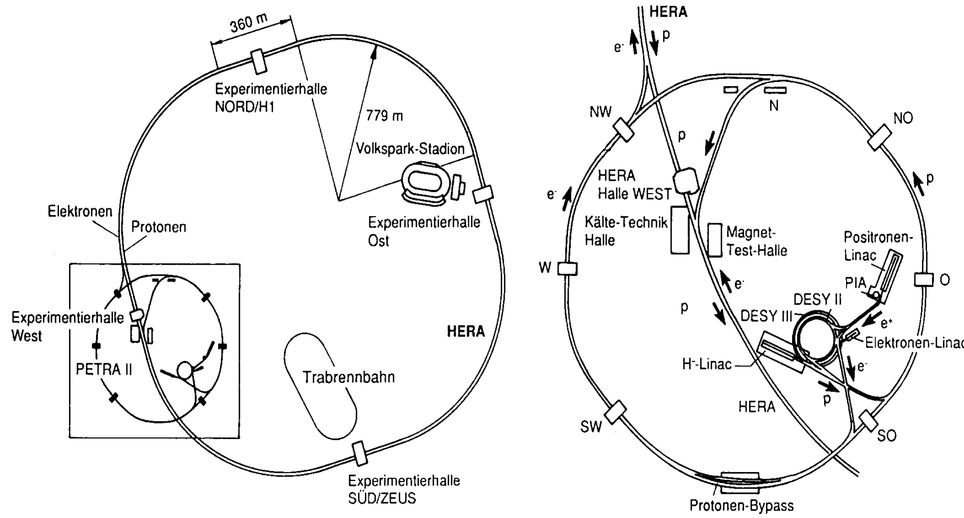

Figure 3.3: *The HERA injection system, showing on the left the large accelerator, and on the right an enlarged view of the pre-accelerator section.*

The first stage of proton acceleration also takes place in a linear accelerator where 50 MeV H^- ions are stripped of their charge and injected into DESY III. 11 bunches are collected which already have the necessary final spacing are accelerated to 7.5 GeV and injected into PETRA II. PETRA II can hold up to 70 bunches which are then accelerated to 40 GeV. After this injection to the HERA ring occurs and the protons are accelerated to their final energies of 820(920) GeV.

The complete HERA injection system is shown in detail in Figure (3.3).

Electron acceleration is carried out via conventional magnets but proton acceleration is done using superconducting magnets, cooled using liquid helium.

HERA holds a maximum of 210 electron and proton bunches, separated by 30m which means interactions occur in ZEUS every 96ns. Some of the bunch slots are left empty to allow the study of background effects from interactions with residual gas in the ring.

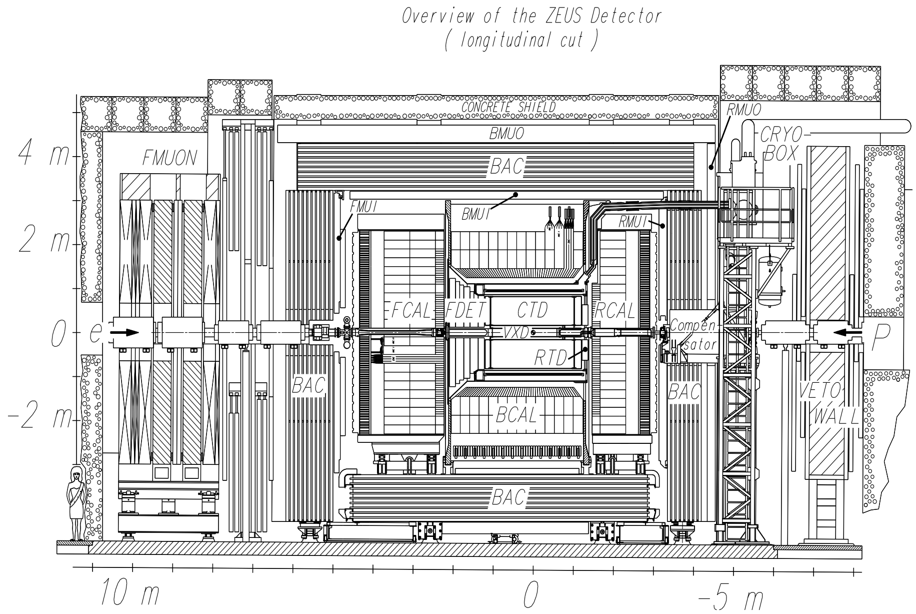

Figure 3.4: *A schematic diagram of the ZEUS detector showing the major components. The view is parallel to the beam axis. The scale is indicated by the figure in the bottom left.*

3.3 The ZEUS Detector

The data used in this analysis was collected by the ZEUS detector [14] between 1996 and 2000. A longitudinal view of ZEUS parallel to the beam axis is shown in Figure (3.4).

The proton beam direction is from right to left across Figure (3.4). The detector is situated in the South Hall of the HERA accelerator complex, at one of the interaction points of the electron and proton beams. The detector itself is approximately 10 metres high and 20 metres in length. Its construction is asymmetric along the beam direction to reflect the nature of *ep* scattering.

The ZEUS detector is designed to detect particles produced in the *ep* collisions using a combination of drift chambers to identify the trajectories of charged particles and a calorimeter to absorb and measure the energy deposits from incident particles.

3.3.1 ZEUS Co-ordinate Scheme

The ZEUS coordinate scheme is right-handed with the Z direction parallel to the beam pipe through the centre of the detector, and the positive Z direction pointing along the direction of travel of the proton beam. The Y axis is upward pointing. The nominal interaction point is located at $X = Y = Z = 0$..

The polar angle, θ, runs from small values in the forward, positive Z direction to 180° in the backward direction. The azimuthal angle, ϕ, runs from 0 to 360° centred around the Z axis. The XY plane is that perpendicular to the beam direction.

A view along the beam axis of the detector showing the central components in the XY plane is given in Figure (3.5)

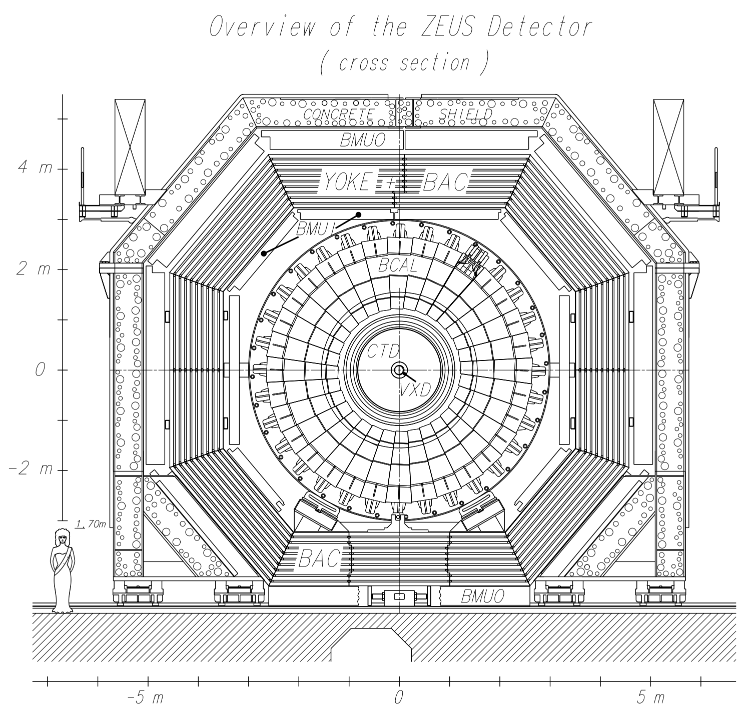

Figure 3.5: *Cross Section of the ZEUS detector in the XY plane. The view is along the beam pipe.*

3.4 Essential ZEUS Components

A brief summary of the individual components which make up the detector follows, beginning with those essential to data taking, primarily the calorimeter and tracking detectors.

3.4.1 Tracking

Charged particles passing through drift chambers leave tracks which can be identified in the detector by the tracking detectors, the CTD (Central Tracking Detector) [15]-[17] and the FRTD (Forward and Rear Tracking Detectors). The CTD covers a polar angular range of $15^\circ < \theta < 164^\circ$. The FRTD covers the polar angular ranges $7.5^\circ < \theta < 28^\circ$ and $160^\circ < \theta < 170^\circ$. Until 2000, the forward section of the FRTD consisted of the forward detector, FDET and the transition radiation detector, TRD. The TRD has now been replaced with a new detector, the straw tube tracker in an attempt to improve track resolution in this region.

The Central Tracking Detector

Moving outwards from the beam pipe and interaction region the CTD is the first crucial component encountered by particles produced in a scattering event. The CTD is a cylindrical drift chamber of length 240cm extending to an outer radius of 85cm, for detecting and accurately measuring the trajectories and momenta of charged particles. The CTD comprises 4608 sense wires in total divided into 9 superlayers. Each of the superlayers is further divided into 8 layers of sense wires. Of the 9 superlayers, 5 consist of sense wires parallel to the drift chamber axis and the remaining 4 contain wires at a small stereo angle of 5° which means the azimuthal and polar angular resolutions are roughly equal.

An example of an octant of the CTD is displayed in Figure (3.6).

The CTD chamber is filled with argon, carbon dioxide and ethane gases. A uniform electric field is provided by high voltage wires in addition to the magnetic

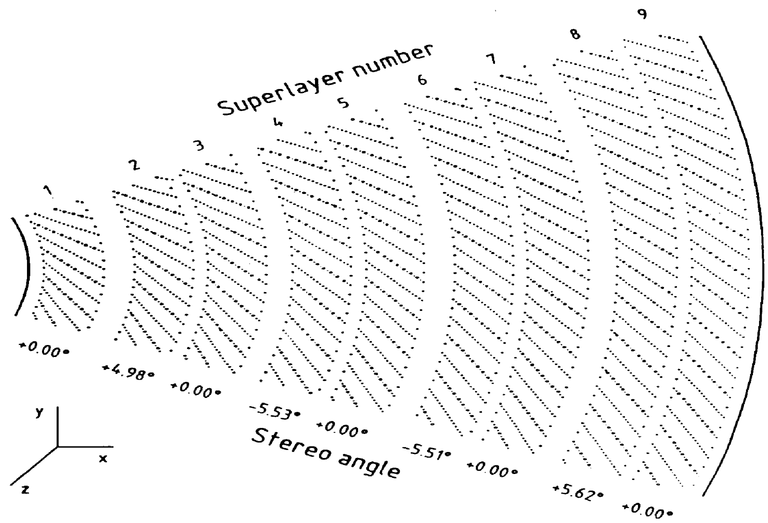

Figure 3.6: *A CTD octant in the XY plane showing the 9 superlayers. The view is along the beam direction.*

field produced by the surrounding solenoid magnet. Ions and electrons produced by charged particles drift through these fields causing hits on the sense wires. A well reconstructed track requires hits to be present in at least 12 or more layers.

Aided by an axial magnetic field of 1.43T from the solenoid, the CTD is able to achieve a high resolution on the track momentum of high momentum particles over a wide angular range. Final state hadrons and leptons are reconstructed with a spatial resolution of 190μm and a momentum resolution as defined in Equation (3.1).

$$\frac{\sigma(p_t)}{p_t} = 0.0058 p_t \oplus 0.0065 \oplus \frac{0.0014}{p_t} \tag{3.1}$$

The Solenoid

The solenoid is a thin superconducting magnet which sits between the CTD and the barrel calorimeter and provides the axial magnetic field to allow momentum measurement. The magnet is as thin as possible to prevent any impairment to the detection of photons and electrons in the calorimeter. The effect of this magnet on the HERA beams is compensated for by a high field superconducting solenoid located in the rear endcap of the iron yoke.

Forward and Rear Tracking Detectors

The Forward and Rear Tracking Detectors, FRTD, are also comprised of drift chambers and extend the tracking coverage out to wider angles. The Forward Tracking Detector, FTD, is made up of three planar drift chambers, each containing three layers, with 18 wire planes in total. The individual layers are made up of rectangular drift cells which are rotated 60° with repect to each other. Each drift cell containts 6 sense wires at right angles to the beam axis.

3.5 The ZEUS Calorimeter

Covering 99.8% of the entire solid angle, the calorimeter [18] is probably the most important central component of the ZEUS detector. Constructed using interleaved layers of depleted uranium and plastic scintillator the ZEUS calorimeter is optimised for the detection of hadronic jets, which are of major importance in the study of Quantum Chromodynamics. The purpose of the calorimeter is to absorb the energy of particles and convert it into a light signal which can be read out by fast electronics.

3.5.1 Interaction of Particles with the Detector

The nature of their interaction with matter varies for particles of different types, differing particularly between electromagnetic and hadronic particles. In jet measurements it is desirable to achieve the same response of the calorimeter to hadronic and electromagnetic particles of the same incident energy as jets often contain a sizeable π^0 or γ component before reaching the calorimeter. The ZEUS calorimeter is a compensating calorimeter, specifically designed and engineered to produce an equal response to hadrons and electrons. This means that the intention is to achieve the same output signal for electromagnetic and hadronic particles of the same incident energy. The ratio of the response to electromagnetic particles to the response to hadronic particles is denoted by e/h. Typically this ratio is dependent on the incident energy and the type of calorimeter. For a non-compensating calorimeter $e/h \approx 1.1 \rightarrow 1.35$, indicating a higher response to electromagnetic particles. In a compensating caloriemeter the absorbing materials used in the detector are carefully chosen to equalise the response to both types of particle and achieve an e/h ratio of 1. This helps to reduce the error in energy measurements.

Electromagnetic Showering

Energy is lost by particles travelling through a medium by either radiation or ionisation. Electrons, which have a low mass, tend to lose energy primarily by radiation. This radiative mechanism is the emission of Bremsstrahlung photons. If these photons are of sufficient energy they convert into e^+e^- pairs. These electromagnetic particles further interact with the electromagnetic fields of the material producing more photons, which in turn pair produce if they are of high enough energy. Thus an electromagnetic shower develops in the target material.

Hadronic Showering

A hadronic shower occurs via a different mechanism. Hadronic particles are heavier and lose energy through ionisation. As well as interaction with the electromagnetic fields of a material, hadrons interact with nuclei within the material producing more hadrons or starting nuclear decay. The energy is transferred to the constituent atoms of the materials creating ion-electron pairs which go on to further interact. Hadronic showers are broader than electromagnetic showers and the hadronic interaction length is typically considerably longer than the radiation length. To properly measure hadronic showers the calorimeter must respond equally to both the hadronic and electromagnetic components of the hadronic shower.

3.5.2 Calorimeter Construction

The ZEUS calorimeter weighs 700 tons in total and is divided into 80 modules which form three separate calorimeter sections, Forward, Barrel and Rear, FCAL, BCAL and RCAL, which cover the polar angular ranges $2.6° < \theta < 36.7°$, $36.7° < \theta < 129.1°$ and $129.1° < \theta < 176.2°$ respectively, where the polar angle is measured from the proton beam direction. Each section of the calorimeter is divided longitudinally into an electromagnetic part and a hadronic part, which lies outside. The sections are divided into cells, of typical size $20cm \times 20cm$ for the hadronic part, HAC, and $5cm \times 20cm$ for the electromagnetic part, EMC. The entire calorimeter consists of 6000 cells. The readout is done using scintillating material and photomultiplier tubes, PMTs. Information for an event can be read out very quickly.

A side view of an FCAL module showing the separation into EMC and HAC parts is shown in Figure (3.7).

Each EMC tower in the calorimeter has a depth of 25 radiation lengths, or 1 nuclear interaction length and each HAC tower is between 4 and 6 nuclear interactions long. The length of the HAC sections means that 90% of incident jets of particles should deposit at least 95% of their energy in the calorimeter.

3.5.3 Energy Resolution

Calorimetry is central to the success of physics analysis using the ZEUS detector. The calorimeter is designed to optimise the measurement of jets. Coverage of almost full solid angle is provided and jet energy measurement is carried out with an energy resolution, based on test-beam data, as given in Equation (3.2).

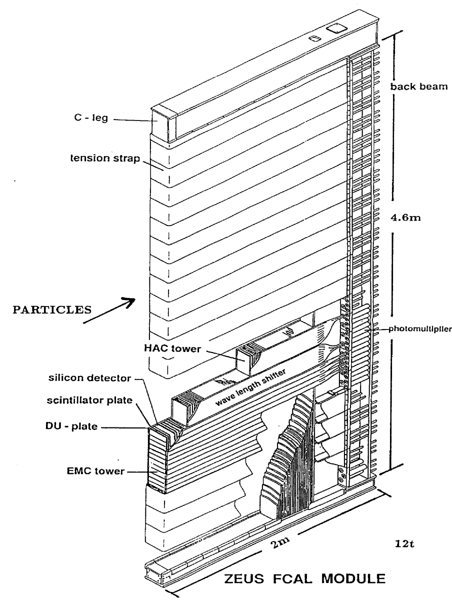

Figure 3.7: *A ZEUS FCAL module*

$$\frac{\sigma(E)}{E} = \frac{35\%}{\sqrt{E}} \oplus 1\% \tag{3.2}$$

The energy resolution of the calorimeter for electromagnetic particles is given in Equation (3.3).

$$\frac{\sigma(E)}{E} = \frac{17\%}{\sqrt{E}} \oplus 1\% \tag{3.3}$$

The calorimeter is also able to provide an angular resolution for jets of 10 mrad or better.

3.5.4 Calorimeter Readout

Information is readout from the calorimeter modules using scintillators and photomultipliers. Advantages of this method are that the pulses can be kept shorter than the bunch crossing time of 96ns, which stops information piling up and reduces dead time. Each of the 6000 cells which make up the calorimeter is read out by two PMTs. The calorimeter is made up of layers of depleted uranium which act as an absorbing material. In between these layers are layers of plastic scintillator. Showers lose energy in the absorbing regions and are sampled by the scintillators. The light produced by the scintillators is collected by wavelength shifting plates and transmitted to the photomultiplier tubes.

3.5.5 The Barrel Calorimeter

This analysis is heavily dependent on the construction of the BCAL [19] as part of the photon identification procedure. The layout of calorimeter cells in this region allows a distinction to be made between photons and neutral pion or eta decays. The BCAL covers the angular region $36.7^\circ < \theta < 129.1^\circ$ and the entire azimuthal range. It is constructed from 32 wedge-shaped modules which each span 11.25° in azimuth. These 32 modules are each rotated by 2.5° in the azimuthal plane around an axis parallel to the beam axis but situated at a radius of 2.3m from the beam. This rotation prevents photons escaping undetected through gaps between modules by ensuring the wavelength shifter plates do not point to the beam axis. A view of an individual BCAL module is shown in Figure (3.8). A longitudinal view of the BCAL perpendicular to the beam direction is shown in Figure (3.9). Figure (3.10) shows a view of the BCAL as seen looking along the beam pipe.

BCAL Module Design

Each individual module is segmented along its length into 3 separate sections, which are read out independently. There is one electromagnetic section, EMC, and two hadronic sections, HAC1 and HAC2. The EMC section is composed of 53 towers which are projective in polar angle and have front face dimensions of $49 \times 233mm^2$. The 14 HAC towers are non-projective. Each HAC tower covers four EMC towers with the exception of the front one which is narrower and covers only two EMC towers. The total depth of the BCAL corresponds to 5 nuclear

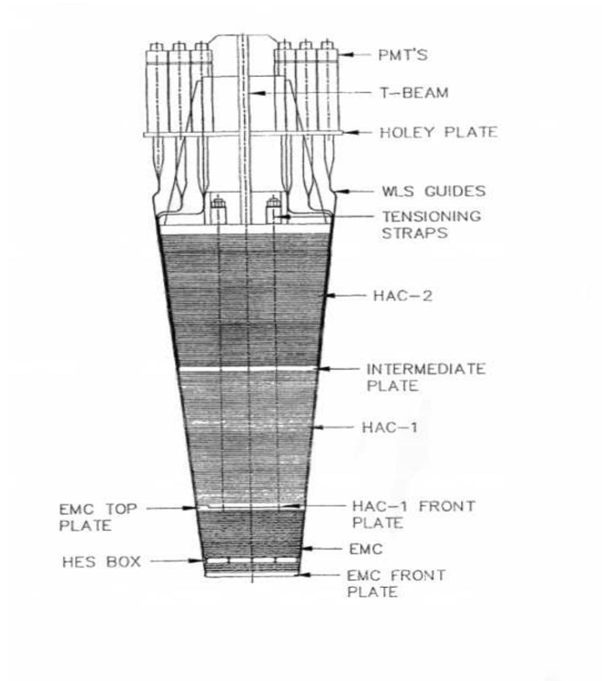

Figure 3.8: *Transverse cross section through an individual BCAL module showing the structural elements.*

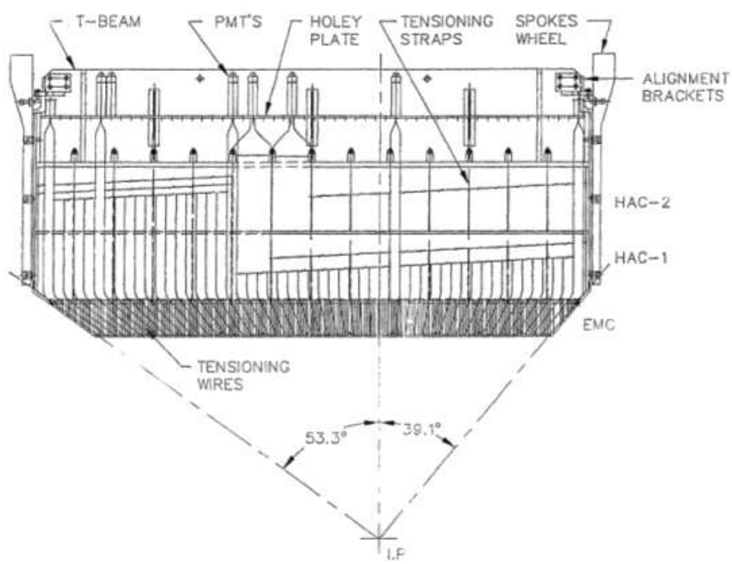

Figure 3.9: *A longitudinal view of the ZEUS Barrel Caloriemeter.*

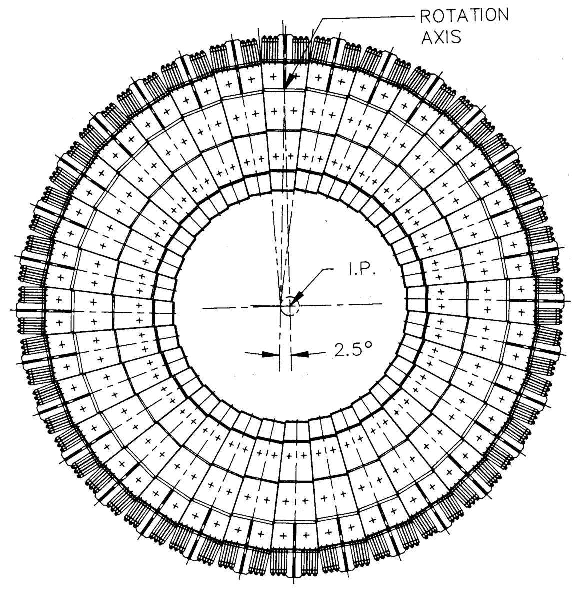

Figure 3.10: *Cross Section of the BCAL in the xy plane*

interaction lengths.

3.6 Outer Components

The outer components of the detector provide useful supplementary information to the inner components and are also important in detecting background processes. Very energetic particles such as muons which pass undetected through the calorimeter can also be identified in the outer regions.

3.6.1 Luminosity Monitoring

Luminosity from HERA is measured in the ZEUS interaction region by the bremsstrahlung process. The method is based on detecting in coincidence the final state electron and photon which are emitted at very small angles from the beam direction [20]. The cross section for this process integrated over angles is given by the Bethe-Heitler formula. By limiting the electron and photon energies the cross section integrated over photon energy is 15.4mb which corresponds to an event rate of 230kHz. Thus fast, continuous monitoring of the luminosity is achievable.

The luminosity monitor consists of an electron detector near the electron beam pipe at a distance of 35m from the interaction region and a photon detector located a further 70m down the tunnel.

3.6.2 Muon Chambers and BAC

Muons are identified at ZEUS using the Backing Calorimeter, BAC, and the muon chambers. The BAC carries out two roles, the return yoke of the central solenoid and also a calorimeter for extremely energetic particles leaking out from the calorimeter in the Barrel region. The BAC measures the energy of late showering particles with a resolution as given in Equation (3.4).

$$\frac{\sigma(E)}{E} = \frac{110\%}{\sqrt{E}} \tag{3.4}$$

The muon chambers surround the detector and measure the trajectories of energetic muons which have crossed the calorimeter. Detection of muons is important in the study of background processes like beam gas, halo muon production or cosmic ray events. In the forward direction muons can be detected by the FMUON at very small angles from the proton direction, where the momentum resolution of the CTD and FTD is much reduced. The FMUON provides an independent measurement of the muon momentum and passess information to the trigger to allow background events to be rejected.

3.6.3 The VETO Wall

The Veto wall is located near the tunnel exit on the proton beam side of the detector. The main purpose of it is to protect the central detector from the beam halo around the proton bunches. Background particles are absorbed and events arising from particles passing through the veto wall can be rejected. The wall is constructed from iron with two scintillator hodoscopes on each side.

3.6.4 The Hadron Electron Separator

The Hadron Electron Separator, HES, can play a role in the identification of electrons produced within jets. The HES covers the electromagnetic sections of the calorimeter by one layer of silicon diodes in the barrel and rear regions and two layers in the forward direction where particle densities and energies are higher.

3.7 The ZEUS Trigger System

Physics events in ZEUS are identified and selected via a 3-tier trigger mechanism. With a bunch crossing occuring every 96ns the trigger must be highly efficient to minimise loss of data and dead time. The data acquisition, DAQ system can only deal with a small fraction of events occurring, however the vast majority of events seen in the detector are non *ep* interactions, but instead are beam gas interactions. It is necessary to reduce the rate of events to less than 10MHz but still efficiently select *ep* events. Each level of the trigger is more sophisticated than the previous one, requiring more information and time to make a decision on a particular event.

3.7.1 First Level Trigger

The first level trigger, FLT, is purely hardware and reduces the rate of data to around 1kHz by eliminating most of the background events. Each component has its own specific FLT and a decision for each event is made by combining the results of each component's decision in the Global First Level Trigger, GFLT. To avoid deadtime in the readout system, information from components is stored in pipelines until the decision of the GFLT which occurs at between 4.4 and 5μs after the bunch crossing. The GFLT receives the signal from each component and makes a decision on the event. This is done electronically. The trigger electronics are pipelined as well, with each step repeated every 96ns, so that, as data from one event moves forward one step, data from a new event can enter. At this first stage the trigger information from the calorimeter is the most important factor in deciding the fate of an event.

Calorimeter First Level Trigger

The Calorimeter First Level Trigger, CFLT, is the most significant part of the initial triggering mechanism. The CFLT uses a pipeline design to provide data for a GFLT decision 5μs after each beam crossing. Summary data is sent to the GFLT after 2μs. The CFLT provides information on:

* Total energy of an event
* Tranverse energy of an event
* Missing energy in an event
* Energy and number of isolated leptons
* Electromagnetic and hadronic energy in various regions of the calorimter

The CFLT allows the experimental trigger rate to be kept below 200Hz at the highest luminosities so far experienced at HERA.

3.7.2 Second Level Trigger

Events which pass the GFLT are passed up the chain to the SLT which is a software based trigger. The SLT reduces the rate to around 100Hz. At this stage, the data is more precise and complete and information coming from different components can be more accurately correlated. The SLT looks for signatures of interesting interactions after doing some basic analysis of information from the components. Information from the first and second level triggers of all events which pass the Global Second Level Trigger, GSLT, are sent to the Event Builder, EVB which combines data from the separate components into a single record of the event, to be passed on to the third level trigger, TLT.

3.7.3 Third Level Trigger

The Third Level Trigger, TLT, carries out a more detailed analysis of the information by running a reduced version of the offline analysis software. The input to the TLT consists of a mixture of beam gas, photoproduction and some DIS events. The TLT reduces the rate to 3-5Hz. At this stage a geometrical reconstruction is performed for each event. Raw data from the components is corrected using calibration information and information from different events is matched. Events can be classified into particular types depending on what third level triggers they pass.

Chapter 4

Event Selection and Reconstruction

To preserve limited statistics as fully inclusive a DIS event sample as possible is selected, because the complete DIS event set must by definition contain all the DIS prompt photon events of interest. Using this well-defined DIS subset of the entire data set, several combinations of electron and photon finding algorithms can be tested in order to establish the best selection method. The event selection is divided into online and offline cuts, where the offline cuts define the specific physics of interest and can be easily varied to determine the effect on the overall cross section.

4.1 The ZEUS Event Store

The Zeus Event Store, ZES [21], is used to obtain as broad a sample as possible of neutral current DIS events. ZES is an object-oriented database written in C++ [22]. Its configuration gives a fast and flexible way of selecting events to be used in ZEUS analysis. Over 300 pre-calculated variables are available to select events for further analysis.

4.1.1 NC DIS Event Selection using ZES

A standard neutral current deep inelastic event will have an electron, located towards the rear of the detector and some hadronic activity, probably forming at least one jet, with further energy deposits in the calorimeter and a number of tracks measured in the CTD.

DST Bit Selection

DST bits are trigger configurations which are based on third level trigger information and some selection algorithms. The first demands made were that every event should pass through the neutral current DIS triggers DST 9 and DST 11, which are defined as:

* DST 9: Electron energy $>$ 4 GeV after running 4 electron finders (see below);
* DST 11: Nominal Neutral Current trigger which selects a set of events with a loose $E - P_z$ cut.

In order to select the widest possible set of events and not lose potential events of interest, the four electron finding algorithms available for ZEUS analysis are run over the data at an early stage and if an electron candidate of the appropriate energy is found by any one routine then the event will pass the DST 9 trigger.

The nominal neutral current trigger, DST 11, is a loose selection which encompasses a wide range of possible neutral current events.

Physics Cuts in ZES

To reduce the volume of data being selected some more specific cuts were also applied in the ZES selection. DIS cuts applied here are similar to those used in previous DIS analyses at ZEUS [23]. These cuts are listed as follows:

* $Z_{vtx} > -40cm$ and $Z_{vtx} < +40cm$

* $E - p_z > 35$ GeV and $E - p_z < 65$ GeV
* $y_{el} < 0.95$
* $y_{jb} > 0.04$
* $E_e > 10$ GeV

Further explanation of the motivation behind these cuts can be found in the following sections.

4.2 DIS Selection Cuts

4.2.1 Z Vertex

The initial event selection involves cuts to select good quality physics events, by suppressing the large background of non-physics events which occur in ZEUS, such as beam gas interactions. Background events are all those arising from processes other than electron-proton scattering, such as beam gas or cosmic ray interactions. The primary signature of electron-proton scattering is a well-defined vertex located within a specified distance of the nominal interaction point $(0, 0, 0)$. The Z_{vertex} of an event is found by timing measurements from the calorimeter. The Z_{vertex} distribution of a sample of ZEUS data events, prior to any further selection cuts is shown in Figure (4.1). The wide tail on the raw data distribution in Figure (4.1), extends over 1 metre on either side of the central point. This tail mainly results from the background processes.

4.2.2 $\sum(E - p_Z)$

There are several Q^2 regions of interest in physics studies at ZEUS. Relevant to the analysis here is $Q^2 > 10 GeV^2$, the deep inelastic region. As the cross section for *ep* scattering is proportional to $1/Q^4$ there is a large number of events

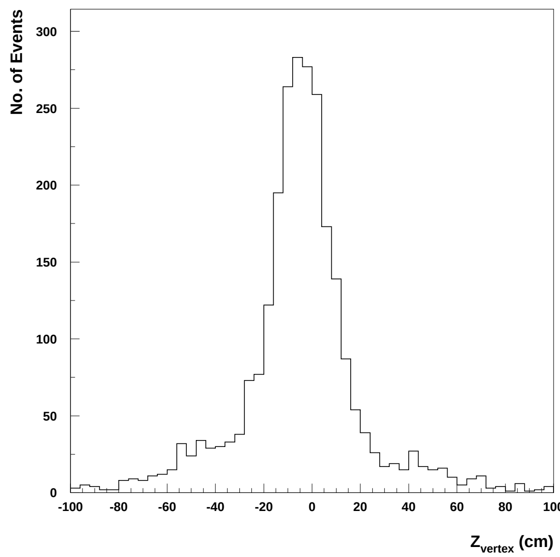

Figure 4.1: Z_{vertex} *position for ZEUS data events, pre-selection. The wide tail on the distribution represents background events, such as cosmic ray and beam gas interactions.*

at $Q^2 \sim 0$ which is known as the photoproduction region. These are events where the scattered electron is almost collinear to the incoming electron and thus escapes undetected down the beam pipe. Photoproduction events contribute significantly more than DIS events to the total *ep* scattering cross section so these type of events must be suppressed. The most efficient way to do this is to study the $\sum(E - p_z)$ of an event. This is a conserved quantity which is prior to the collision equal to twice the sum of the electron energy for each event (electrons travel in the negative Z direction). In the case of photoproduction the electron escapes down the beam pipe after the interaction and is not detected, leading to a large amount of missing energy. A well contained DIS event, where all the initial particles or their decay products are detected in the calorimeter will have an $\sum(E - p_z)$ value of 55GeV, twice the initial energy of the positron. DIS events are therefore selected with $\sum(E - p_z) > 35GeV$.

However, in some photoproduction events a particle such as a π^0 can be misidentified as an electron. Events of this type can be removed by a further cut on the $\sum(E - p_z)$ of the event. An upper cut is also applied to exclude events with double interactions occuring.

A further cut to exclude remaining photoproduction events from the analysis is made on $y_{electron} < 0.7$ as these events typically have $y_{electron}$ values of close to one.

4.2.3 Calorimeter Noise

Due to noise in the calorimeter from decays of Uranium, measurements can be distorted when the hadronic activity is low. To prevent this a minimum cut is made on $y_{JB} > 0.04$, as the Jacquet-Blondel method is the best way of reconstructing kinematic variables in this low y region. This definition of y is given in Equation (2.4).

4.2.4 Electron Energy Cleaning Cut

The distribution of electron energy for all DIS events selected is shown in Figure (4.2). This shows that the energy spectrum of the scattered electron peaks at around 22 GeV with very few events at energies below 10 GeV. A cleaning cut on the electron energy is made to remove these events with electrons reconstructed at very low energies. Figure (4.2) confirms that few events will be lost by this cut.

4.3 Electron Finding

Based on the trigger configuration used, it is expected that from the set of DIS events passing loose selection cuts applied so far most, if not all will have an electron present. The first step in a more detailed event selection is to identify

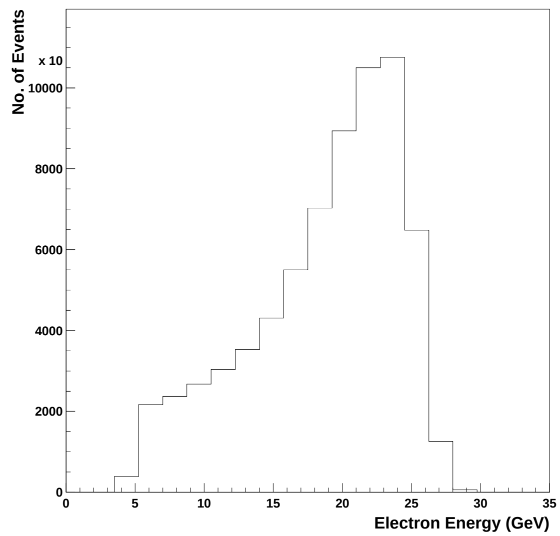

Figure 4.2: *Energy distribution of DIS scattered electrons.*

this electron within each of these events and demand primarily that it should be present and well-reconstructed. From the previous investigation of ISR/FSR events it is known that in such cases the emitted photon will be most often in the angular range which corresponds to the rear calorimeter region of the ZEUS RCAL, so it is better not to consider photon candidates in this area. The polar angle distribution of scattered electrons for all accepted DIS events is shown in Figure (4.3).

Figure (4.3) shows that this backward region is also the most likely destination for the final state electron, so the electron finding is done using the SINISTRA [24] electron finder which is a neural network trained to find electrons in the RCAL region of the ZEUS detector. SINISTRA has an electron finding efficiency of 95% in the RCAL. Electron candidates found are ordered in probability of being an electron. For each event the candidate with the highest probability is assumed to be the electron. Events with electrons outwith the angular range corresponding to the ZEUS RCAL region are rejected for this analysis. To ensure the candidate

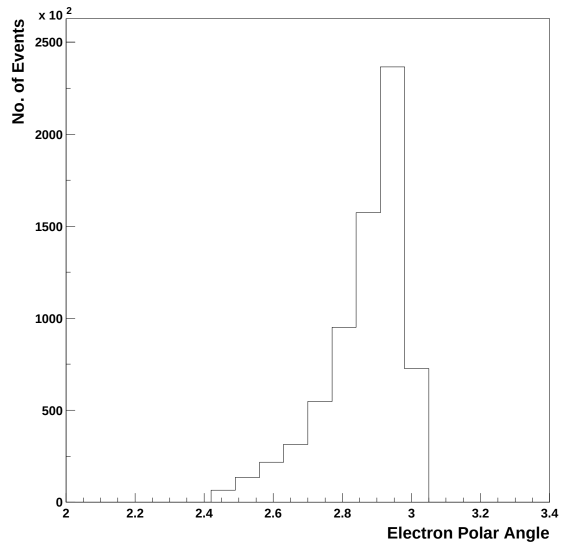

Figure 4.3: *Polar angle distribution of final state scattered electrons.*

is fully contained in the RCAL, the electron polar angle is selected as in Equation (4.1).

$$2.44 < \theta_{electron} < 3.0 radians \tag{4.1}$$

Electrons with $\theta_{electron} > 3.0$ radians are rejected as too close to the beam pipe. The range is restricted to the rear direction to minimise identification problems between the electron and the photon. The majority of events have electrons which are scattered through a small angle and end up in the rear direction so the statistics lost through this angular restricition are limited.

4.3.1 Event Kinematics

The event kinematics are calculated from the electron system, which is the most straightforward method for this type of event. In each event, the electron is present and its energy and polar angle are well-measured. Q^2 and $y_{electron}$ for the event are calculated using Equations (2.5) and (2.6). The cuts then made to these variables are listed in Equations (4.2) and (4.3).

$$Q^2 > 35GeV^2 \tag{4.2}$$

$$y_{electron} < 0.7 \tag{4.3}$$

A cut of $Q^2 > 35GeV^2$ is made as the signal to background ratio from the neutral meson subtraction (see Chapter 5) is improved at higher Q^2 values. The cut on $y_{electron}$ is made to remove possible photoproduction events left in the sample. Together both cuts help to provide a cleaner set of events.

4.4 Prompt Photon Search

Having established this sample of clean neutral current DIS events the next stage is to run a 'photon finder' to look for candidate prompt photons within these events. The aim is to obtain an inclusive sample of prompt photons. The event signature for these inclusive events consists of only a well reconstructed electron somewhere in the rear calorimeter as described previously, and a second electromagnetic cluster in the central region, plus some significant hadronic activity in the detector.

4.4.1 Photon Search Region

The search for a prompt photon candidate is restricted to the central part of the ZEUS detector, the Barrel Calorimeter, BCAL. There are several reasons to restrict the photon search to the BCAL. The most important is that the arrangement of cells in this calorimeter is very useful in the necessary neutral meson background subtraction. Also, the forced separation into different calorimeter sections is very helpful in distinguishing photons from electrons, which are mainly to be found in the RCAL area.

A further reason for choosing the central region for photon finding is that initial and final state leptonic radiation, which is emitted nearly collinear to the incoming or scattered electron is found primarily in the RCAL region. Looking for photons away from this region greatly suppresses the contribution from this type of process. The number of events where a potential photon would be found in the forward direction is insignificant and the forward direction is also dominated by hadronic activity from the proton remnant. Therefore no photon finding is performed in the forward region.

4.4.2 Photon Selection Cuts

Prompt photon candidates are selected in the energy range defined in Equation (4.4) and the pseudorapidity range given in Equation (4.5).

$$5 < E_T^{\gamma} < 10 GeV \tag{4.4}$$

$$-0.7 < \eta^{\gamma} < 0.9 \tag{4.5}$$

The energy range in Equation (4.4) is chosen to maximise the efficiency of the background subtraction which must be later performed. The pseudorapidity range in Equation (4.5) corresponds to the ZEUS BCAL region. It is calculated using the calorimeter cell location and the production vertex for each event.

4.4.3 Photon Finder

Photon candidates are found using the electron finding algorithm, ELEC5 [25], which is less stringent than SINISTRA in its demands of an electromagnetic cluster and finds the photon candidates, which are of lower energy, without any tracking information being used. The algorithm also finds the neutral meson background which can then be properly subtracted. It is necessary to properly cover the full range of the background as this is needed for the subtraction routines. The more relaxed electron identification criteria applied by ELEC5 allow the much larger electromagnetic clusters associated with these neutral mesons to be identified as electron candidates.

4.4.4 Electron-Photon Separation

Care must be taken to avoid double counting, as the SINISTRA electron is always on the list of candidates returned by ELEC5 as would be expected. This can be done in two ways which lead to very similar results. Firstly, the list of calorimeter cells belonging to the electron as found by SINISTRA is compared to the list of cells belonging to every photon candidate found by ELEC5, and if any cells are common to both lists it is assumed that the electron has again been identified and the candidate is rejected.

A more intuitive method is to simply calculate the absolute distance between each prompt photon candidate and the electron and to reject photon candidates within 50cm of the electron, i.e. $\sqrt{\Delta x^2 + \Delta y^2} < 50cm$. This cut, in effect, forces the photon candidate to be in the BCAL.

4.5 Photon Isolation

Prompt photon signals can be faked by events in which a neutral meson such as a π^0 or η produced within a jet is misidentified as a single photon. These particles look very similar to an electron finder. There are also a class of events where photons are produced from fragmentation processes in the middle of hadronic jets. In order to suppress this contribution to the prompt photon cross section the photon candidate is required to be isolated from nearby tracks and energy deposits. Neutral mesons produced in these events are often close to tracks and unassociated energy deposits. Photons produced from fragmentation processes within jets will also have a similar energy signature in the calorimeter.

Isolation cuts are effective at removing a substantial fraction of these events however sufficient events remain which must be statistically subtracted at a later point.

4.5.1 Track Isolation

As a neutral particle a photon will leave no tracks in the detector and hence, an isolated photon should not be close to any tracks. The separation of the photon, Δr from each track in an event is defined in Equation (4.6).

$$\Delta r = \sqrt{(\eta^{\gamma} - \eta^{track})^2 + (\phi^{\gamma} - \phi^{track})^2} \tag{4.6}$$

In Equation (4.6), η and ϕ are the pseudorapidity and azimuthal angle of the photon and the track. The distance of the photon from the track is calculated for all tracks which are reconstructed in a pseudorapidity range of -1.9 to 1.9 and with transverse momentum, $p_T^{track} > 200 MeV/c$. A cut is made on the separation between the photon and the closest track in an event. A cone is constructed in $\eta - \phi$ space around the photon and the cut defined in Equation (4.7) is applied.

$$\Delta r_{min} > 0.2 \tag{4.7}$$

The distance of the nearest track can be studied in data and Monte Carlo, at both generator and detector level. The distance to the nearest track for events of each of these three types is shown in Figure (4.4).

Studying the track isolation in Figure (4.4), a clear peak near zero can be seen in both data and detector level Monte Carlo events, perhaps suggesting the misidentification of an electron as a photon. This behaviour is not evident in generator level Monte Carlo events, where the prompt photon is seen to be well isolated from the nearest track. It is seen that this cut has a signifcant effect on the data, removing a large number of wrongly identified photon candidates.

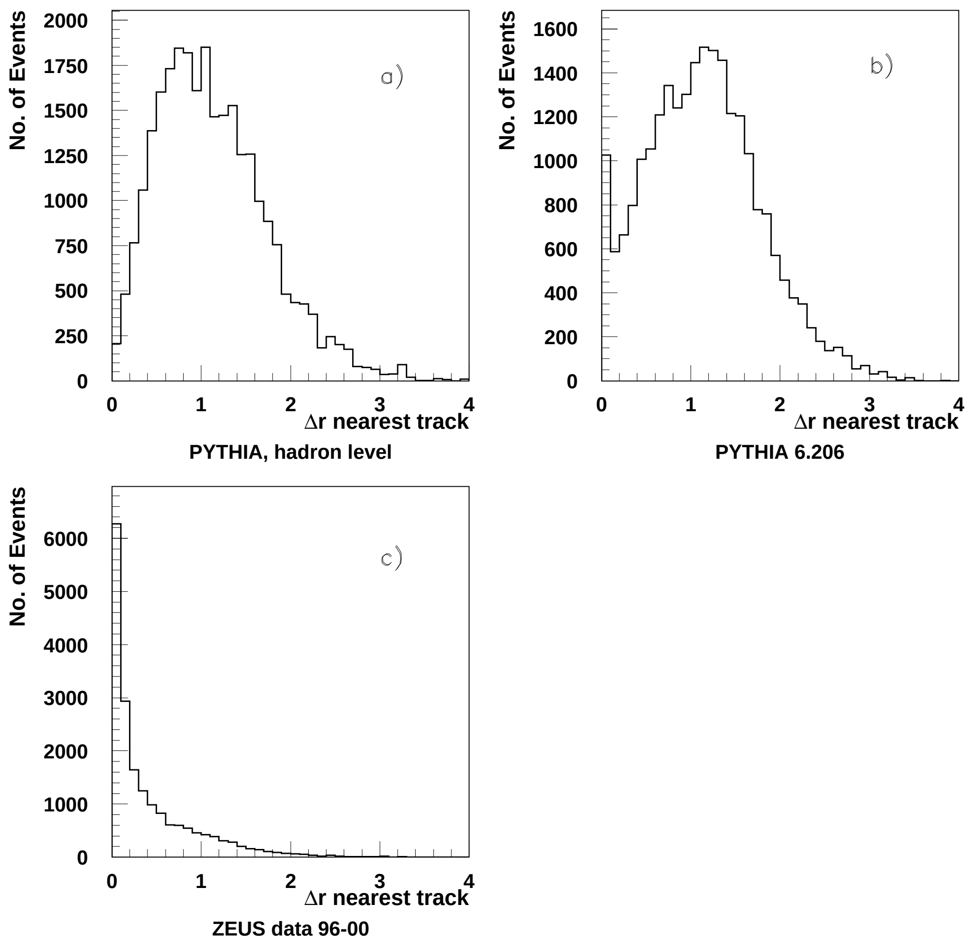

Figure 4.4: *Separation in $\eta - \phi$ space of photon candidate from the nearest track with $p_T^{track} > 200$ MeV/c for a) PYTHIA at generator level, b) PYTHIA at detector level and c) ZEUS 96-00 data.*

4.5.2 Energy Isolation

A second isolation cut removes events where there is a large amount of unassociated energy around the photon candidate. A cone of radius 1.0 in $\eta - \phi$ space is formed centred on the photon candidate and the all the energy within the cone is examined. A sum of the energy of all cells belonging to the photon cluster is compared to the sum of all the energy of the cells within the cone. It is required that at least 90% of the energy in the cone must belong to the photon candidate.

In Figure (4.5) a sharp peak can be seen at one, showing that in PYTHIA the prompt photons are well-isolated when generated. This peak is also apparent in the Monte Carlo after detector simulation although less sharply defined. Studying the energy distribution of generated prompt photon events led to the isolation cut in Equation (4.8) being imposed. The data distribution is improved by applying cuts on the photon energy and the presence of nearby tracks.

$$\frac{E_{\gamma}}{E_{r<1.0}} > 0.9 \tag{4.8}$$

4.6 QED Compton and DVCS Rejection

Both elastic QED Compton events and deeply virtual Compton scattering, DVCS, events have a final state which consists of an electron and a photon with no hadronic activity detected. These event types can be suppressed through both tracking measurements, as these events will possess a maximum of one track, associated with the final state electron, and through energy measurements. A cut on the ratio of the sum of the electron and photon energies to the total event energy is made, demanding that together the electron and the photon must make up less than 95% of the total event energy. These requirements can be summarised as:

* No. of good tracks per event ≥ 2

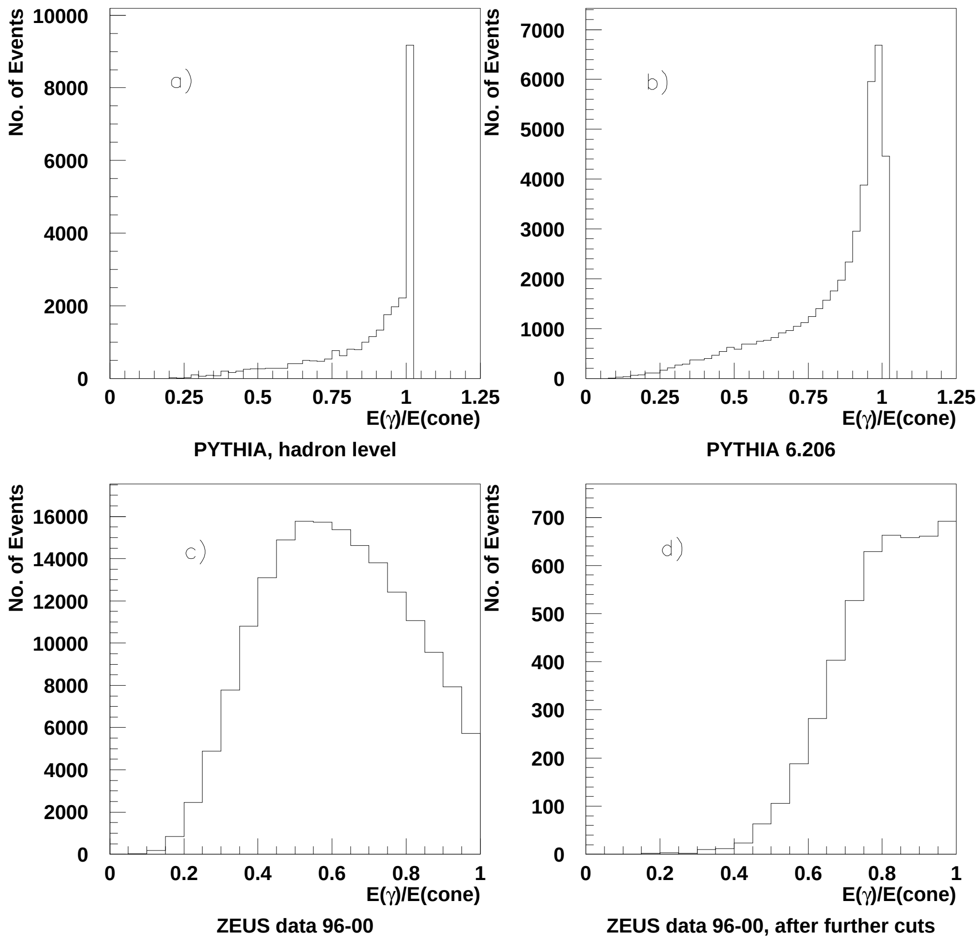

Figure 4.5: *Energy in a cone of radius 1.0 in $\eta - \phi$ space around the photon candidate for a) PYTHIA at generator level, b) PYTHIA at detector level, c) ZEUS 96/00 data and d) ZEUS 96-00 data, after further selection cuts.*

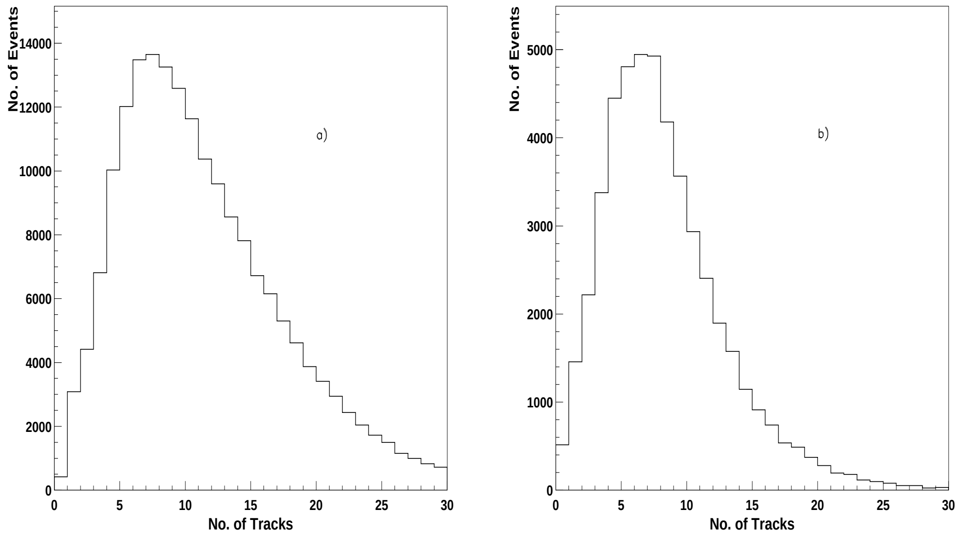

Figure 4.6: *Total number of good tracks per event for a) ZEUS 96-00 data and b) Monte Carlo. A good track has* $p_T^{track} > 200MeV/c$ *and* $-1.9 < \eta^{track} < 1.9$.

* $\frac{E_{elec}+E_{\gamma}}{E_{total}} < 0.95$

The total number of good tracks per event is shown in Figure (4.6) for both data and Monte Carlo. A good track is one with p_T^{track}¿200 MeV/c and $-1.9 < \eta^{track} < 1.9$.

It it seen in Figure (4.6) that the number of tracks found per event had a similar shape for both data and Monte Carlo, peaking at around 10 tracks, with very few events having only 1 or 2 tracks.

The energy ratio used in rejecting QED Compton is shown in Figure (4.7). It is observed in Figure (4.7) that very few events have values above 0.95, so this cut has a small effect, but is a useful precautionary measure in eliminating unwanted events.

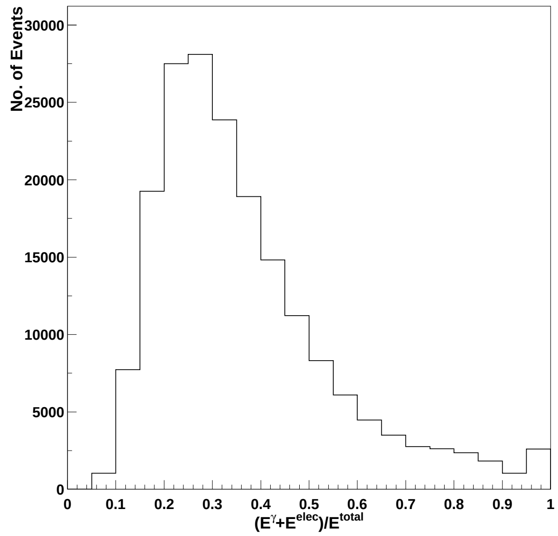

Figure 4.7: *Ratio of the sum of electron and photon energies to the total calorimeter energy in an event. Events with high values may be QED Compton.*

4.6.1 Prompt Photon Candidate Events

As previously indicated, the final event signature is a well reconstructed electron in the rear calorimeter, an isolated photon candidate in the central region and any further hadronic activity. Examples of prompt photon candidate events displayed using LAZE [26], the ZEUS event display, are shown in Figures (4.8) and (4.9).

In Figure (4.8) the photon candidate is seen in an isolated position in the top central region of the diagram, with the electron present in the RCAL and hadronic activity clearly present in the forward calorimeter.

Figure (4.9) is a typical prompt photon event, with the isolated photon visible in the centre of the top section of the barrel calorimeter. A jet can be seen in the bottom right of the diagram and the electron, as before, is to be found in the rear direction.

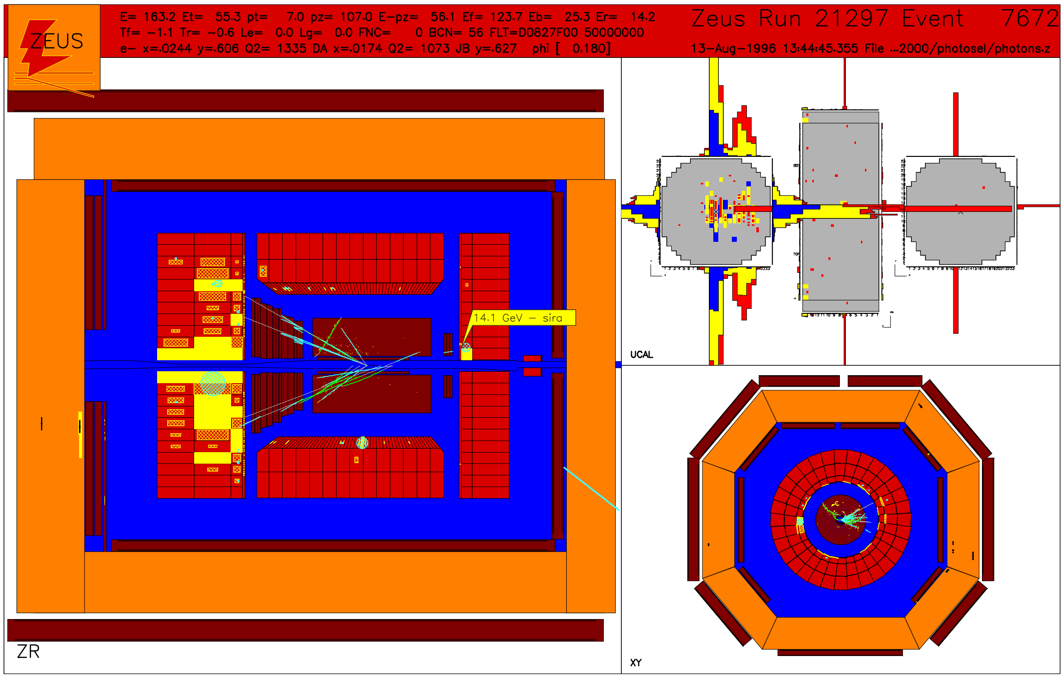

Figure 4.8: *A typical example of a deep inelastic prompt photon event in the ZEUS detector.*

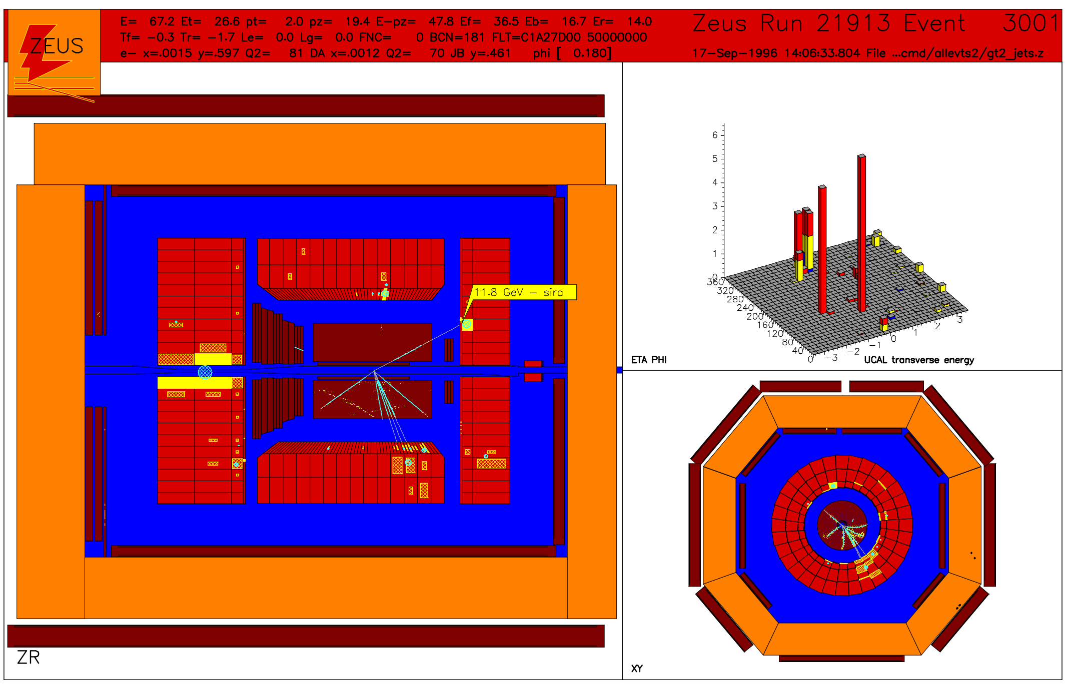

Figure 4.9: *A typical example of a deep inelastic prompt photon event in the ZEUS detector.*

4.7 Photon Reconstruction

The photon energy measured in the ZEUS detector is not quite identical to the actual energy of the photon measured. This is a result of energy being lost in passing through dead material in the detector. The possible effects of this process on the important kinematic variables of the photon ($E_T^\gamma, \eta^\gamma, \phi^\gamma$) can be examined using single photon Monte Carlo and comparing the difference between the true values generated and those reconstructed in the detector. These different situations will be referred to as true and reconstructed (rec) in this section. For each variable the difference between the true and reconstucted measurements is studied as a function of the variables $E^\gamma_{T,true}, \eta^\gamma_{true}$ and ϕ^γ_{true}. The effects are plotted in Figure (4.10). At this stage, the full range of energies generated, $3 \rightarrow 20GeV$ is considered, although this range is reduced for subsequent data analysis.

Looking at Figure (4.10), it can be seen that the variation between true and reconstructed values for the angular variables, η and ϕ is very small and does not require any correction applied. However the measured E_T^γ shows a disagreement between true and reconstructed values of around 0.2 to 0.3 GeV.

This significant discrepancy requires further treatment as this important variable is used as the basis for many cuts and for cross section kinematic region definition. The transverse energy of the photon seems to be lower when reconstructed than when generated. This difference shows no significant ϕ dependence but is not constant across the η range studied, showing a small variation. Therefore any correction to be applied must be done in bins of η^γ. The first plot from Figure (4.10) which shows $(E^\gamma_{T,true} - E^\gamma_{T,rec}) vs. E^\gamma_{T,true}$ is plotted again in 8 bins of η^γ corresponding to the photon pseudorapidity bins used in later stages of the analysis. This is shown in Figure (4.11).

The true energy of a photon can be related to its measured energy in the detector by fitting a straight line through the data points in each bin as shown

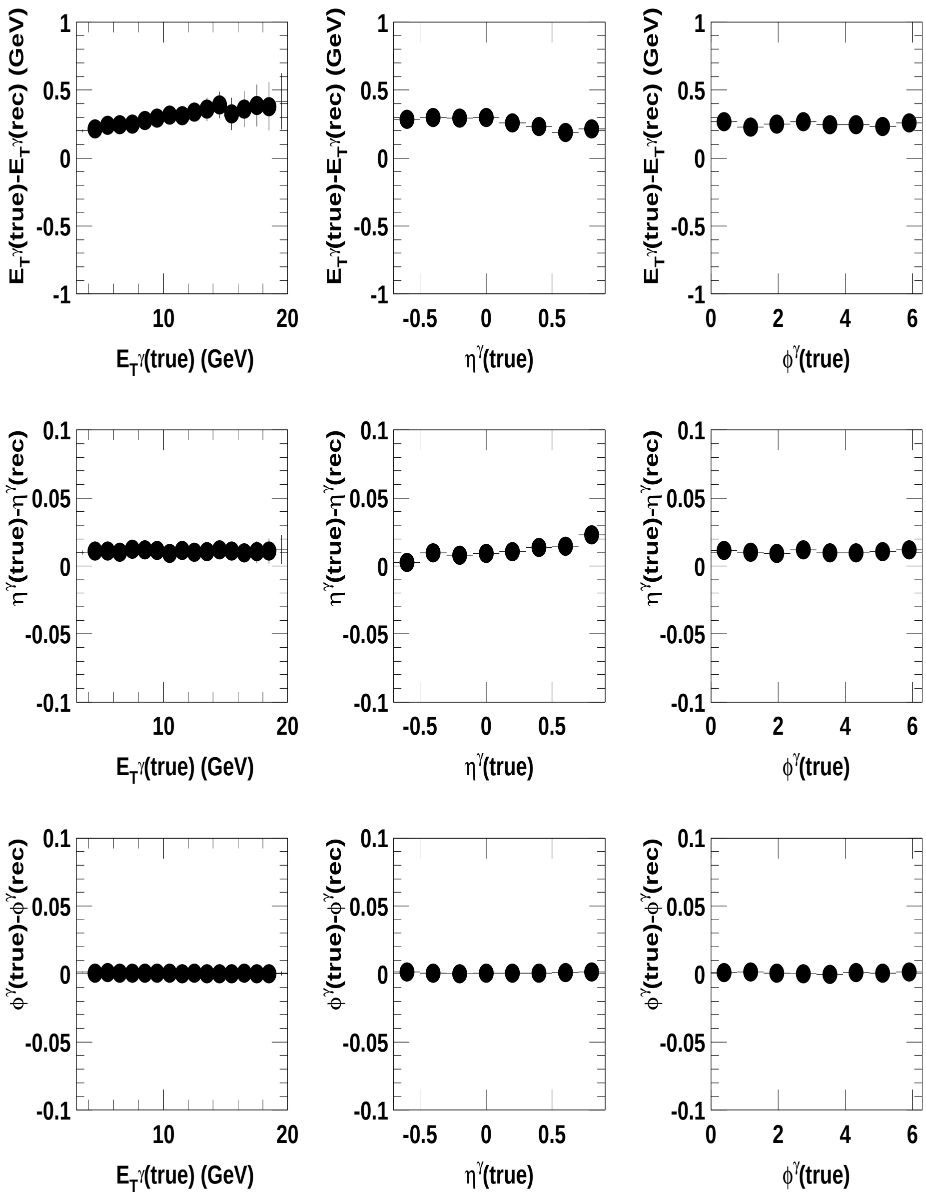

Figure 4.10: *Correlation of photon variables between the true values generated and those reconstructed in the detector. The top row of plots shows how the transverse energy difference varies as a function of (from left to right) $E^{\gamma}_{T,true}$, η^{γ}_{true} and ϕ^{γ}_{true}. The middle row of plots shows, in the same way, how the pseudorapidity difference varies and the final row of plots shows the behaviour of the azimuthal angular difference. The values plotted are mean values for each bin.*

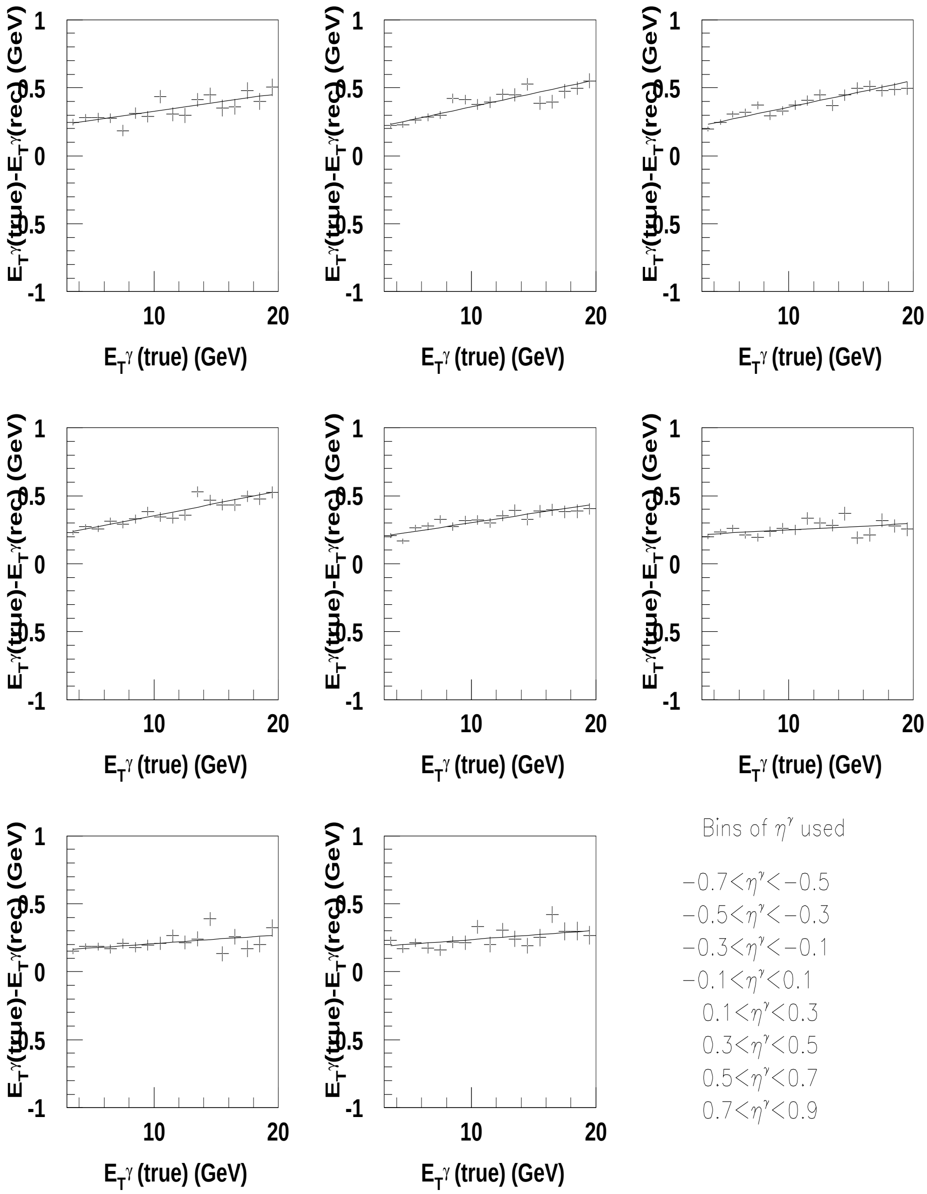

Figure 4.11: *The difference between generated and reconstructed values of E_T^γ is plotted in bins of photon pseudorapidity. Each plot is fitted with a straight line. The bins of pseudorapidity are listed and begin with the top left plot. The points plotted are the mean values for each bin.*

η^γ bin	M	C
$-0.7 < \eta^\gamma < -0.5$	0.013	0.196
$-0.5 < \eta^\gamma < -0.3$	0.020	0.162
$-0.3 < \eta^\gamma < -0.1$	0.019	0.163
$-0.1 < \eta^\gamma < 0.1$	0.018	0.175
$0.1 < \eta^\gamma < 0.3$	0.014	0.162
$0.3 < \eta^\gamma < 0.5$	0.005	0.201
$0.5 < \eta^\gamma < 0.7$	0.006	0.143
$0.7 < \eta^\gamma < 0.9$	0.007	0.168

Table 4.1: *Correction factors for photon E_T determined from studies of single photon Monte Carlo*

in Figure (4.11). The form of this straight line is given in Equation (4.9)

$$E_T^{true} - E_T^{rec} = M \times E_T^{true} + C \tag{4.9}$$

Equation (4.9) can be rearranged to give the form shown in Equation (4.10).

$$E_T^{true} = \frac{E_T^{rec} + C}{1 - M} \tag{4.10}$$

The correction factors extracted from the straight lines plotted in Figure (4.12) are given in Table (4.1). The errors on the correction factors are typically very small in comparison to the errors on the data and are neglected.

4.7.1 Photon Energy Resolution

By applying the correction factors in Table (4.1) to the detector level photon transverse energy the effect of this correction on the energy resolution can be evaluated. The energy resolution is defined as the difference between generator and detector level transverse energy. The resolution is calculated using both the uncorrected and corrected energies at detector level and both curves are plotted together to show the effect of the correction. This is shown in Figure (4.12).

From Figure (4.12) it is seen that applying the correction has the effect of shifting the resolution left, so it becomes centred closer to zero. It can be ascertained from Figure (4.12) that the photon energy correction is not a large effect.

4.8 Jet Reconstruction

To compare to theory calculations a subset of the inclusive prompt photon events consisting of those where the photon is accompanied by one jet is studied. A quark is emitted from the hard scattering subprocess but cannot exist independently as a coloured object and therefore undergoes a process of hadronisation into a 'jet' of colourless objects. Experimentally these jets are reconstructed from clusters of hadronic energy deposits in the detector.

4.8.1 Jet Finding

In high energy collisions, the outgoing partons from hard scattering subprocesses are often quarks or gluons. Because of their intrinsic colour these partons cannot continue to exist unaltered and must undergo a process of evolution into colourless objects. This process involves soft radiation and hadronisation processes which are not completely understood. An initial quark will become, through this hadronisation process, a 'jet' of hadrons which each have a small transverse momentum relative to the parent quark direction. The final local cluster of hadronic energy in the detector defines a 'jet', the experimental signature of a final state quark or gluon.

For each event in the inclusive data set, a jet finding program is run and the information on jets in the event is kept. This enables the measurement of both inclusive and photon + jet(s) from the same data sample.

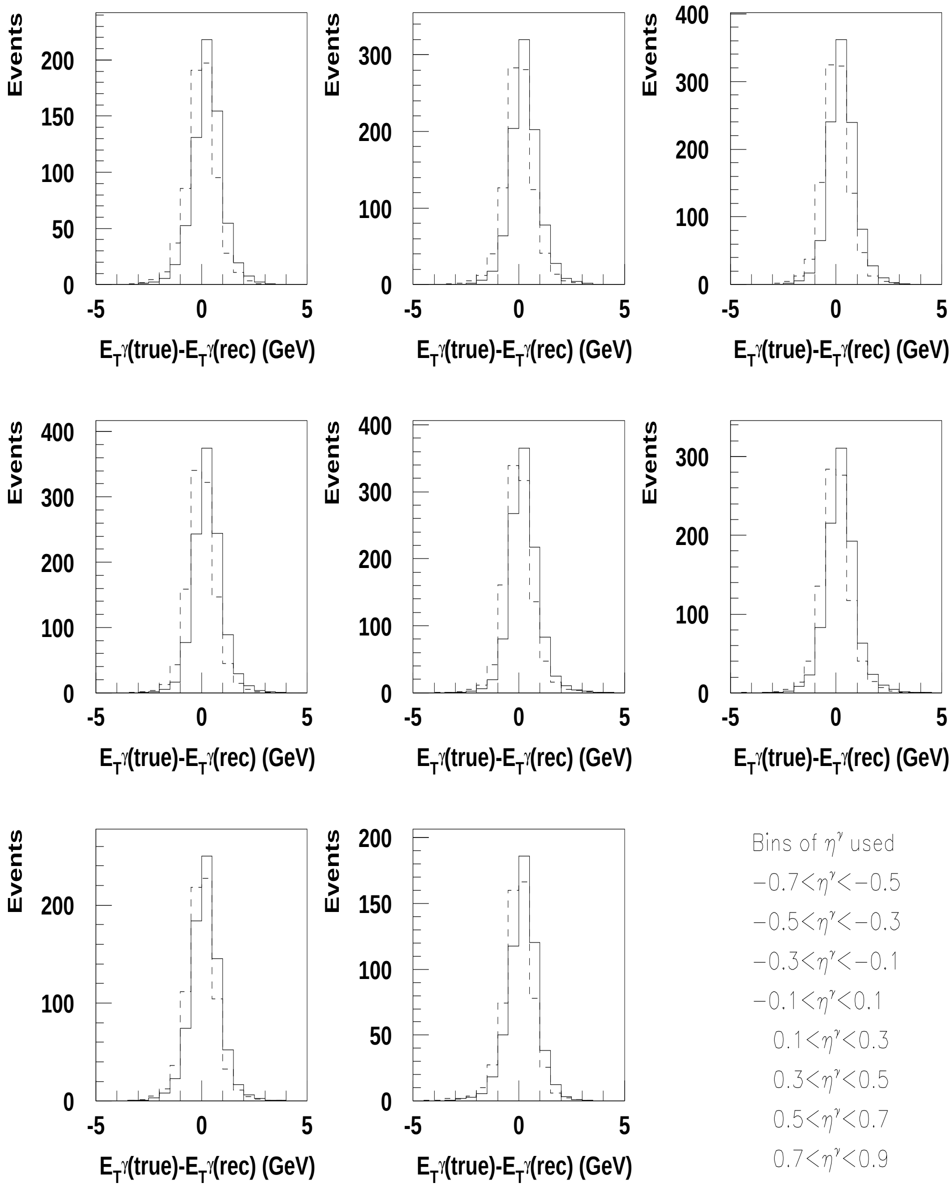

Figure 4.12: *Energy resolution, $E^{\gamma}_{T,true} - E^{\gamma}_{T,rec}$, for single photons in bins of photon pseudorapidity. The full curves show the resolution calculated using uncorrected values of the reconstructed transverse energy and the dotted curves show the resolution found using the corrected values of the reconstructed transverse energy. The bins of photon pseudorapidity used are listed in order, with the first plot at the top left.*

4.8.2 Jet Finding Algorithms

There are two distinct types of jet finding algorithm available for ZEUS analysis, based on clustering and cone jet reconstruction methods. These algorithms differ in the criteria by which particles are assigned as belonging to a particular jet or not.

4.8.3 The Cone Algorithm

Jet finding in both this analysis and the theory calculations used is performed using a cone algorithm. The cone algorithm is probably the most intuitive jet finder available. It searches for jets by clustering particles with trajectories in the same area of $\eta - \phi$ space. The ZEUS algorithm EUCELL [27] searches over a grid of cells in $\eta - \phi$ space and moves a window across the $\eta - \phi$ grid searching for clusters of energy.

EUCELL searches for clusters of energy which lie in the same cone of radius R in $\eta - \phi$ space. The cone radius used in this work is $R = 0.7$. EUCELL employs the concept of preclustering. A window of 3 cells by 3 cells in area is formed where these cells have approximate size $\Delta\eta^{gridcell} = \Delta\phi^{gridcell} = R/2$. This window is slid over the space and each window which has a minimum transverse energy is noted as a precluster, or potential jet , of pseudorapidity η^{jet} and azimuth ϕ^{jet}. For each potential jet other calorimeter cells which are within the cone radius are added to the jet, ie each cell, i with pseudorapidity η^i and azimuth ϕ^i, which satisfies the condition in Equation (4.11).

$$R_i = \sqrt{(\eta_i - \eta_{jet})^2 + (\phi_i - \phi_{jet})^2} < R \tag{4.11}$$

The process is repeated for each precluster with energy above the minimum.

According to the Snowmass convention [28], the transverse energy, E_T, pseudorapidity, η, and azimuth, ϕ, of a jet are calculated by summing over the particles in the jet and are defined in Equations (4.12) to (4.14).

$$E_T{}^{jet} = \Sigma_i E_{Ti} \tag{4.12}$$

$$\eta^{jet} = \frac{1}{E_T^{jet}} \Sigma_i E_{Ti} \eta_i \tag{4.13}$$

$$\phi^{jet} = \frac{1}{E_T^{jet}} \Sigma_i E_{Ti} \phi_i \tag{4.14}$$

4.8.4 Differences in Jet Variables between True and Reconstructed Values

Due to the nature of a jet, it is expected that the behaviour may vary significantly between hadron and detector level. Hadron level jets are identified by using the four-vectors of the final state hadrons from the Monte Carlo generation process as the input to the jet finding algorithm. As with the photon study, the difference between hadron and detector level in each of three variables, E_T, η and ϕ is studied as a function of each of these three variables. All jets with $E_T^{jet} > 3GeV$ are considered initially. For E_T^{jet} the ratio $E_{T,jet}^{true}/E_{T,jet}^{rec}$ is used instead of the difference. The correlation plots showing the difference between true and reconstructed values are shown in Figure (4.13).

From Figure (4.13) it can be seen first of all that the reconstruction of angular variables is good with little difference between hadron and detector level. Looking at the E_T comparison there is clearly a problem in reconstructing the jet at the correct E_T. This difference seems to have no ϕ dependence, although some small η dependence is noted. Hence any corrections to be applied should be applied in bins of the jet pseudorapidity. Also the E_T variation is much greater at low values of measured tranverse energy.

The correction factor to be applied to the data must be of the form given in Equation (4.15).

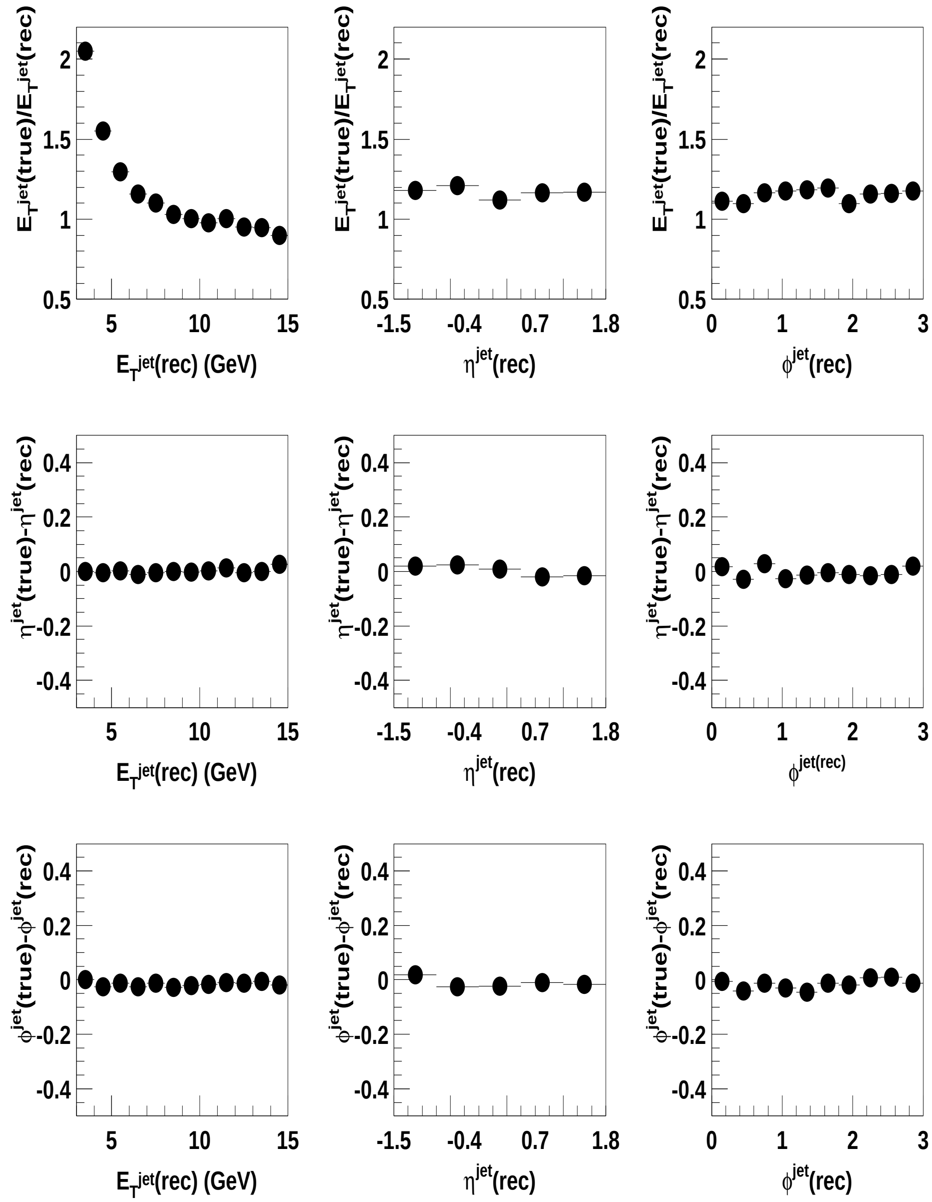

Figure 4.13: *Correlation of hadron and detector level variables for the highest* E_T *jet. The top row of plots describes how the ratio* $E^{true}_{T,jet}/E^{rec}_{T,jet}$ *behaves as a function of* $E^{rec}_{T,jet}$, η^{jet}_{rec} *and* ϕ^{jet}_{rec}*. The middle row of plots shows how the difference between true and reconstructed values of jet pseudorapidity behaves and the final row shows how the difference between true and reconstructed values of the azimuthal angle behaves. The points plotted are the mean values for each bin.*

η^{jet} bin	A	B	C
$-1.5 < \eta^{\gamma} < 0.0$	0.896	1.835	-0.518
$0.0 < \eta^{\gamma} < 0.4$	0.940	1.971	-0.531
$0.4 < \eta^{\gamma} < 0.7$	1.055	2.458	-0.706
$0.7 < \eta^{\gamma} < 1.8$	0.986	2.070	-0.566

Table 4.2: *Correction factors for jet E_T determined from studies of event Monte Carlo*

$$E_T^{true} = C(E_T^{rec}, \eta^{rec})E_T^{rec} \tag{4.15}$$

A similar procedure to the photon E_T is followed here, plotting the value E_T^{true}/E_T^{rec} in bins of η^{rec} and then fitting a curve to the plots. Four separate regions of η^{jet} are used. These plots are shown in Figure (4.14).

A curve of the form given in Equation (4.16) is fitted with three free parameters to the plots in Figure (4.14) to find the correction factors.

$$C(E_T^{rec}, \eta^{rec}) = A + exp(B + CE_T^{rec}) \tag{4.16}$$

The correction factors obtained from the fit are given in Table (4.2).

Due to the very large corrections which have to be applied to low energy jets, a cut is made on the minimum uncorrected jet energy of 4.5 Gev to remove these events. After correction, only jets with an energy above 6 GeV are accepted. The cut on uncorrected energy is necessary to prevent jets of very low energies which may pass the 6 GeV cut after the correction is accepted.

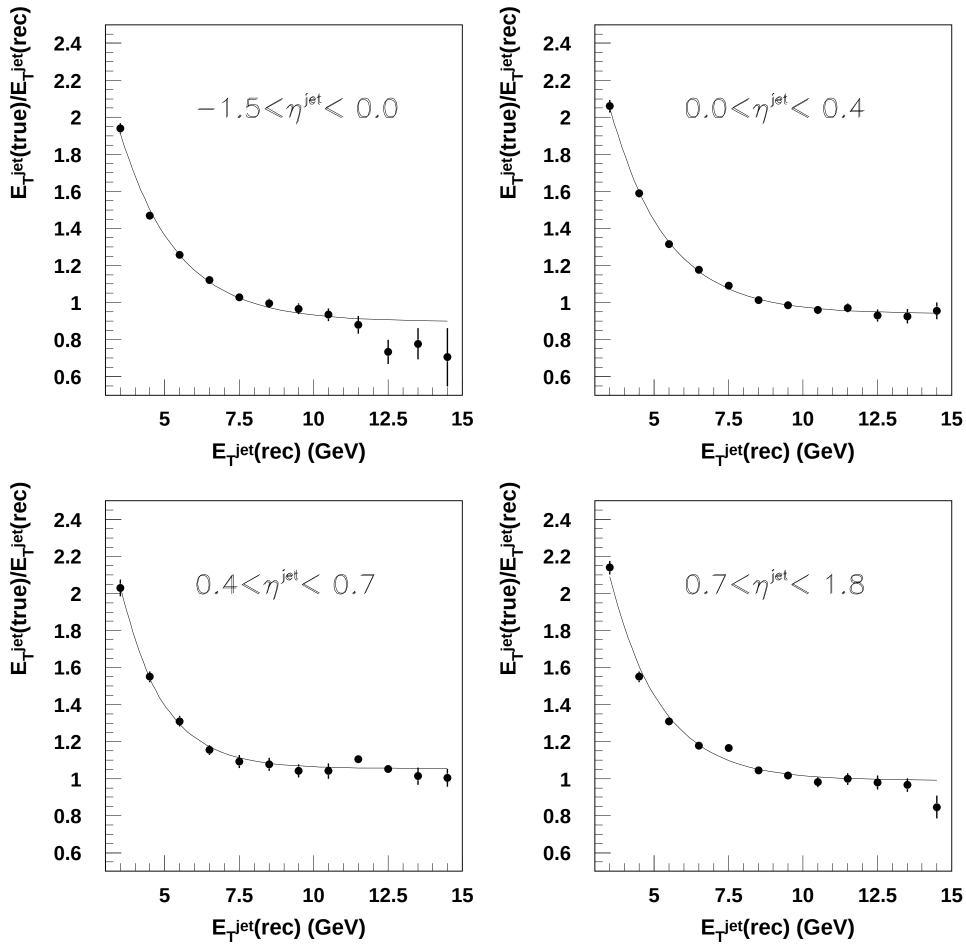

Figure 4.14: *The ratio $E^{true}_{T,jet}/E^{rec}_{T,jet}$ plotted in four bins of jet pseudorapidity. The points plotted are the mean values in each bin. The points in each bin are fitted with a curve of the form $y = A + exp(B + Cx)$.*

4.8.5 Jet Energy Resolution

The effects of applying these corrections to the jet energy as measured at detector level can be seen in Figure (4.15) where the E_T resolution is plotted using both uncorrected and corrected data.

It is seen from Figure (4.15) that the effect of applying the correction is to centre the the resolution about zero. A more significant effect is seen here than for the photon energy correction.

4.9 Jet Selection

After correction, jets are accepted which pass the cuts listed in Equations (4.17) to (4.18).

$$E_T^{jet} \geq 6GeV \tag{4.17}$$

$$-1.5 < \eta^{jet} < 1.8 \tag{4.18}$$

For each event, every jet which passes these cuts is stored, and then events which have only one suitable jet are accepted for the $(\gamma + jet)$ analysis.

4.10 Data Distributions

Although there still remains a neutral meson background in the data set it is interesting at this stage to look at some data distributions. The transverse energy and pseudorapidity of both the photon and the jet are shown in Figure (4.16).

It is seen from plot a) in Figure (4.16) that the photon pseudorapidity is higher in the backwards region while plot c) shows that the jet pseudorapidity peaks in the forward direction. It is also observed from plots b) and d) that the photon energy spectrum is softer than that of the jet.

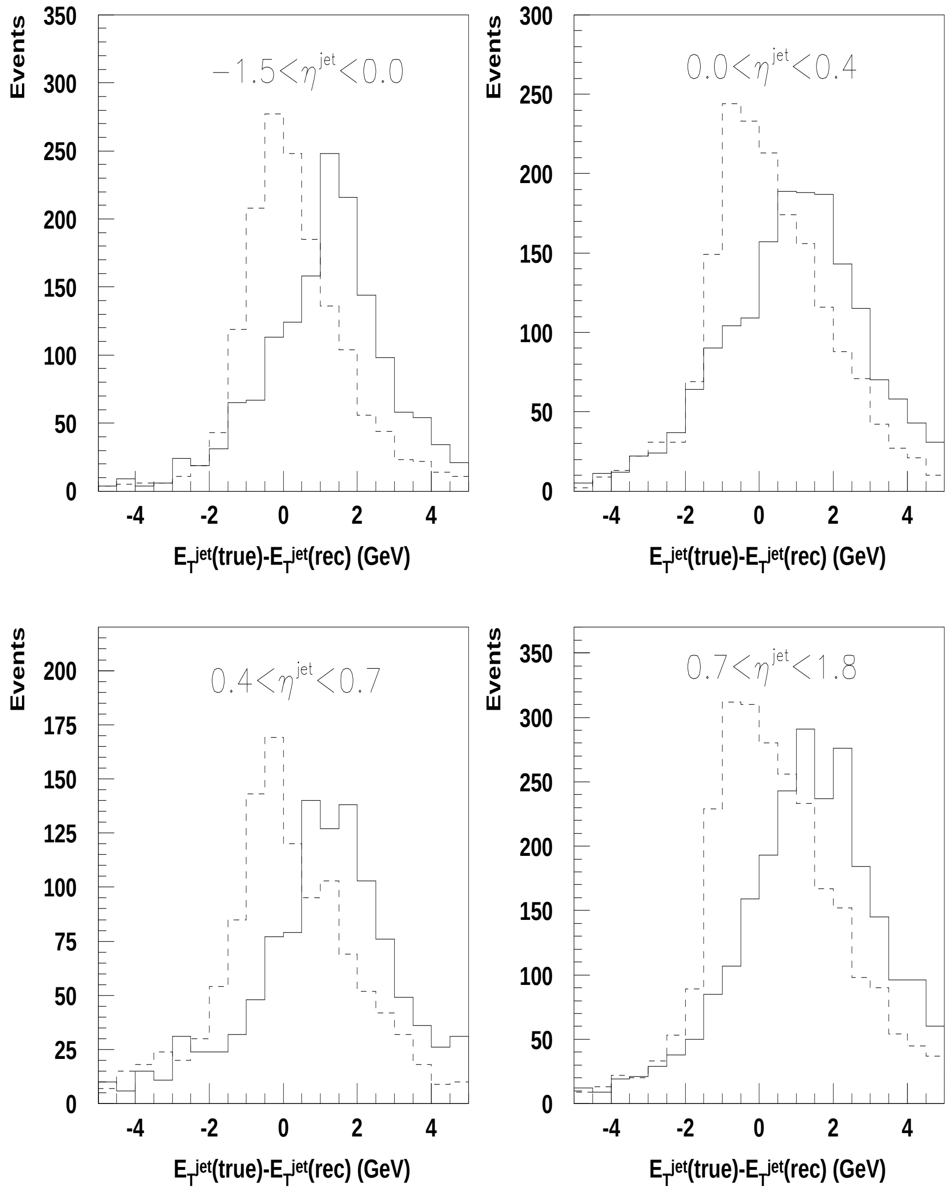

Figure 4.15: *Jet E_T resolution, $E_{T,jet}^{true} - E_{T,jet}^{rec}$, in bins of jet pseudorapidity. The full histograms show the resolution using uncorrected data and the dotted histograms show the resolution using corrected data. The minimum jet E_T accepted before correction is 4.5 GeV.*

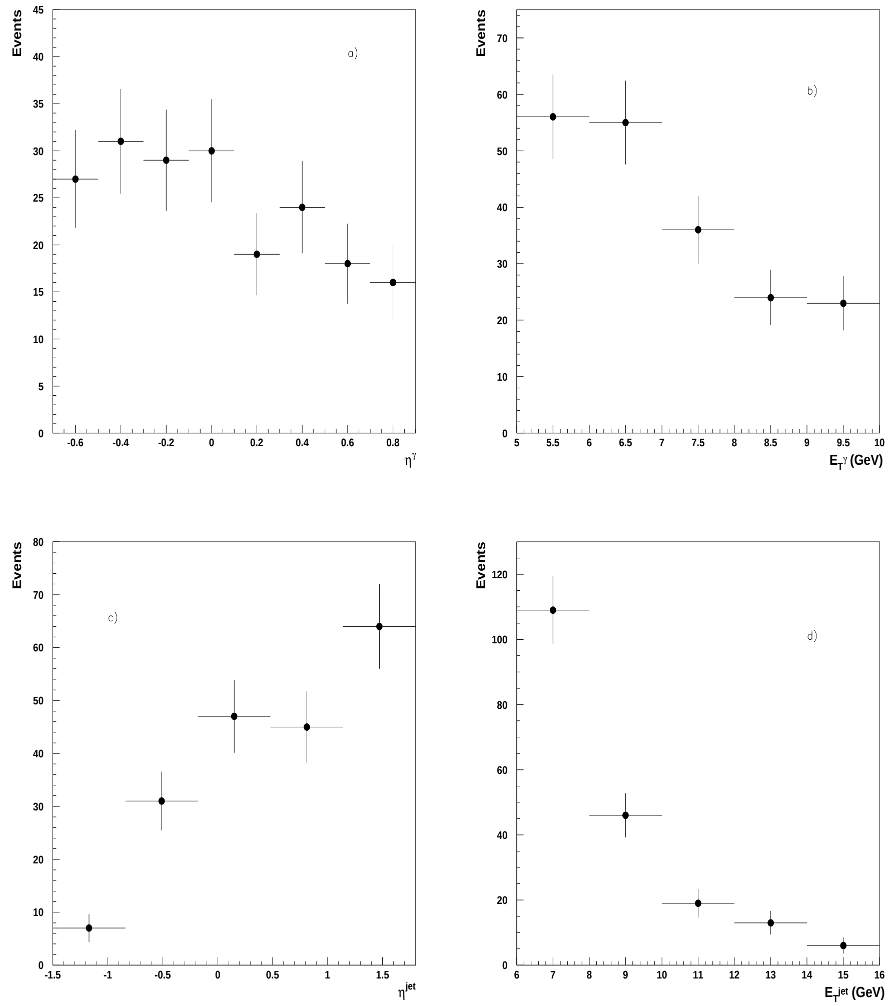

Figure 4.16: *Data distributions: a)η^{γ}, b) E_T^{γ}, c)η^{jet} and d)E_T^{jet}. These distributions are shown with statistical errors only.*

Chapter 5

Background Subtraction

The event selection procedure as discussed in the previous chapter is only able to provide a sample of isolated prompt photon *candidates*. However this sample is still contaminated by neutral mesons which decay to two or more photons with a narrow opening angle. The results of these decays are indistinguishable from single photons to an electron finder which searches merely for an electromagnetic cluster requiring no information on the cluster width or surroundings.

The particles mostly responsible for the sample contamination are π^0 and η mesons. These particles mimic photons in the electromagnetic calorimeter, neutral particles with no tracks which exhibit similar energies to actual prompt photons. It is not possible to make further cuts to unambiguously separate the photon signal from the neutral meson background so the the signal must be statistically extracted. It is expected that photons and neutral mesons will have slightly different cluster shapes in the calorimeter.

This neutral meson background is subtracted using the method developed for previous prompt photon analyses in photoproduction [29, 30]. The method involves measuring two parameters of the electromagnetic cluster shape in the calorimeter.

5.1 Neutral Meson Decay Processes

After making cuts to suppress the contribution from other leading order photon producing processes the major background to the analysis is misidentification of final state neutral mesons, η and π^0, as photons. The decay processes which contribute to the background found are listed in Equations (5.1), (5.2) and (5.3) [31].

$$\pi^0 \rightarrow \gamma\gamma \text{ Branching Ratio } 98.8\% \tag{5.1}$$

$$\eta \rightarrow \gamma\gamma \text{ Branching Ratio } 39\% \tag{5.2}$$

$$\eta \rightarrow \pi^0\pi^0\pi^0 \text{ Branching Ratio } 32\% \tag{5.3}$$

In the decay process in (5.3) each π^0 will probably further decay to two photons, giving a six photon final state.

The final states of these decays can be mistaken for single photons when the photons end up too close together to be individually resolved. To further illustrate this, it is helpful to consider decays which results in two photons and establish the final separation in the calorimeter for different starting energies.

The opening angle between two photons from a π^0 decay is given in Equation (5.4).

$$\alpha = 2 * \sin^{-1}\left[\frac{m_{\pi^0}}{2 * \sqrt{E_1(E_{\pi^0} - E_1)}}\right] \tag{5.4}$$

The minimum opening angle between the two photons produced occurs when they have equal energy. The minimum final distance between the photons corresponds to this minimum opening angle and is given in Equation (5.5).

$$\Delta_{min} = 2 * \frac{123.2}{\sin\theta_{\pi^0}} * \tan\left[sin^{-1}\left(\frac{m_{\pi^0} * \sin\theta_{\pi^0}}{E_{T,\pi^0}}\right)\right] \tag{5.5}$$

In Equations (5.4) and (5.5) E_{π^0} and m_{π^0} are the energy and mass of the decaying pion. The energies of the two photons are E_1 and hence, $E_{\pi^0} - E_1$. To find the minimum distance between the photons in an $\eta \rightarrow \gamma\gamma$ decay, the energy and mass used are that of the η meson. The value 123.2 is the radial distance, (in cm) of the barrel calorimeter from the interaction region and is the distance travelled from decay to detection.

For the relevant photon energy range of 5 to 10 GeV, Equation (5.5) gives the minimum separation of the two photons from the decay to be between 3.3cm and 6.7cm. For the photons from an η decay the distances are wider, between 13.5cm and 27.2cm. (The wider distances are for the lower energy particles). Therefore, it is possible to distinguish between the three types of particle in the BCAL where the calorimeter cells measure $5cm \times 23cm$, with each cell having a length of 5cm along the Z axis.

5.2 Calorimeter Cluster Shape

Two variables describing the size and energy distribution of the electromagnetic clusters in the calorimeter are introduced and defined in this section.

5.2.1 $< \delta Z >$

The neutral meson background can be modelled using straightforward single particle Monte Carlos of each involved particle, γ, π^0 and η. In the photoproduction analysis it was discovered that the cluster shapes of different types of particle varied significantly.

The first variable, $< \delta Z >$ is the energy-weighted mean width of the cluster in the Z direction, i.e. along the beam direction through the ZEUS detector, defined as follows:

$$< \delta Z >= \frac{\Sigma \left(|Z_{cell} - Z|\right) E_{cell}}{\Sigma E_{cell}} \tag{5.6}$$

In Equation (5.6), Z_{cell} is an integer counting the cell number in Z. Recall, from Chapter 3, that the BCAL is segmented into 5cm strips in Z. Z is the energy-weighted mean of Z_{cell} and cluster. E_{cell} is the energy contained within a cell.

The $< \delta Z >$ distributions for the three types of single particles are shown in Figure (5.1).

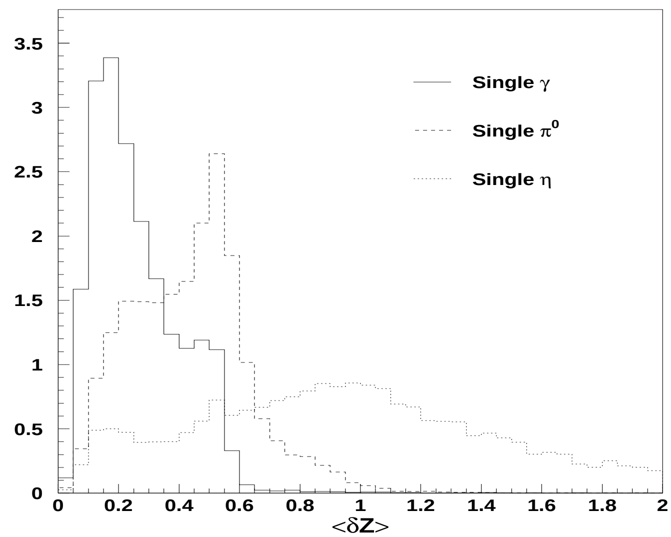

Figure 5.1: *$< \delta Z >$ from single particle Monte Carlo studies. Each curve is normalised to an area of one. Each particle type has been generated with a flat E_T distribution and reweighted to better reflect the data. These curves are for particles with $-0.7 < \eta < 0.9$ and $5 < E_T < 10GeV$.*

It is observed from Figure (5.1) that the photons have a peak around 0.2, with virtually no tail, while the pions peak at around 0.5 and the eta distribution is much flatter with a long tail extending to values beyond 2. It is seen that above values of 0.65 there is almost no photon contribution so this region is used to fix the ratio of π^0s to ηs for a fit, as described in Section (5.3).

The $< \delta Z >$ distribution for prompt photon candidate events in the 96-00 ZEUS data set is shown in Figure (5.2).

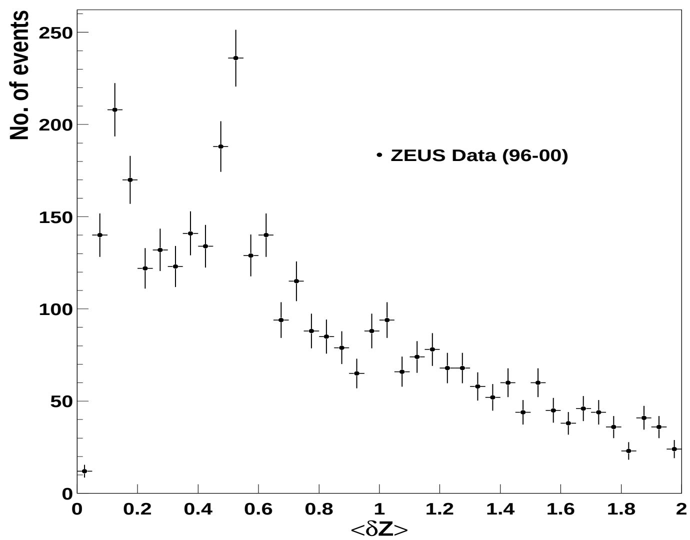

Figure 5.2: *$< \delta Z >$ distribution of prompt photon candidate events in the ZEUS 96-00 data set for* $5 < E_T^\gamma < 10 GeV$ *and* $-0.7 < \eta^\gamma < 0.9$

It is noted from Figure (5.2) that a similar shape can be seen to the combined single particle plot in Figure (5.1), with two sharp peaks corresponding to photon and pion components and a long tail of etas and other neutral mesons.

Studying both plots, it can be determined that the photon peak is not sufficiently well-represented by the Monte Carlo, with the data offset to the right of the Monte Carlo peak, hence a second parameter is introduced to allow the subtraction to be done. The offset in the $< \delta Z >$ plot is not important as this region of the plot will not be used for the subtraction. It is thought that this discrepancy between the data and the Monte Carlo stems from an inability of the Monte Carlo to correctly reproduce the fine details of the electromagnetic shower simulation in magnetic fields.

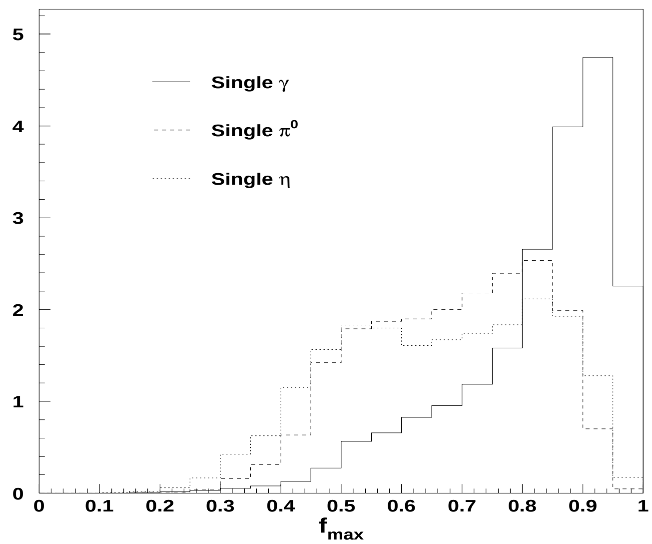

Figure 5.3: *f_{max} from Single Particle MC Studies. Distributions are for particles of $-0.7 < \eta < 0.9$, $5 < E_T < 10GeV$ and $< \delta Z >< 0.65$. Each curve is normalised to an area of one.*

5.2.2 f_{max}

The new quantity which is used to carry out the main part of the subtraction, f_{max}, is defined as the ratio of energy in the highest energy cell of a cluster to the total energy of the cluster, given by Equation (5.7).

$$f_{max} = \frac{\text{Energy of highest energy cell in cluster}}{\text{Total energy of cluster}} \tag{5.7}$$

The area normalised distributions of f_{max} for the three types of single particle are shown together in Figure (5.3). It can be seen in Figure (5.3) that the π^0 and η curves display a similar shape, but that the photon is peaked very strongly towards higher values, consistent with the knowledge that a photon will not decay and its energy should be contained almost entirely in one cell, unless it should impact on the calorimeter close to a cell boundary.

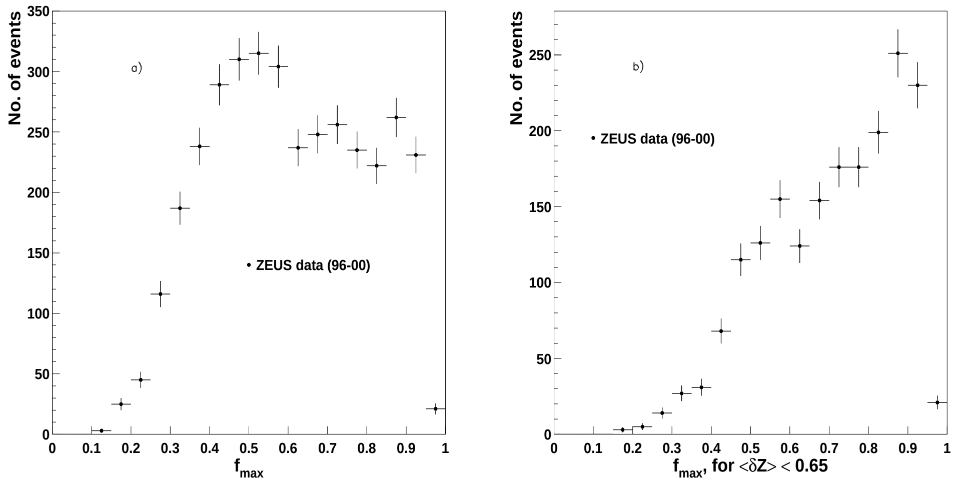

Figure 5.4: f_{max} *distribution of ZEUS data from 96-00 a) before cut on* $< \delta Z >> 0.65$ *events and b) having applied this cut.*

The f_{max} distribution for prompt photon candidates from the ZEUS 96-00 data is shown in Figure (5.4), before and after making a cut to remove all events with $< \delta Z >> 0.65$. The effect of this cut is to reduce the presence of background events and highlight the photon peak as would be expected.

The single particle simple Monte Carlo events are generated with a flat E_T distribution and must be reweighted to represent the energy spectrum of the data. Plotting $< \delta Z >$ for ZEUS data showed 2 clear peaks and a long tail (Figure (5.2)). This plot can be divided into three rough regions representing γs, π^0s and ηs. Plotting the E_T distribution in each of these regions on a logarithmic scale gives the factors to reweight the single particle Monte Carlo which is originally generated with a flat E_T distribution from 3 to 20 GeV.

5.2.3 f_{max} Correction Factors

As with the $< \delta Z >$ distribution, there is some problem in modelling the particles' curves correctly with the f_{max} variable. However, in the photoproduction analysis, a correction factor was calculated for the γ and π^0 f_{max} distributions to shift the peak closer to that seen in the data. Full details of this correction procedure are presented in [29] and [30].

The correction applied is of the form detailed in Equation (5.8).

$$f_{max}(corrected) = f_{max}(uncorrected) * factor \tag{5.8}$$

where $factor$ is the correction factor to be applied. During the correction procedure the correction factors were found to be pseudorapidity dependent. The correction factor for the photon f_{max} is calculated using Equation (5.9).

$$factor = -(0.104 * \eta^2) + (0.002 * \eta) + 1.046 \tag{5.9}$$

Similarly, the correction factor to be applied to the π^0 f_{max} distribution is defined in Equations (5.10) and (5.11).

$$factor = 1.0 + [(factor' - 1.0) * (1.8 - \frac{0.72}{f_{max}(uncorrected)})] \tag{5.10}$$

$$factor' = -(0.037 * \eta^2) + 1.010 \tag{5.11}$$

These same corrections are applied to all single particle distributions before they are used. Later, a systematic uncertainty is introduced which allows these corrections to vary within their error bounds.

5.3 Subtraction Method

The subtraction method is that developed for the photoproduction analysis as previously discussed. The ratio of $\pi^0 s$ to ηs is fixed from the region $0.65 <<$

$\delta Z >< 2.0$ and is thereafter kept constant throughout the subtraction. This is done by fitting a combination of the three types of single particles to the data events with $< \delta Z >> 0.65$. When the best fit is found, the two different background components are added together and a combined background is used to extract the final signal. It is found that pi^0 and η mesons contribute approximately equally to the observed background. The actual subtraction is performed using the f_{max} distributions of data, photons, pions and eta mesons. A particular physics plot, e.g., η^γ is plotted in two regions of $f_{max} > 0.75$ and $f_{max} \leq 0.75$. These will be referred to as signal-enriched and background-enriched, or simply 'good' and 'poor'. Assuming the fraction of events passing the f_{max} cut is reasonably constant over the whole region of the plot then it is sufficient to perform only one subtraction for the plot.

5.3.1 f_{max} Subtraction in Different Regions

It is possible that the the distributions of single particle Monte Carlo and hence the effect of the subtraction will vary significantly over the kinematic range of the photon candidate under consideration. To establish the validity of this hypothesis it is first necessary to study the effect of the background subtraction over the full photon pseudorapidity range relevant for use in the analysis, that which corresponds to the ZEUS BCAL region. The variation in subtraction power over the relevant η range is shown in Figure (5.5)

From Figure (5.5) it is immediately observed that a significant difference between the fraction of photons passing the cut, around 80%, and the fraction of π^0 or η mesons which pass the cut, around 30%. However this difference is reasonably constant over the pseudorapidity range in question and doesn't indicate any real dependence on that variable.

For the transverse energy the possible analysis range of $4 \rightarrow 15 GeV$ is studied and the results of this are shown in Figure (5.6).

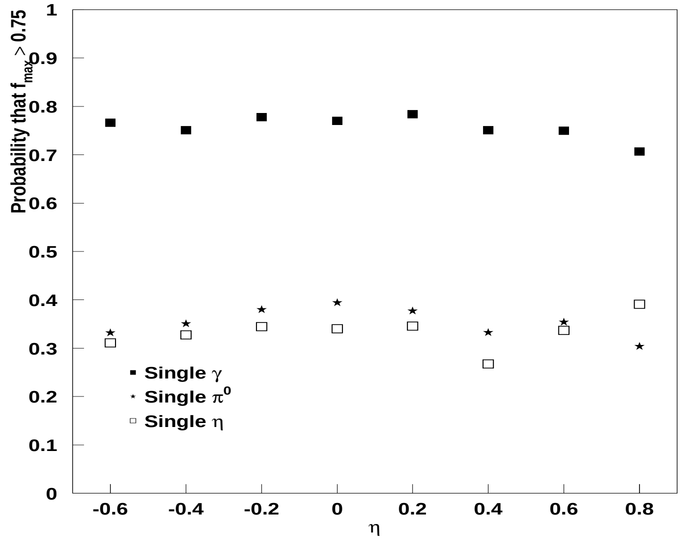

Figure 5.5: *The probabilities of single particles events having $f_{max} > 0.75$ for the η range appropriate to the ZEUS BCAL.*

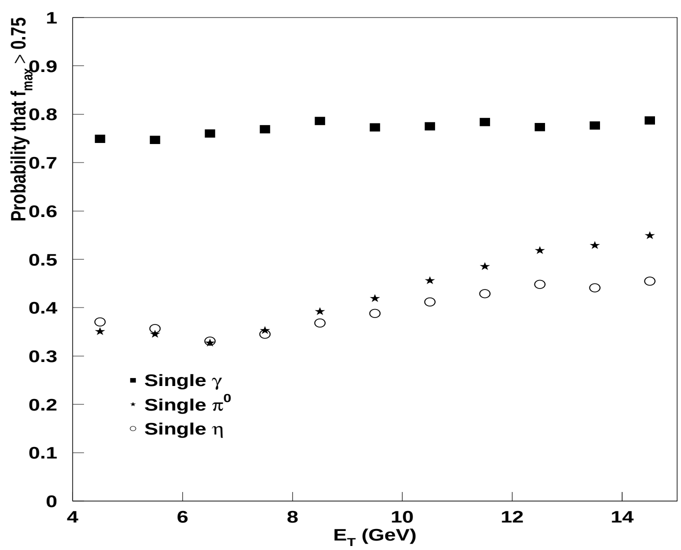

Figure 5.6: *The probabilities of single particles events having $f_{max} > 0.75$ for the likely E_T^{γ} analysis range.*

In Figure (5.6) it can be seen that on moving to higher values of E_T the fraction of photons passing the cut remains steady but the fraction of background events passing the cut increases significantly. This is due to the narrowing of the clusters at high E_T as the decaying particles have smaller opening angles. As a result of this, the energy range of the analysis is limited to a maximum of 10 GeV and as a further precaution the photon transverse energy plot is divided into bins of E_T before subtraction.

5.3.2 Signal Extraction

Beginning from the good and poor physics plots the true photon signal and neutral meson background are extracted in the following way using Equations (5.12) and (5.13).

$$N_{f_{max}>0.75} = \alpha N_{signal} + \beta N_{bgd} \tag{5.12}$$

$$N_{f_{max}<0.75} = (1-\alpha) N_{signal} + (1-\beta) N_{bgd} \tag{5.13}$$

Rearranging Equations (5.12) and (5.13) gives expressions for N_{signal} and N_{bgd} from which the statistical errors on these distributions can be evaluated using Equations (5.14) and (5.15).

$$\sigma^2_{signal} = \frac{1}{(\alpha-\beta)^2}\{(1-\beta)^2\sigma^2_{good} + \beta^2\sigma^2_{poor}\} \tag{5.14}$$

$$\sigma^2_{bgd} = \frac{1}{(\alpha-\beta)^2}\{(1-\alpha)^2\sigma^2_{good} + \alpha^2\sigma^2_{poor}\} \tag{5.15}$$

In Equations (5.12) to (5.15), α is defined as the probability that photon events satisfy f_{max} greater than 0.75 and β is defined as the probability that background events satisfy the same condition. The equations above are solved for each bin of a physics plot to provide the final extracted signal and background plots.

5.4 Comparison of f_{max} and $< \delta Z >$ for Data and Monte Carlo

The data are shown compared with a combination of the three types of single particle Monte Carlo with the ratios for combination calculated in the subtraction. Three curves are shown, single η mesons, a combination of π^0 and η mesons and finally a combination of all three particle types. Figure (5.7) shows the comparisons of $< \delta Z >$ and f_{max} for the full kinematic region. In Figure (5.8) these comparisons are shown in three bins of E_T^γ.

The comparisons for the full inclusive kinematic region are displayed in Figure (5.7). This is the set of all data events which satisfy all the selection cuts and have no jet requirements imposed.

These inclusive plots are also divided into three bins of E_T^γ, $5 \rightarrow 6$ GeV, $6 \rightarrow 8$ GeV and $8 \rightarrow 10$ GeV, and these individual bin plots are shown in Figure (5.8).

These comparisons are carried out in the same way for the $(\gamma + jet)$ process, although this is much more heavily dominated by statistical errors. The resulting plots for the full kinematic region are given in Figure (5.9). Figure (5.9) immediately shows that the $(\gamma + jet)$ process has a much less significant contribution from background events. As before, the comparisons are also carried out in the three bins of E_T^γ defined previously. These plots are given in Figure (5.10).

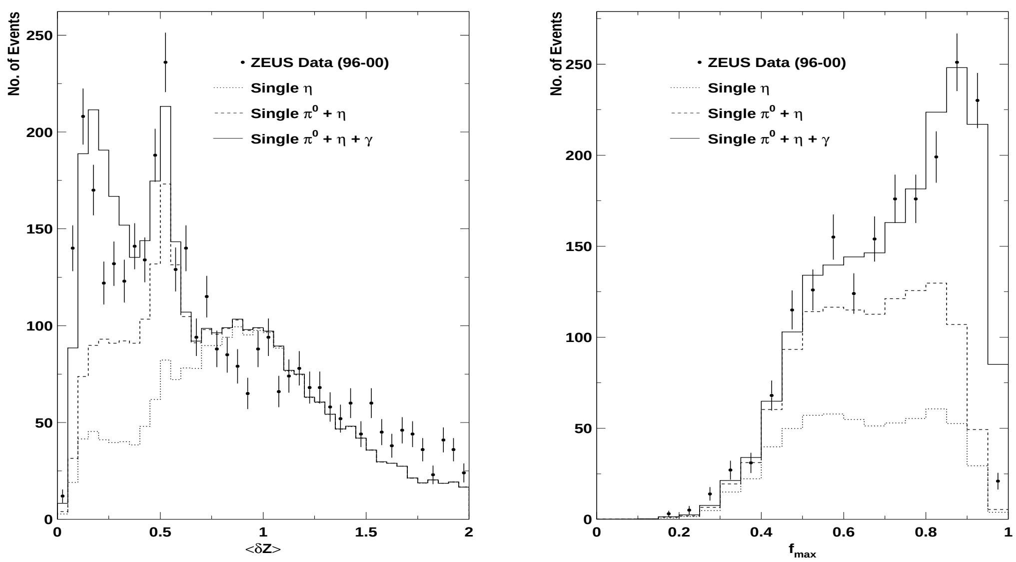

Figure 5.7: *Comparisons between data and single particle Monte Carlo of* $< \delta Z >$ *and* f_{max} *for the full inclusive data set.*

5.5 Extracted Signal and Background for the Inclusive Prompt Photon Process

For the inclusive prompt photon process, the most interesting variables to study are those of the prompt photon itself, namely the pseudorapidity and transverse energy. It is also interesting to look more closely at the kinematics of the whole event, through Q^2 and y which are calculated from the scattered electron. It is expected that as the single particle subtraction methods is only correlated to parameters of the photon then for the non-photon specific quantities it may be assumed that the subtraction procedure is independent of the variable.

The extracted photon signal and meson background plots for Q^2 and $y_{electron}$ for the inclusive process are shown in Figure (5.11).

The extracted signal and background region plots for η^γ and E_T^γ are shown in Figure (5.12).

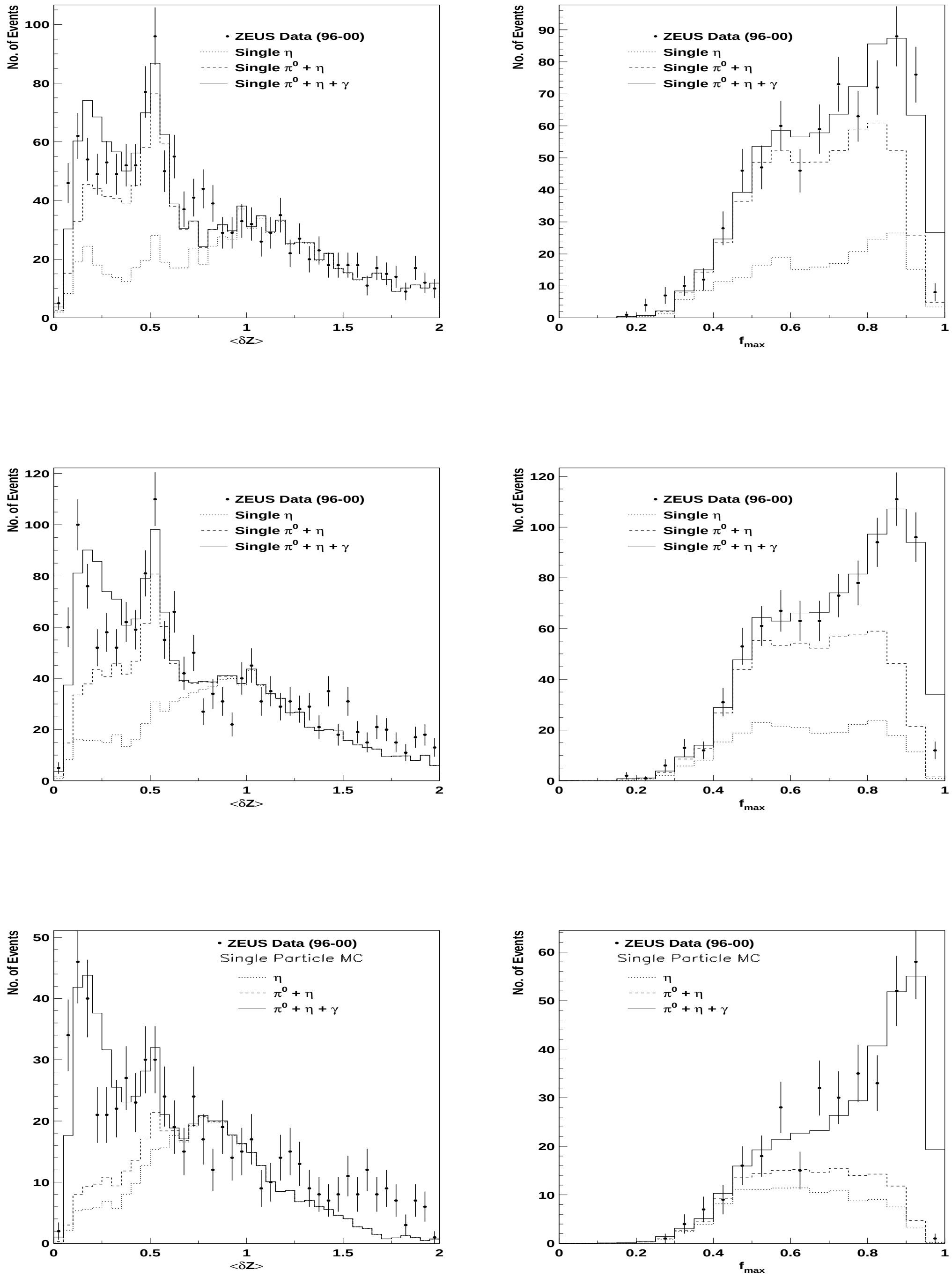

Figure 5.8: *Comparisons between data and single particle Monte Carlo of* $< \delta Z >$ *and* f_{max} *in bins of* E_T^γ *for the inclusive process. The bins of* E_T^γ *used are* $5 \rightarrow 6GeV$, $6 \rightarrow 8GeV$ *and* $8 \rightarrow 10GeV$. *Each row of plots represents an* E_T *bin, with the lowest energy bin at the top.*

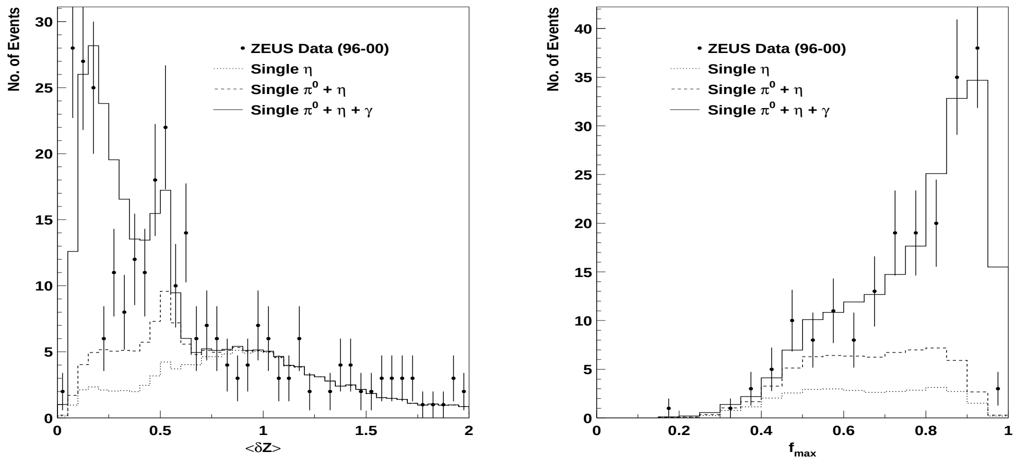

Figure 5.9: *Comparisons between data and single particle Monte Carlo of* $< \delta Z >$ *and* f_{max} *for the full* $(\gamma + jet)$ *kinematic region*

The plots show the number of events after subtraction in the signal and background regions. Although corresponding to the same kinematic region there are slight differences in the number of signal events between the different physics plots arising from statistical fluctuations in the background subtraction procedure.

5.6 Extracted Signal and Background for the $(\gamma + jet)$ Process

For the case of a prompt photon accompanied by a jet, there are also the jet variables available for study. The jet variables, η^{jet} and E_T^{jet} are available for study as well as those quantites studied in the inclusive process. Again, the extracted signal and background are shown for each physics plot, beginning with the kinematic plots, Q^2 and $y_{electron}$ in Figure (5.13). The extracted photon signal and meson background plots describing the photon are given in Figure (5.14). The

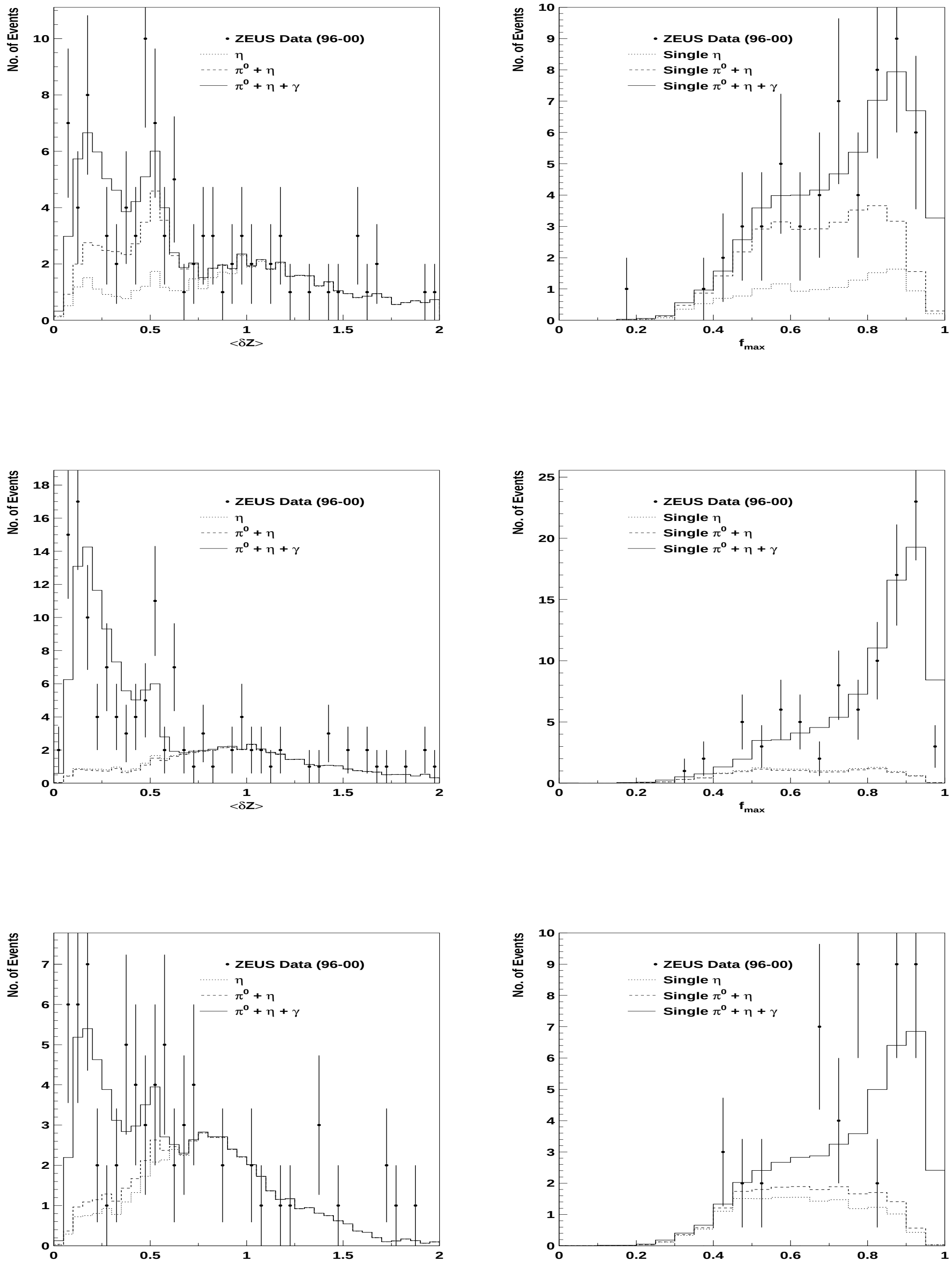

Figure 5.10: *Comparisons between data and single particle Monte Carlo of* $<\delta Z>$ *and* f_{max} *in bins of* E_T^{γ} *for the* $(\gamma + jet)$ *process. The bins are* $5 \rightarrow 6GeV$, $6 \rightarrow 8GeV$ *and* $8 \rightarrow 10GeV$. *Each row of plots represents an* E_T *bin, with the lowest energy bin at the top.*

Events surviving selection	1875
'good' events, $f_{max} > 0.75$	877
'poor' events, $f_{max} \leq 0.75$	998
Signal events	570
Background events	1305

Table 5.1: *Number of events before and after background subtraction for the inclusive process.*

extracted photon signal and meson background plots for those variables describing the jet are given in Figure (5.15).

5.7 Effect of Subtraction on Signal to Background Ratio

From Figures (5.7) and (5.8) it can be seen that in general more background events are found than signal events, although as expected the signal to background ratio improves in the $(\gamma + jet)$ case as further strict restrictions are placed on the surviving events. A summary of the number of events surviving the background subtraction in the inclusive process are given in Table (5.1).

It is observed that in Table (5.1) that a significant fraction of events have been misidentified as prompt photon events prior to the subtraction process. From the almost 50% of events which satisfy the f_{max} cut, the number of surviving signal events is only about one third of the total number of events. A summary of the number of events surviving the background subtraction in the $(\gamma + jet)$ process are given in Table (5.2).

It is seen from Table (5.2) that contrary to the inclusive case, here there are more events satisfying the f_{max} cut than are failing and the ratio increases slightly further in favour of the good events after the subtraction, suggesting that

Events surviving selection	194
'good' events, $f_{max} > 0.75$	115
'poor' events, $f_{max} \leq 0.75$	79
Signal events	122
Background events	72

Table 5.2: *Number of events before and after background subtraction for the* ($\gamma +$ *jet*) *process.*

the imposition of a jet requirement is beneficial to the signal extraction, while simultaneously reducing the available statistics.

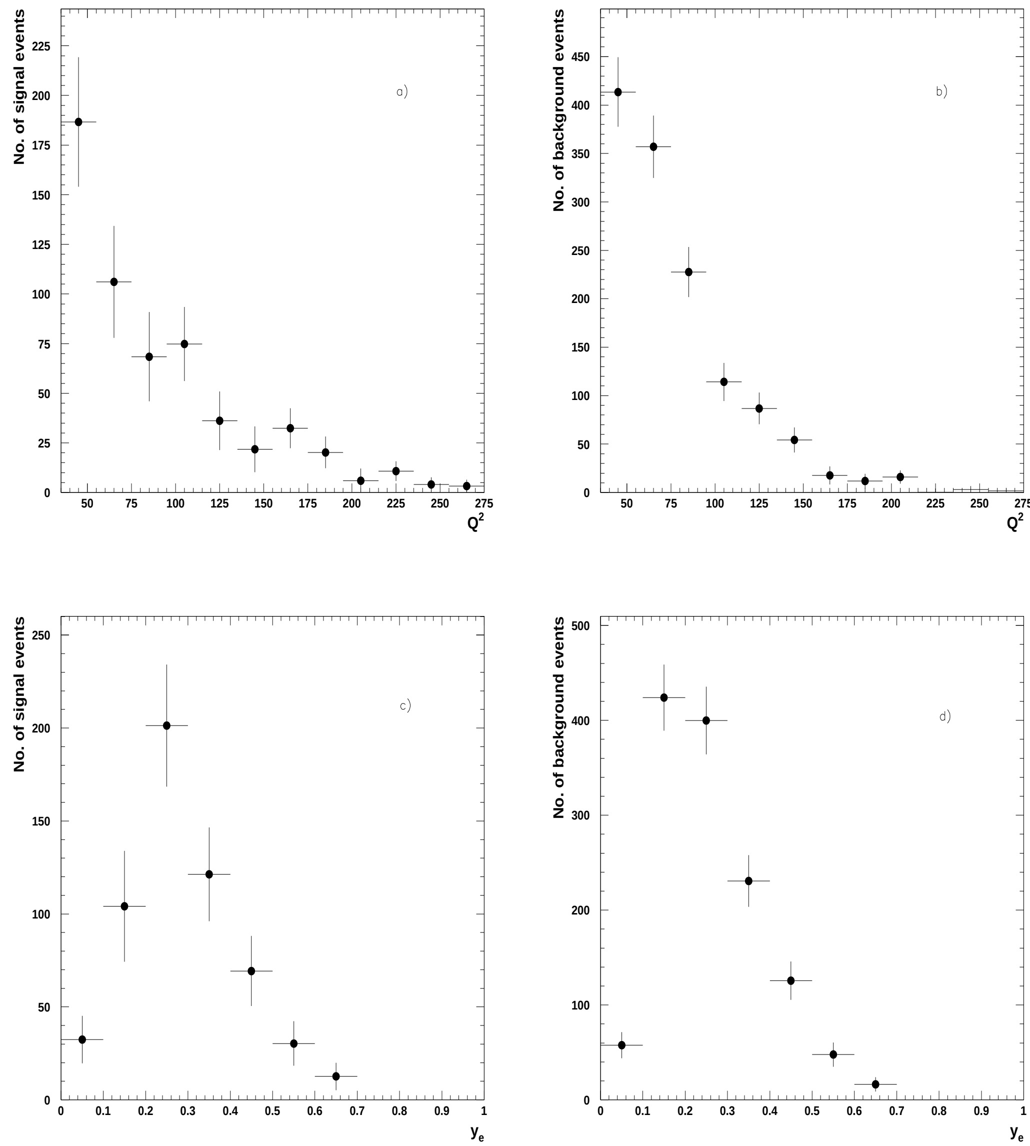

Figure 5.11: *Extracted signal and background plots for the inclusive prompt photon process. a) Q^2 signal, b) Q^2 background, c) $y_{electron}$ signal and d) $y_{electron}$ background. The plots show the number of events in each region.*

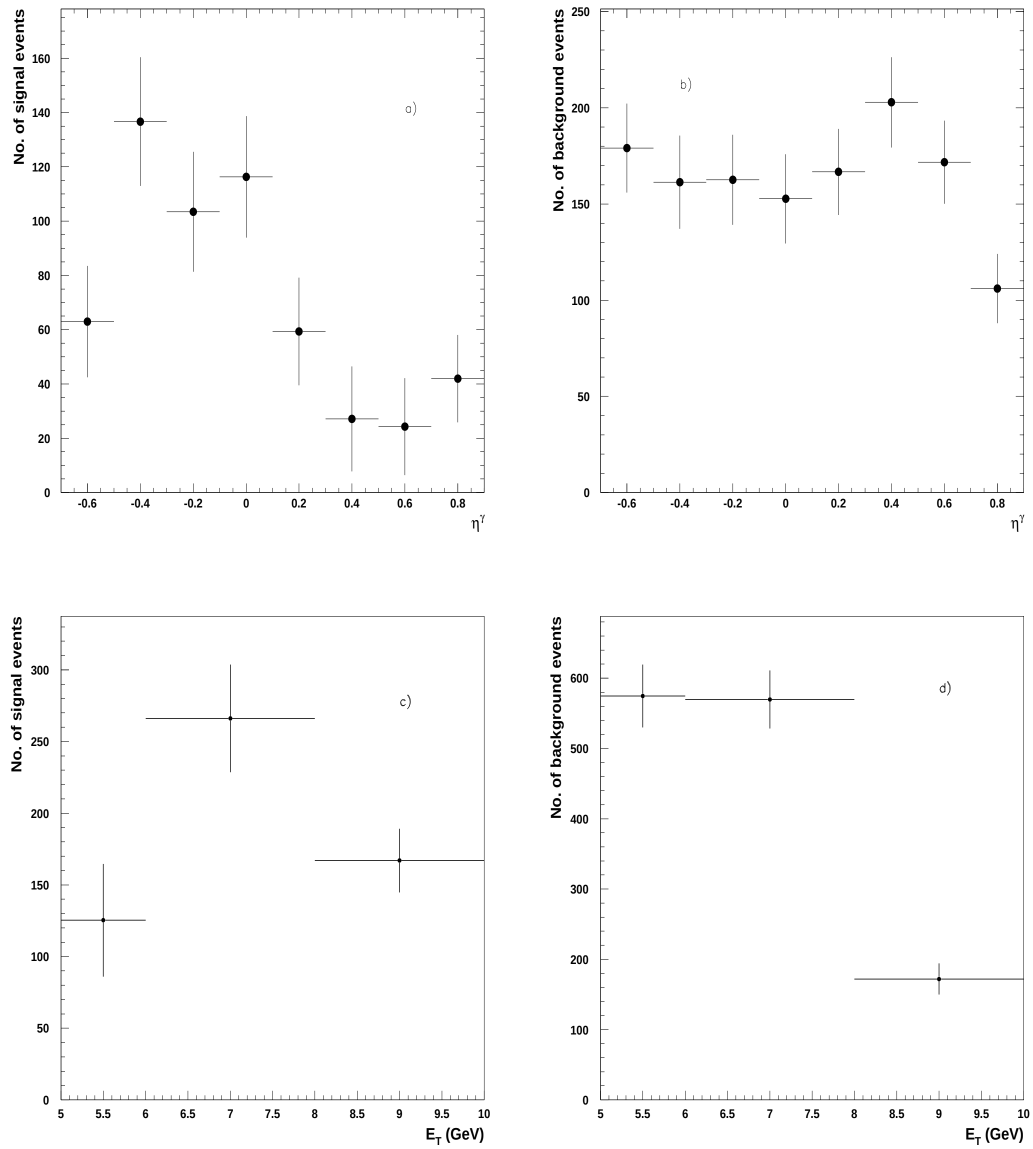

Figure 5.12: *Extracted signal and background plots for the inclusive prompt photon process. a) η^{γ} signal, b) η^{γ} background, c) E_T^{γ} signal and d) E_T^{γ} background. The plots show the number of events in each region.*

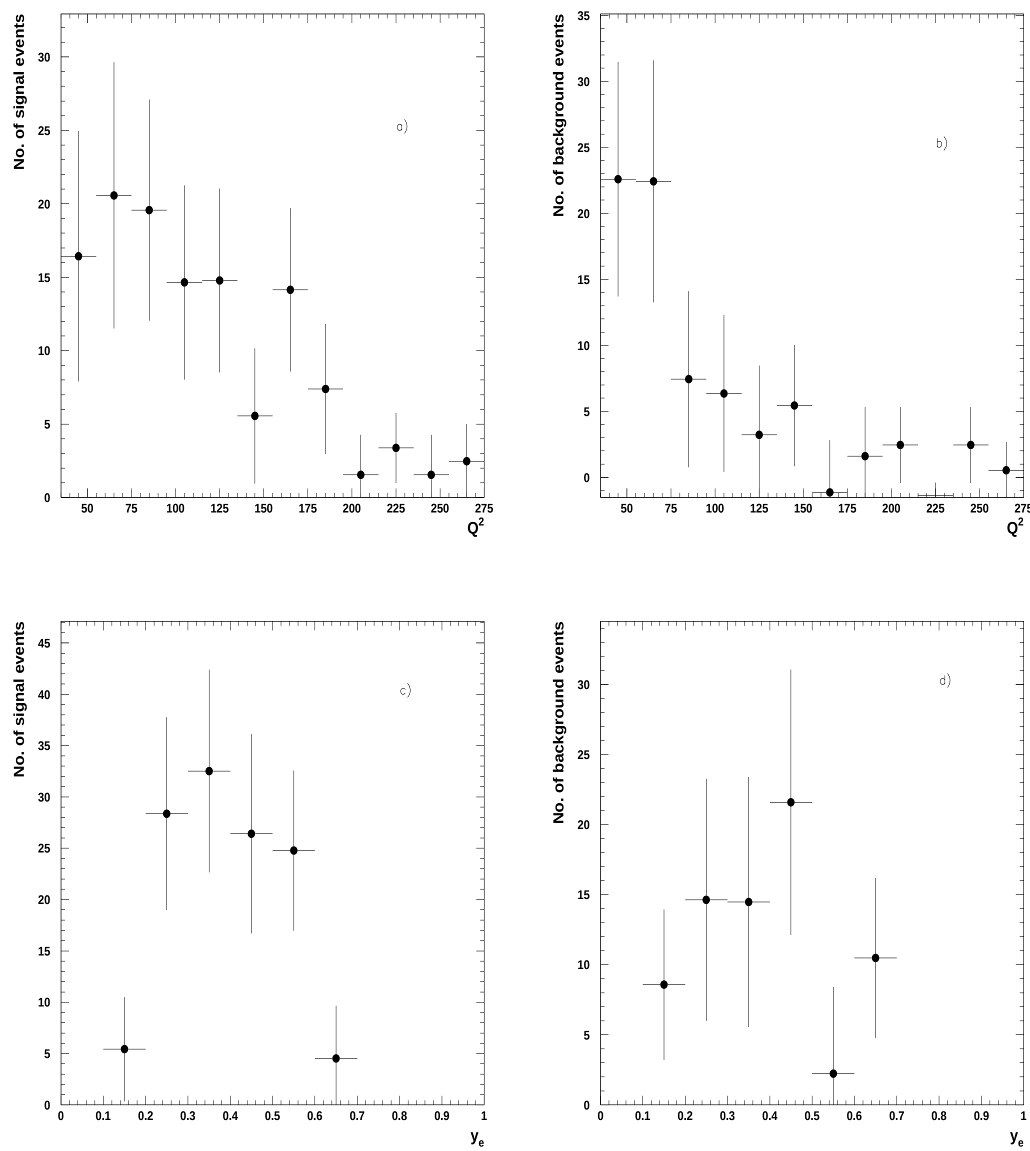

Figure 5.13: *Extracted signal and background plots for the* $(\gamma + jet)$ *process. a)* Q^2 *signal, b)* Q^2 *background, c)* $y_{electron}$ *signal and d)* $y_{electron}$ *background. The plots show the number of events in each region.*

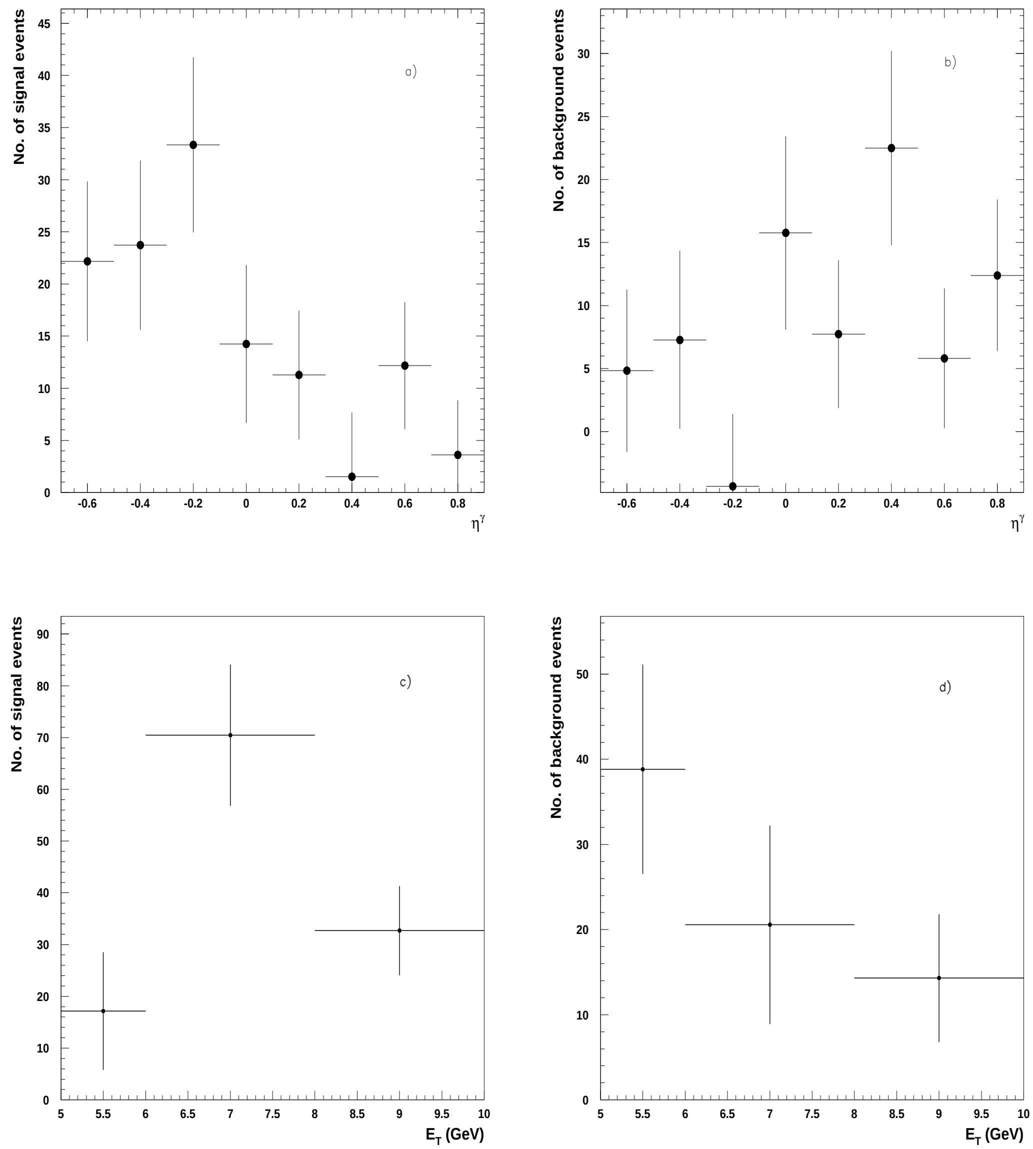

Figure 5.14: *Extracted signal and background plots for the* $(\gamma + jet)$ *process. a)* η^γ *signal, b)* η^γ *background, c)* E_T^γ *signal and d)* E_T^γ *background. The plots show the number of events in each region.*

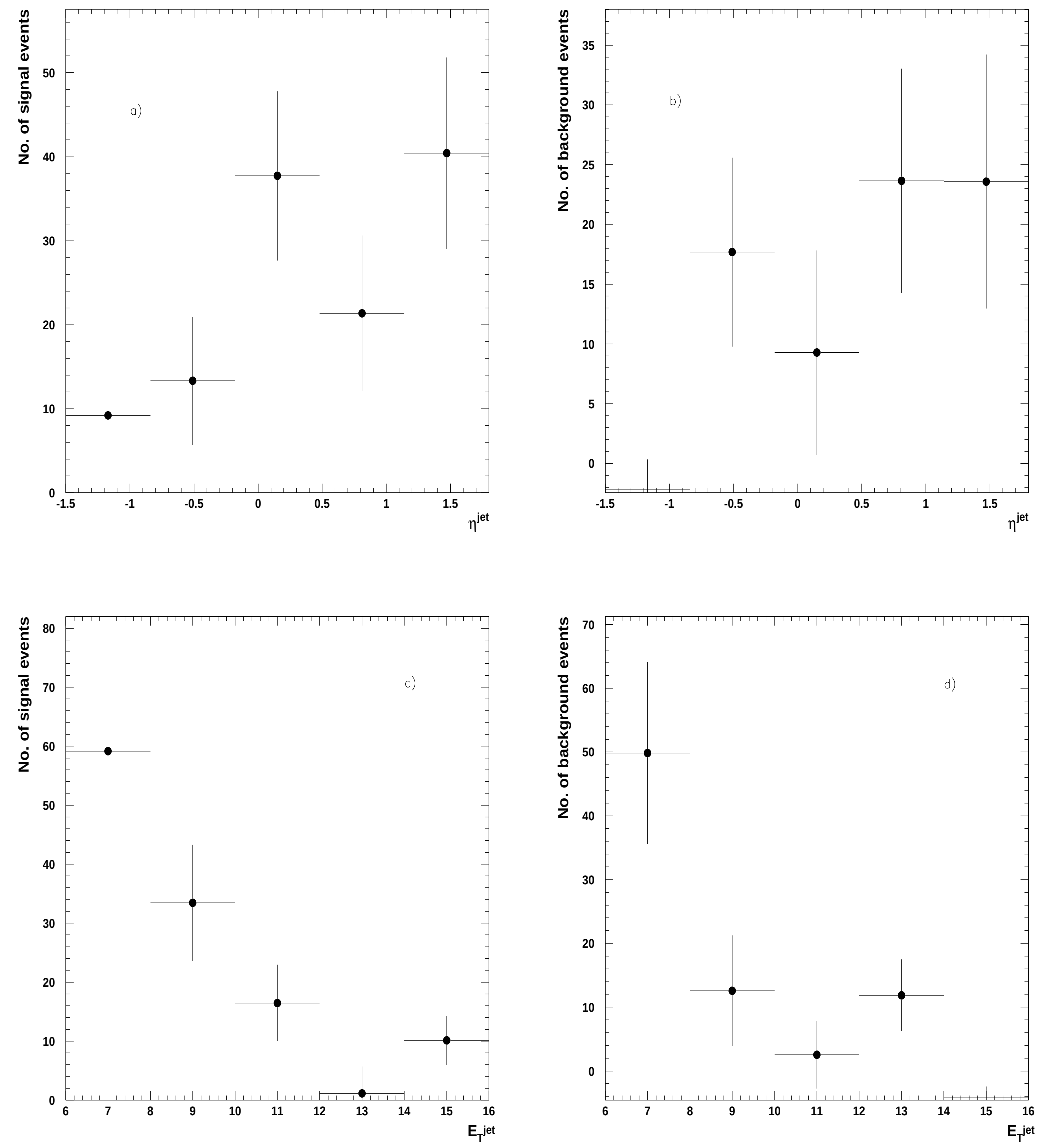

Figure 5.15: *Extracted signal and background plots for the* $(\gamma + jet)$ *process. a)* η^{jet} *signal, b)* η^{jet} *background, c)* E_T^{jet} *signal and d)* E_T^{jet} *background. The plots show the number of events in each region.*

Chapter 6

Inclusive Prompt Photon Production

This chapter contains cross section measurements of what has previously been introduced as the inclusive prompt photon process, where the final state consists of an electron, a prompt photon and some other activity in the calorimeter[1].

Due to differences between hadron and detector level events, the detector level data measurements have to be corrected to obtain the true measurement. The differences arise from energy losses in detector material, detector smearing and bin migrations between the interaction point and where the particle is found in the detector. The correction from a measurement back to its 'true' value is studied by looking at Monte Carlo before and after detector simulation is applied.

[1]No distinction is made between e^+p and e^-p. The result is a weighted average of 33% 820 GeV and 67% 920 GeV c.m. energy. The predicted cross section changes by far less than the statistical precision of the measurement.

6.1 Hadron Level Cross Sections of Inclusive Prompt Photons

For the inclusive prompt photon data which satisfies the kinematic cuts listed in Equations (6.1) to (6.5) and the energy isolation cone requirement, the cross section is calculated using an acceptance from PYTHIA studies.

$$Q^2 > 35GeV^2 \tag{6.1}$$

$$2.44 < \theta_{electron} < 3.0 \tag{6.2}$$

$$y_{JB} > 0.04; y_{electron} < 0.7 \tag{6.3}$$

$$5 < E_T^{\gamma} < 10\text{GeV} \tag{6.4}$$

$$-0.7 < \eta^{\gamma} < 0.9 \tag{6.5}$$

The data are corrected for energy losses and migration of events between bins from generation to detection by applying a bin-by-bin method of correction. In order to do this it is necessary to define the efficiency, ϵ and purity, p, of a Monte Carlo sample. The efficiency of a particular bin i, $\epsilon(i)$, is defined in Equation (6.6).

$$\epsilon(i) = \frac{B(i)}{G(i)} \tag{6.6}$$

In Equation (6.6), $G(i)$ is the number of events originally generated in bin i, and $B(i)$ is the number of events which are both generated *and* reconstructed in bin i. The efficiency of a sample of Monte Carlo events provides a measure of how many of the originally generated events are reconstructed in the same region.

The purity of a particular bin in a Monte Carlo sample of events, $p(i)$, is defined in Equation (6.7).

$$p(i) = \frac{B(i)}{R(i)} \tag{6.7}$$

In Equation (6.7), $R(i)$ is the number of events which are reconstructed in a bin. As before, $B(i)$ is the number of events which are both generated and reconstructed in that bin. The purity provides a measure of the number of detected events which have not migrated bins between hadron and detector level.

The errors on the purity and efficiency are calculated using binomial expressions, in Equations (6.8) and (6.9), which do not allow them to exceed a value of one.

$$\delta\epsilon(i) = \sqrt{\frac{(1-\epsilon(i)).\epsilon(i)}{G(i)}} \tag{6.8}$$

$$\delta p(i) = \sqrt{\frac{(1-p(i)).p(i)}{R(i)}} \tag{6.9}$$

The measured efficiencies and purities of the photon transverse energy and pseudorapidity from PYTHIA are shown in Figure (6.1). As in the background subtraction, the E_T plot is binned in unequal bins, with bin sizes of $5 \rightarrow 6$ GeV, $6 \rightarrow 8$ GeV and $8 \rightarrow 10$ GeV.

6.1.1 Acceptance Correction

A correction factor related to the efficiency and purity to account for the effect of inter-bin migration can be calculated and applied to produce a corrected cross section. This acceptance correction factor, $A(i)$, is defined in Equation (6.10).

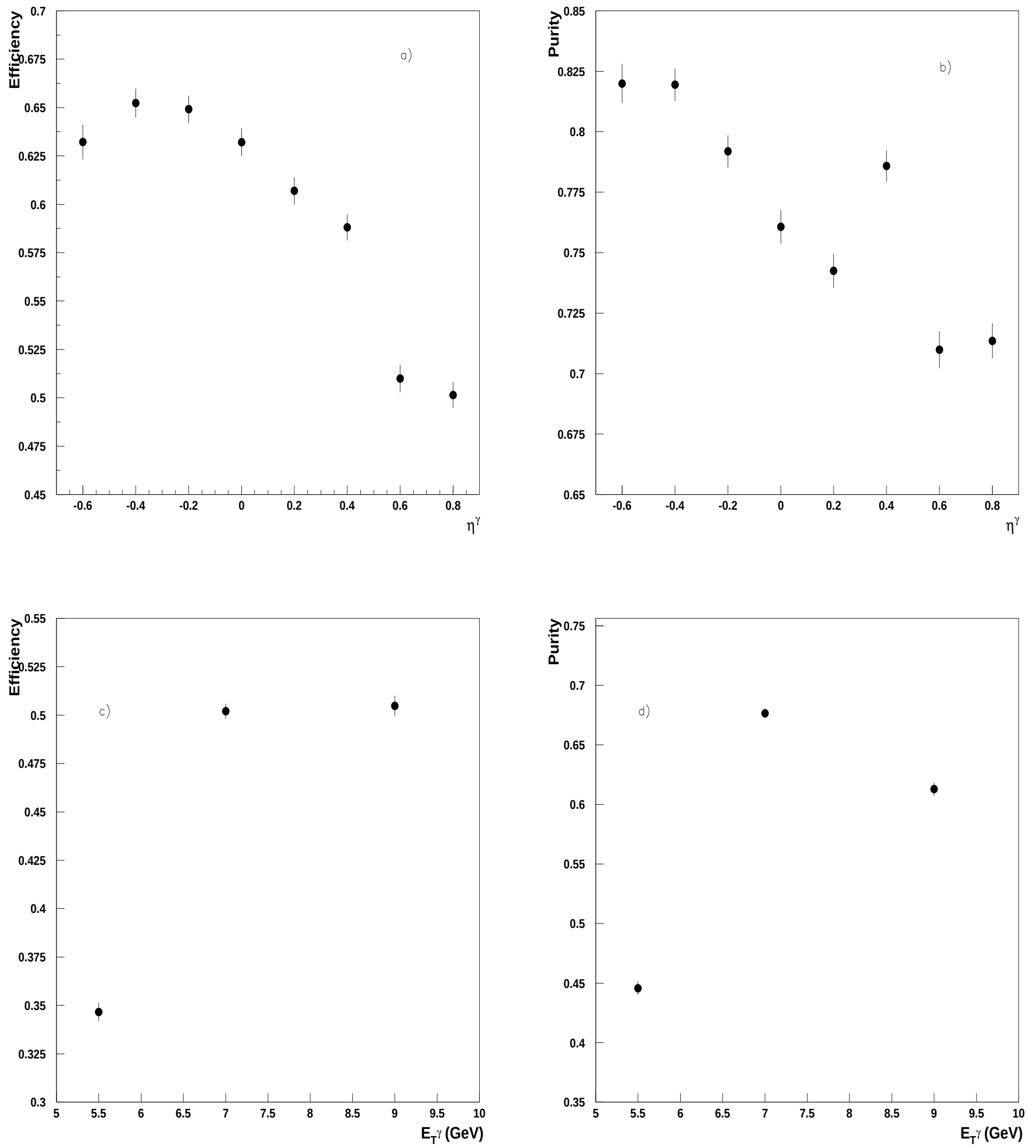

Figure 6.1: *The efficiencies and purities as calculated using PYTHIA v6.206. a) η^γ Efficiency b) η^γ Purity c) E_T^γ Efficiency d) E_T^γ Purity*

$$A(i) = \frac{p(i)}{\epsilon(i)} \tag{6.10}$$

The errors on the acceptance correcion factors take into account correlations between $G(i)$ and $R(i)$ and are given by Equation (6.11).

$$\delta A(i) = \sqrt{\frac{G(i)}{R(i)_3}\left[G(i) + R(i) - 2G(i) \cap R(i)\right]} \tag{6.11}$$

The acceptance correction factors for η^γ and E_T^γ are shown in Figure (6.2).

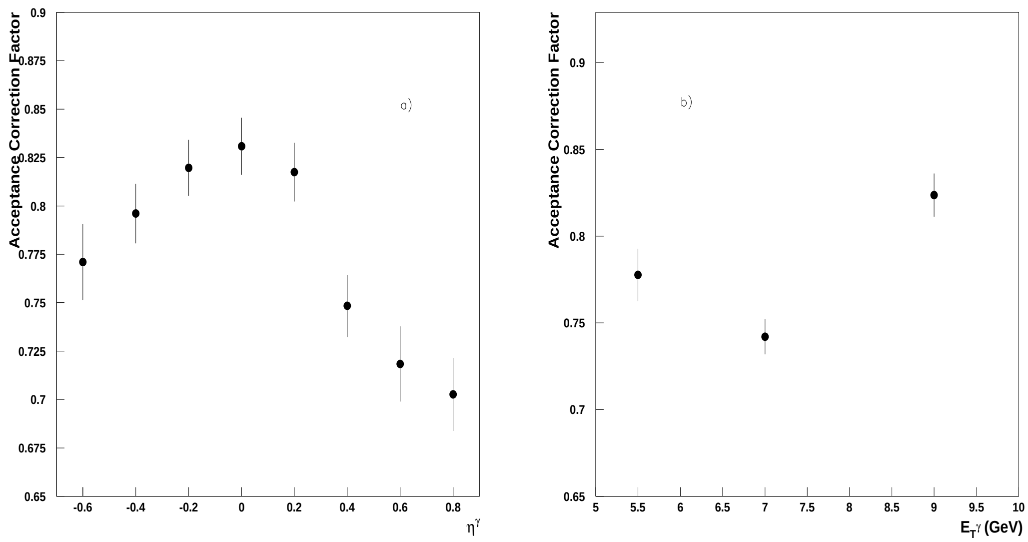

Figure 6.2: *Acceptance Correction Factors for a) η^γ and b) E_T^γ as calculated from PYTHIA v6.206.*

6.2 Inclusive Cross Sections

The differential cross-section for a bin i of a process with respect to a particular physics quantity is given by Equation (6.12).

$$\frac{d\sigma}{d\eta^{\gamma}}_i = \frac{N(\eta^{\gamma})}{A(\eta^{\gamma}).\Gamma(\eta^{\gamma}).\int Ldt} \tag{6.12}$$

In Equation (6.12), $N(\eta^{\gamma})$ is the number of events in the bin, $A(\eta^{\gamma})$ is the acceptance correction factor for the bin, as calculated from Monte Carlo models, $\Gamma(\eta^{\gamma})$ is the width of the bin and $\int Ldt$ is the total luminosity of the sample of data under consideration.

Differential cross sections with respect to the pseudorapidity and transverse energy of the prompt photon in the process $e+p \rightarrow e+\gamma+X$ are shown in Figure (6.3). The errors here are statistical errors which have been propagated through the background subtraction procedure.

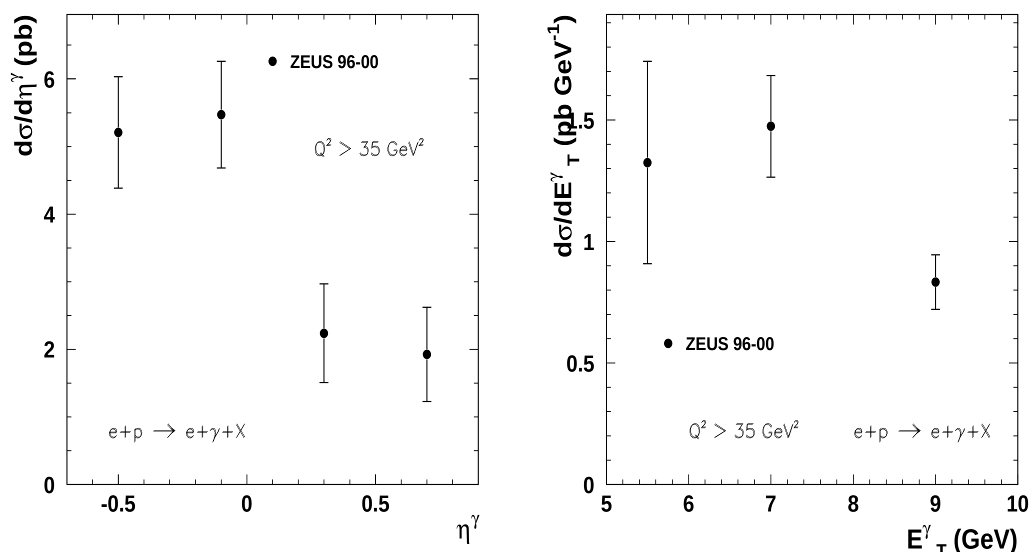

Figure 6.3: *Differential Cross Sections for Inclusive Prompt Photon Production for a)* $d\sigma/d\eta^{\gamma}$ *and b)* $d\sigma/dE_T^{\gamma}$. Statistical errors only are shown.

It is observed that the rapidity distribution falls as the pseudorapidity increases giving an enhancement of prompt photons at negative pseudorapidity, in the backwards region of the ZEUS calorimeter. It is also observd that the E_T

slope is gently falling as the transverse energy increases.

6.3 Systematic Errors

In order to provide a better estimate of the accuracy of the final measurement it is necessary to study a range of possible sources of systematic uncertainty, concentrating on suspected larger effects like energy measurement, background subtraction or Monte Carlo acceptance.

* Calorimeter energy scale. It is probable that there is some offset from the true value in the energies measured in the calorimeter. The potential effect of this is studied by varying the reconstructed energy distributions in the Monte Carlo by +/- 3 % and calculating two new sets of acceptances.

* Photon Energy Resolution. The photon energy at detector level is varied within +/- 10% in both data and reconstructed Monte Carlo. This reflects the width of the energy resolution spectrum. This is to study possible calibration errors in the data. Ideally cross sections should not change as acceptances will alter to compensate changes in data.

* Photon f_{max} correction. Based on the intensive background subtraction studies performed for the photoproduction analysis the photon f_{max} distribution is corrected so the peaks in data and single photons are more closely aligned. The scale factor is varied within the errors.

* Pion f_{max} correction. The pion f_{max} distribution is also corrected based on the photoproduction analysis and varied within the errors.

* HERWIG. The acceptance correction factors are calculated using HERWIG rather than PYTHIA.

* slope of E_T reweighting. The single particle Monte Carlo is generated at flat E_T and then reweighted by a factor e^{-aE_T} based on the E_T distribution of data. The reweighting factor, a, is altered by $\pm 3\%$.

The systematic errors are shown individually for each bin of each distribution. They are displayed by showing the size of the systematic change from the original data point as a percentage of the statistical error bar in the bin. The errors for the photon pseudorapidity are shown in Figure (6.4).

In Figure (6.4), the eight plots represent the eight bins of η^γ used in the analysis. These bins are defined previously. It is seen in Figure (6.4) that the largest effects are from altering the photon energy and varying the correction to the pion f_{max} shape, but no obvious pattern can be established.

The systematic errors for the photon transverse energy plot are shown in Figure (6.5). This shows the systematic uncertainties in the three previously established bins of photon transverse energy. As with the case of photon pseudorapidity it is found that varying the photon energy of the f_{max} correction factors have the largest effect but no clear systematic pattern emerges.

6.4 Cross Sections with Systematic Errors

These systematic errors are added in quadrature to the statistical errors. The calorimeter energy scale uncertainty is assumed to be correlated to all the other systematic uncertainties and is therefore not added in quadrature, but is instead shown as a yellow band around the data points. The differential cross sections are shown together with these additions in Figure (6.6). The plot of η^γ is now shown in four bins in view of the large size of the errors.

It is observed from Figure (6.6) that the systematic uncertainties are typically small in comparison to the size of the statistical error bars. It is also seen that altering the calorimeter energy scale by $\pm 3\%$ is a small effect with the limited

η^γ	$d\sigma/d\eta^\gamma$ (pb)
$-0.7 < \eta^\gamma < -0.5$	$3.36 \pm 1.10^{+0.54}_{-0.46}$
$-0.5 < \eta^\gamma < -0.3$	$7.06 \pm 1.23^{+0.51}_{-0.80}$
$-0.3 < \eta^\gamma < -0.1$	$5.19 \pm 1.11^{+0.24}_{-0.35}$
$-0.1 < \eta^\gamma < 0.1$	$5.76 \pm 1.11^{+0.20}_{-0.37}$
$0.1 < \eta^\gamma < 0.3$	$2.98 \pm 1.00^{+0.22}_{-0.33}$
$0.3 < \eta^\gamma < 0.5$	$1.49 \pm 1.06^{+0.28}_{-0.34}$
$0.5 < \eta^\gamma < 0.7$	$1.39 \pm 1.02^{+0.26}_{-0.41}$
$0.7 < \eta^\gamma < 0.9$	$2.46 \pm 0.94^{+0.18}_{-0.25}$

Table 6.1: *Values of the Inclusive Cross Section as a function of photon pseudorapidity*

$E_T(GeV)$	$d\sigma/dE_T^\gamma(pbGeV^{-1})$
$5.0 < E_T^\gamma < 6.0$	$1.32 \pm 0.42^{+0.05}_{-0.01}$
$6.0 < E_T^\gamma < 8.0$	$1.47 \pm 0.21^{+0.06}_{-0.05}$
$8.0 < E_T^\gamma < 10.0$	$0.83 \pm 0.11^{+0.10}_{-0.01}$

Table 6.2: *Values of the Inclusive Cross Section as a function of photon transverse energy*

statistics. The small size of the energy scale uncertainty allows us to combine this less significant effect with the other systematic uncertainties.

6.4.1 Final Inclusive Cross Sections

The actual values of the cross section in bins of photon pseudorapidity are given in Table (6.1).

Numerical values for the differential inclusive cross section as a function of photon transverse energy are given in Table (6.2).

The total inclusive cross section, defined in Equations (6.1) to (6.5) and including the isolation requirements, calculated from photon pseudorapidity measurements is given in Equation (6.13) and from photon transverse energy measurements in Equation (6.14).

$$\sigma(ep \rightarrow e\gamma X) = (5.94 \pm 0.61(stat.)^{+0.19}_{-0.26}(sys.))pb \tag{6.13}$$

$$\sigma(ep \rightarrow e\gamma X) = (5.94 \pm 0.63(stat.)^{+0.23}_{-0.10}(sys.))pb \tag{6.14}$$

The slight difference in the two measurements arises from the background subtraction procedure.

6.5 Comparison to Monte Carlo

Two Monte Carlo models have been used in calculating the acceptance correction factors and estimating an associated systematic uncertainty, PYTHIA v6.206 and HERWIG v6.1. The final measured inclusive cross sections are compared to both these PYTHIA and HERWIG predictions. Comparisons are made to both absolute Monte Carlo predictions, to compare the magnitude with the data results and to normalised curves to compare the shape of the Monte Carlo distributions more easily to the data.

6.5.1 Absolute Predictions of Monte Carlo Models

Absolute cross section predictions from the Monte Carlo are determined using the luminosity of the generated Monte Carlo events and the number of events which survive the complete selection process at hadron level. Comparisons of the measured data cross sections to these predictions are shown in Figure (6.7).

It is seen from Figure (6.7) that both predictions lie significantly below the level of the data points, with HERWIG lower than PYTHIA. Compared to a total data cross section of $5.94pb^{-1}$ PYTHIA predicts a total cross section value of $2.48pb^{-1}$ and HERWIG predicts a value of $0.71pb^{-1}$. For the pseudorapidity distribution the shape of the HERWIG curve more closely resembles the shape of the data. Further details of Monte Carlo generation can be found in Appendix A, including discussion of Q^2 and y distributions. It is noted, however that generating events with two hard scales (Q^2, E_T) is a challenge for Monte Carlo simulation.

6.5.2 Normalised Predictions of Monte Carlo Models

To better ascertain the success of the models in describing the correct shape of the data distributions, the curves are normalised to be of the same area as the data. Comparisons of the cross sections to these normalised PYTHIA and HERWIG predictions are shown in Figure (6.8).

It is clear from Figure (6.8) that while both models describe the transverse energy distribution of the photon reasonably well, PYTHIA does not describe well the pseudorapidity spectrum. HERWIG describes the shape of this curve much more successfully, with the curve peaking in the rear region and falling towards positive pseudorapidity values.

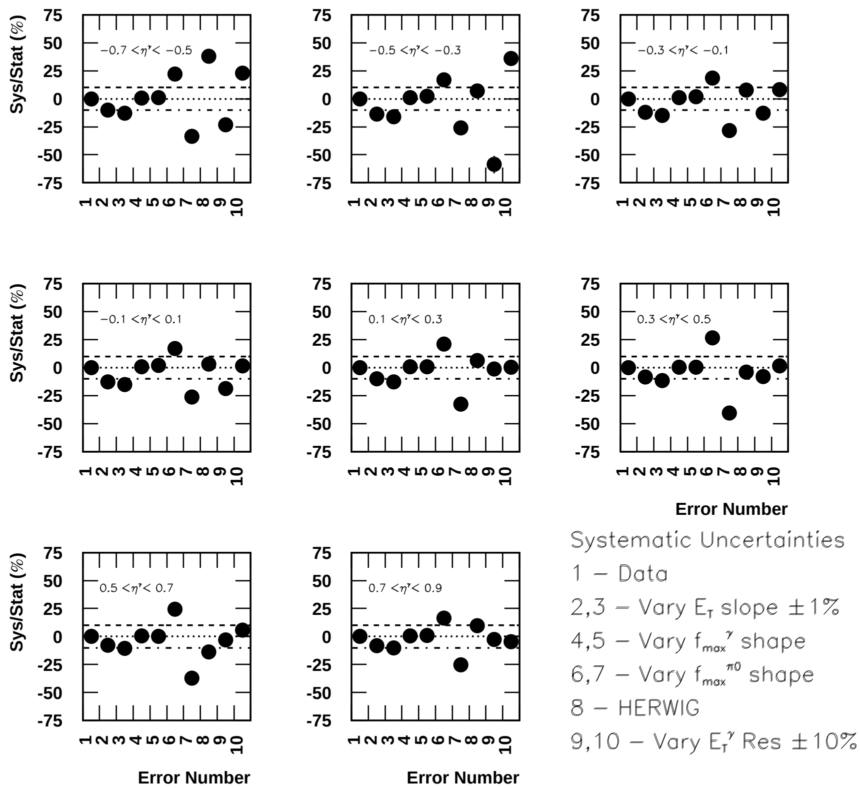

Figure 6.4: *Systematic errors as a percentage of the statistical error size, for η^γ. The original data is represented by a straight line at zero. Each point 2-10 represents a different systematic change. Further lines indicating a change of* $\pm 10\%$ *are shown. The systematic effects are displayed in eight bins of η^γ.*

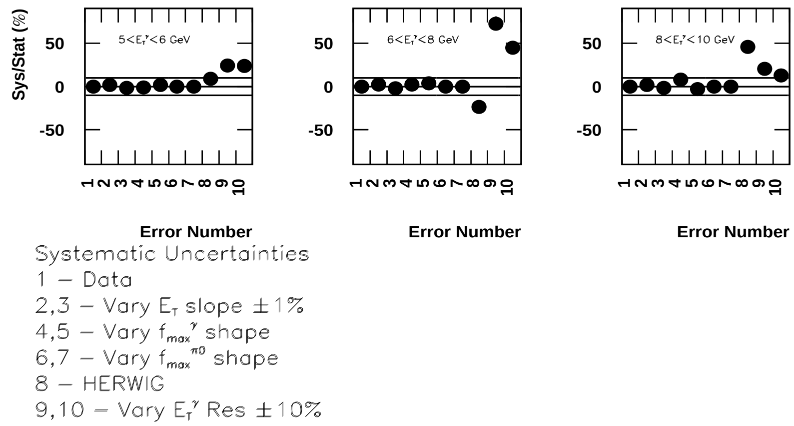

Figure 6.5: *Systematic errors as a fraction of the statistical error size, for E_T^γ. The original data is represented by a straight line at zero. Each point 2-10 represents a different systematic effect. Two further lines are drawn showing ±10%. The effects are shown in three bins of E_T^γ.*

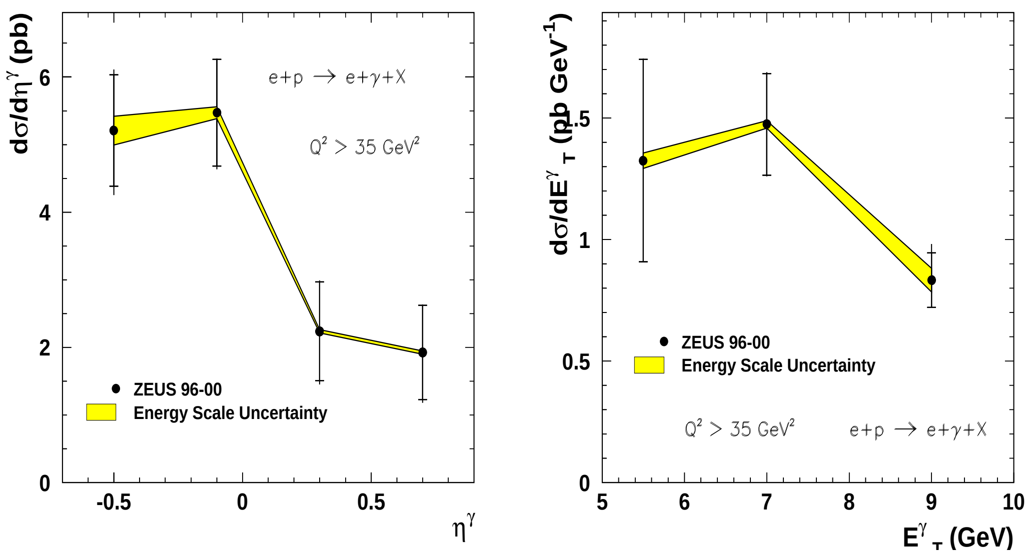

Figure 6.6: *Final inclusive cross sections with systematic errors and calorimeter energy scale uncertainty. a) $d\sigma/d\eta^\gamma$ and b) $d\sigma/dE_T^\gamma$*

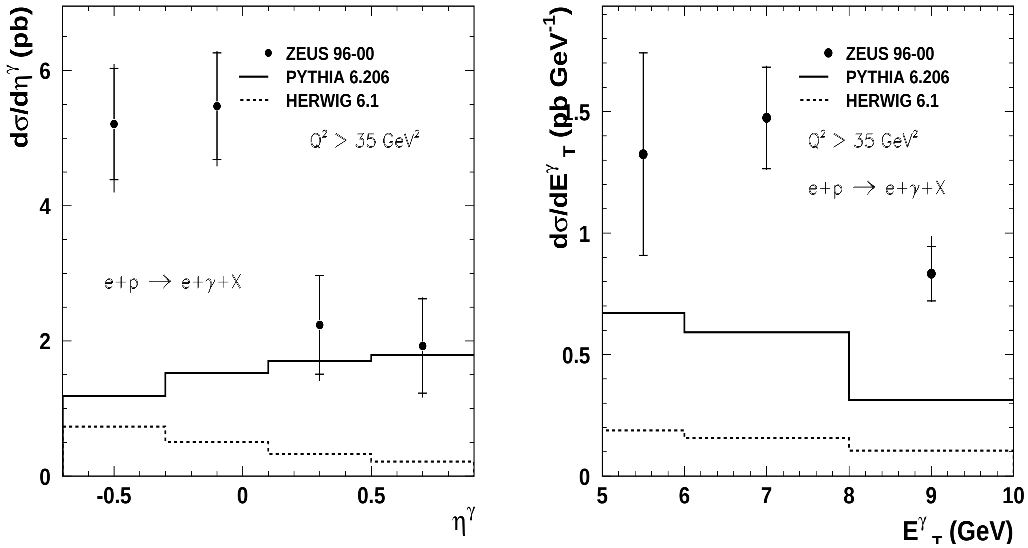

Figure 6.7: *Comparisons to absolute predictions from PYTHIA and HERWIG for a) Photon pseudorapidity and b) Photon Transverse Energy*

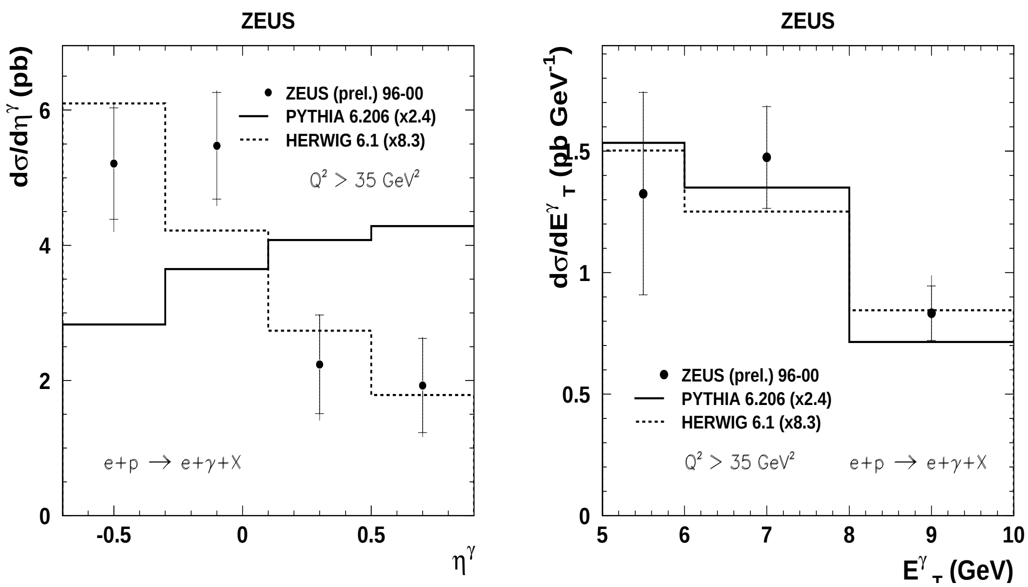

Figure 6.8: *Comparisons to normalised predictions from PYTHIA and HERWIG for a) Photon pseudorapidity and b) Photon Transverse Energy*

Chapter 7

Prompt Photon + Jet Production

As previously described, a subset of the inclusive prompt photon process can be studied where a jet is reconstructed within the acceptance. This is the $(\gamma + jet)$ process. For these events the procedure to obtain the hadron level cross sections is exactly as for the inclusive process, but only events with one, and only one, well defined jet passing the cuts are accepted. The same PYTHIA sample used to correct the inclusive events back to hadron level is used, with jet finding carried out at both hadron and detector level. Including a jet in the process makes the kinematic variables, E_T^{jet} and η^{jet} available for study. A more detailed description of the definition of a jet can be found in Chapter 4. As previously stated, jets are accepted within the ranges listed in Equations (7.1) and (7.2).

$$E_T^{jet} \geq 6GeV \tag{7.1}$$

$$-1.5 < \eta^{jet} < 1.8 \tag{7.2}$$

Measured cross sections for $(\gamma + jet)$ events satisfying Equations (6.1) to (6.5) and (7.1) to (7.2) and the energy isolation cone requirement are compared to predictions from standard Monte Carlo models, PYTHIA 6.206 and HERWIG 6.1. Comparisons to both absolute and normalised predictions are made. The process $ep \rightarrow e\gamma jet$ has been calculated at order $O(\alpha^2\alpha_s)$ by theorists [12] so the final cross section measurements are compared to the theoretical predictions.

7.1 Correction to Hadron Level Cross Sections

In order to show the cross sections at hadron level, Monte Carlo acceptance corrections are applied, as for the inclusive process.

7.1.1 Efficiency and Purity

The acceptance correction factor used is formed, as before, from the efficiency and purity of a Monte Carlo sample. The efficiency and purity are described in more detail in Chapter 6 and are defined in Equations (6.6) and (6.7).

The efficiencies and purities for the photon related quantities, η^γ and E_T^γ are shown in Figure (7.1). It is interesting to note the slight dip in acceptance in the central rapidity region. This is the region where the photon is in the centre of the barrel calorimeter, which therefore leaves less space in the area for a jet to be found as a result of the strict isolation criteria. The photon isolation does not permit the jet to be located near it. This influences the calculation of the acceptances in a way which depends on the production dynamics at different pseudorapidities. The photon-jet rapidity correlation differs between PYTHIA and HERWIG, however this is taken into account in the systematic uncertainty measurements. The efficiency and purity distributions of PYTHIA for the jet variables, η^{jet} and E_T^{jet} are given in Figure (7.2). It can be seen that efficiency and purity values are missing for the lowest jet pseudorapidity bin. This bin has very low statistics in both data and Monte Carlo, and in the case of Monte Carlo there are no events both generated and reconstructed in the same bin.

However, as there are some events in the bin at both generator and detector level an acceptance correction factor is still calculable.

7.1.2 Acceptance Correction

The acceptance correction factor is calculated from the measured efficiency and purity using the relationship in Equation (6.10). The acceptance correction factors for the four physics variables under investigation for the $(\gamma + jet)$ process are shown in Figure (7.3).

The acceptance correction factors for the photon variables are similar in shape to those for the inclusive process. The acceptance of events falls as the jet energy increases and rises as the jet pseudorapidity increases.

7.2 Systematic Uncertainty

It is not sufficient to quote a measurement with only a statistical error. It is also necessary to consider any potential systematic effects which may be influencing the final result and allow for these. The systematic uncertainties studied are the same as for the inclusive case. Here, the effect of varying the jet energy by $\pm 20\%$ is also added. This is done in an analagous way to the photon energy variation.

First, the systematic errors for the photon pseudorapidity distribution are shown, in Figure (7.4). These are shown in 8 bins of pseudorapidity, before the final cross section is shown in four bins due to limited statistics.

It is seen that the most significant effects on this cross section are the change between PYTHIA and HERWIG, the adjustment of the f_{max} correction factor and the changing of the photon and jet energies.

Figure (7.5) shows the systematic uncertainties for the photon transverse energy distribution in three energy bins. Looking at Figure (7.5) the same major effects on the overall cross section that were observed for the pseudorapidity distribution are seen here. Systematic uncertainties for the jet pseudorapidity dis-

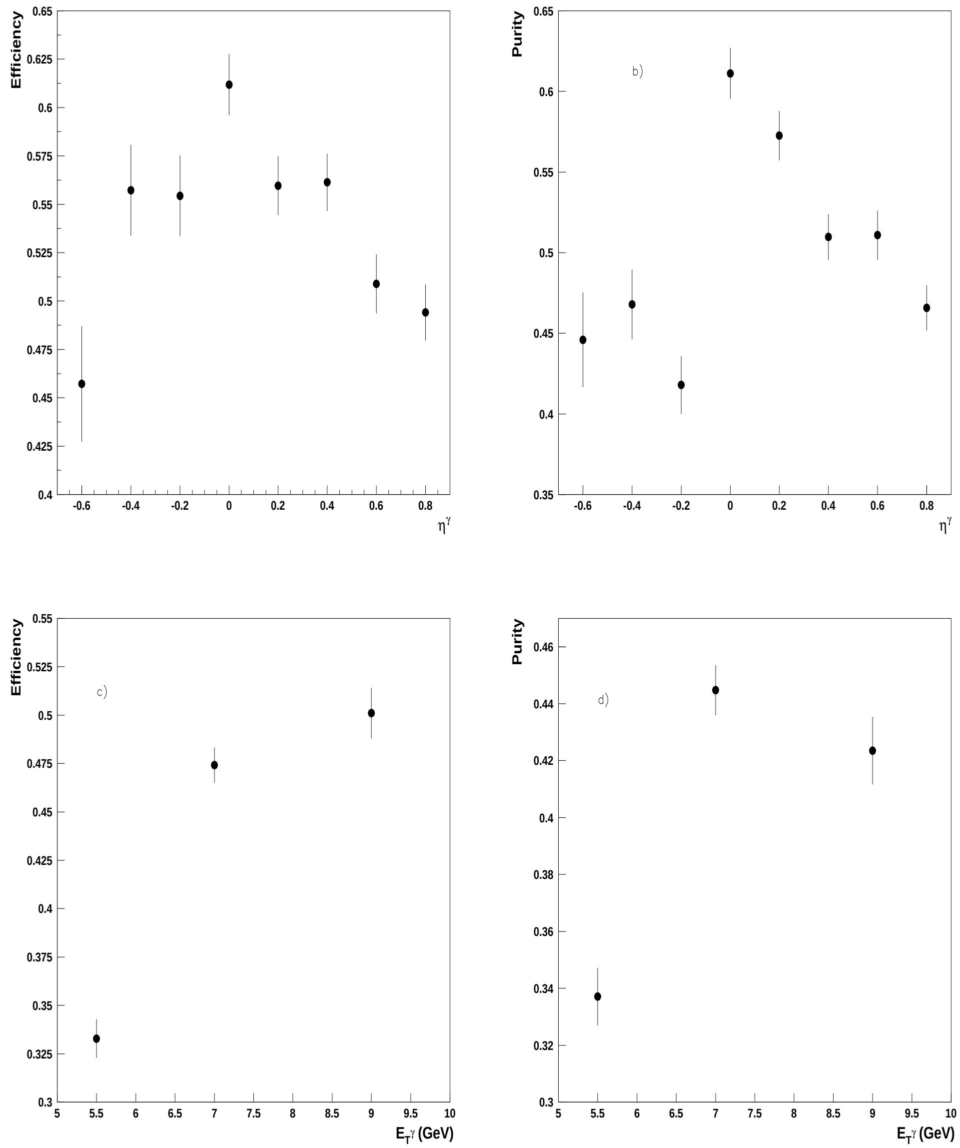

Figure 7.1: *Efficiencies and Purities for PYTHIA 6.206 a) η^{γ} Efficiency b) η^{γ} Purity c) E_T^{γ} Efficiency d) E_T^{γ} Purity.*

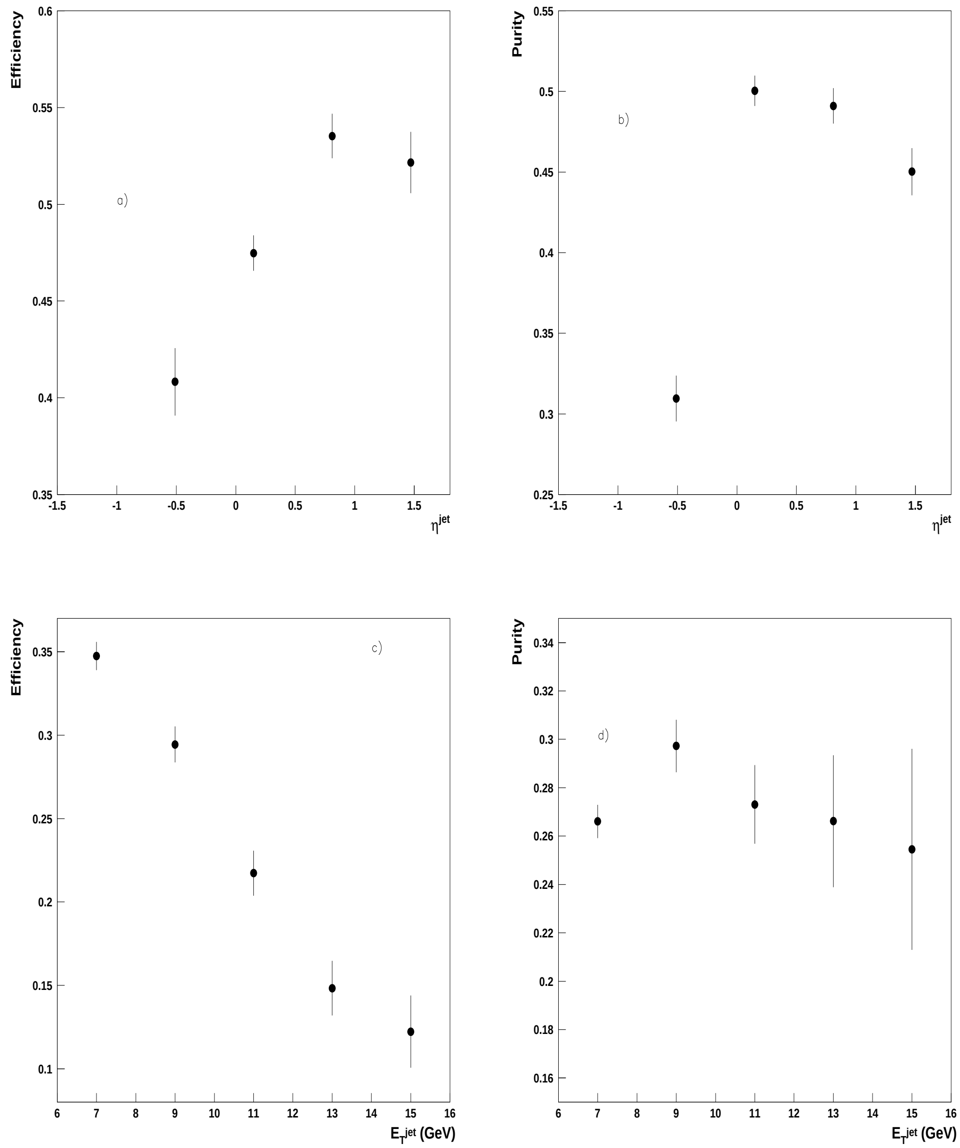

Figure 7.2: *Efficiencies and Purities for PYTHIA 6.206 a) η^{jet} Efficiency b) η^{jet} Purity c) E_T^{jet} Efficiency d) E_T^{jet} Purity.*

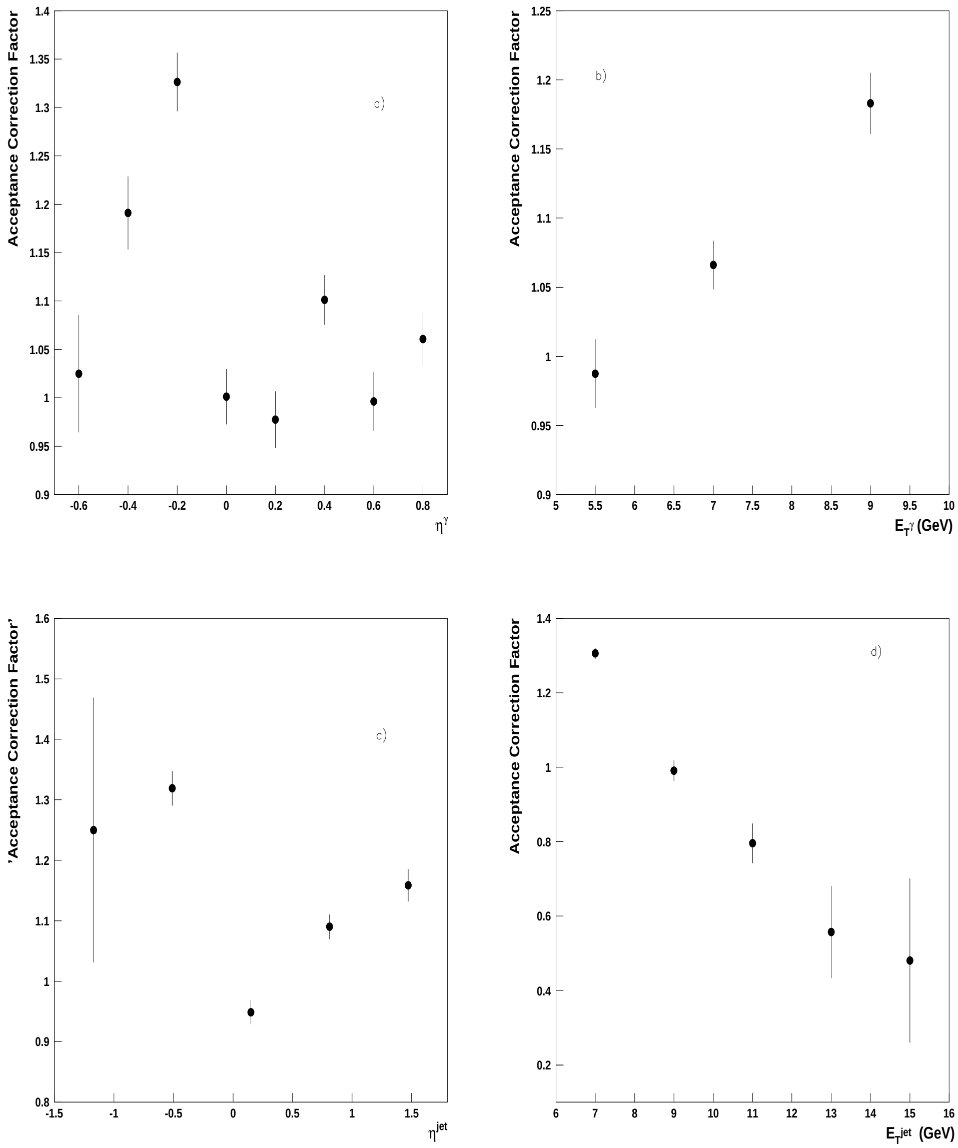

Figure 7.3: *Acceptance Correction Factors from PYTHIA 6,206 for a) η^{γ} b) E_T^{γ} c) η^{jet} and d) E_T^{jet}.*

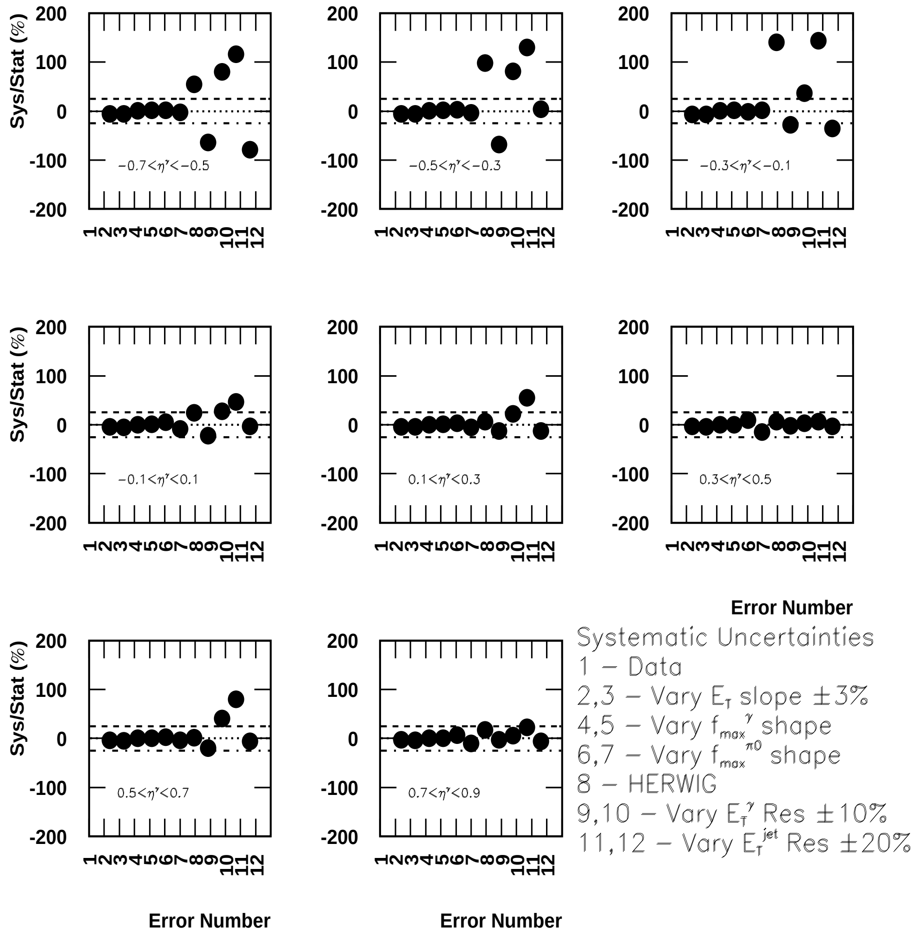

Figure 7.4: *Systematic errors in bins of photon pseudorapidity. The ratio of the systematic error size to statistical error size is shown for each separate systematic effect studied for each of the eight bins of* η^γ*. The original data is represented by a straight line, with two further lines shown at* $\pm 25\%$*. The 11 points represent the systematic effects 2 to 12.*

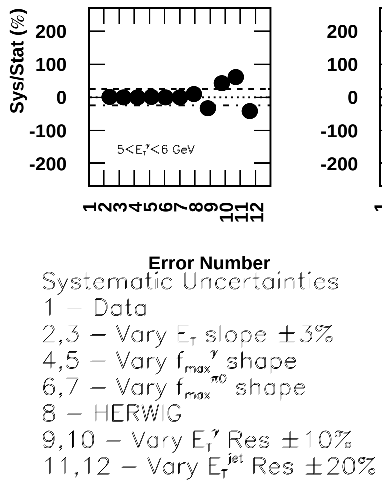

Figure 7.5: *Systematic errors in bins of photon transverse energy. The ratio of the systematic error size to statistical error size is shown for each separate systematic effect studied for each of the three bins of E_T^γ. The original data is represented by a line at zero with two further lines at ±25%. The 11 points represent the systematic effects, 2 to 12.*

tribution are shown in Figure (7.6). These are shown in five equal pseudorapidity bins, again showing the same general response to the changes made.

Similarly, the systematic uncertainties relating to the transverse energy of the jet are shown in Figure (7.7), again in five bins, although the uppermost two bins are combined due to limited statistics before the final cross section is presented.

7.3 $(\gamma + jet)$ Cross Sections

7.3.1 Photon Pseudorapidity

The photon pseudorapidity is measured for photons in the region $-0.7 < \eta^\gamma < 0.9$ with transverse energies between 5 and 10 GeV. The differential cross section for

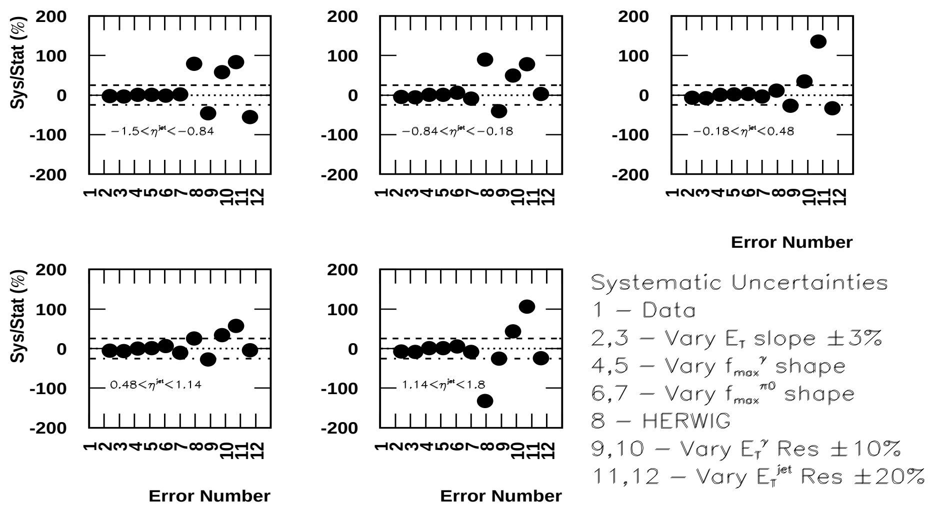

Figure 7.6: *Systematic errors in bins of jet pseudorapidity. The ratio of the systematic error size to statistical error size is shown for each separate systematic effect studied for each of the five bins of* η^{jet}*. The original data is represented by a line at zero with two further lines at* $\pm 25\%$*. The 11 points represent the systematic effects, 2 to 12.*

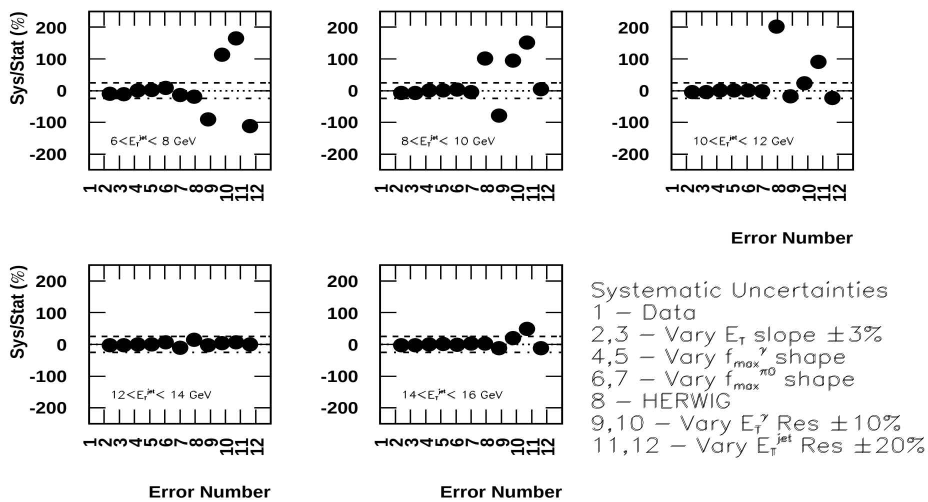

Figure 7.7: *Systematic errors in bins of jet transverse energy. The ratio of the systematic error size to statistical error size is shown for each separate systematic effect studied for each of the five bins of E_T^{jet}. The original data is represented by a line at zero with two further lines at ±25%. The 11 points represent the systematic effects, 2 to 12.*

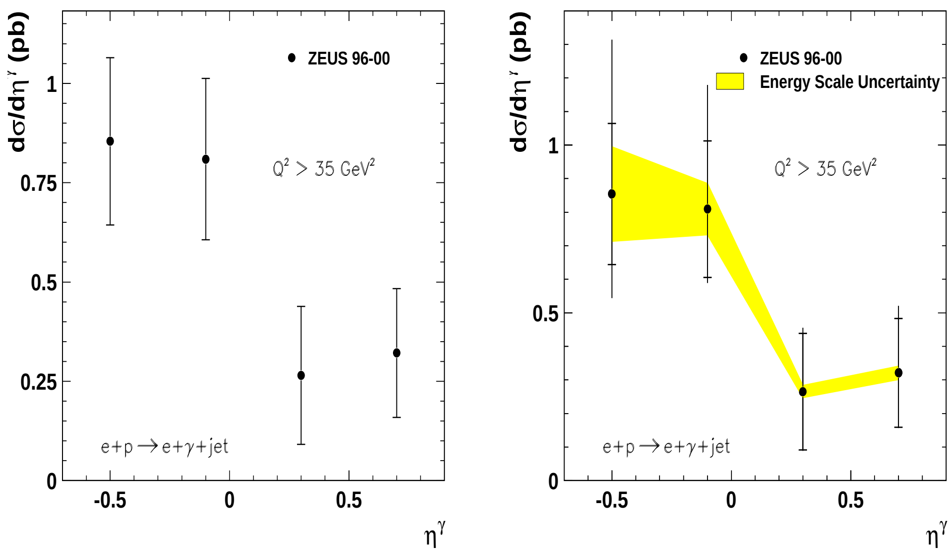

Figure 7.8: *Differential Cross Section, $d\sigma/d\eta^{\gamma}$ for the prompt ($\gamma + jet$) process with a) Statistical Errors only and b) Including systematic uncertainties and the effect of calorimeter energy scale variation.*

production of prompt photon + jet events, $d\sigma/d\eta^{\gamma}$, is shown in Figure (7.8), with only statistical errors and also with systematic uncertainties. The systematic uncertainties are shown added in quadrature to the statistical errors. Because of limited statistics in this process, four bins of photon pseudorapidity are used to display the final results.

Immediately, it is observed in Figure (7.8) that a similar distribution shape to the corresponding measurement from the inclusive process is seen in the photon pseudorapidity spectrum, with a decrease in the number of photons found in moving towards the forward region. Also in Figure (7.8) it is seen that there is no obvious pattern which can be found in the effect of the systematic errors. As with all ZEUS results, the effect of varying the energy measured in the calorimeter is strongly correlated to other systematic effects investigated and is shown separately as a yellow band around the data. It is clear that the energy scale

η^γ	$d\sigma/d\eta^\gamma(pb)$
$-0.7 < \eta^\gamma < -0.3$	$0.85 \pm 0.21^{+0.41}_{-0.28}$
$-0.3 < \eta^\gamma < 0.1$	$0.81 \pm 0.20^{+0.35}_{-0.22}$
$0.1 < \eta^\gamma < 0.5$	$0.26 \pm 0.17^{+0.19}_{-0.18}$
$0.5 < \eta^\gamma < 0.9$	$0.32 \pm 0.16^{+0.20}_{-0.16}$

Table 7.1: *Differential cross section for production of prompt photons accompanied by one jet, in bins of photon pseudorapidity.*

effect is small, with the entire band lying well within the statistical error bars. The measured total cross section for production of prompt photons accompanied by one and only one jet is calculated from this differential cross section to be:

$$\sigma(ep \rightarrow e\gamma jet) = (0.90 \pm 0.15(stat.)^{+0.19}_{-0.08}(sys.))pb \tag{7.3}$$

Numerical values for the differential prompt $(\gamma + jet)$ cross section in photon pseudorapidity bins are given in Table (7.1).

7.3.2 Photon Transverse Energy

The transverse energy of the photon is measured for photons in the energy range, $5 < E_T^\gamma < 10GeV$ and in the defined pseudorapidity range. The differential cross section, $d\sigma/d\eta^\gamma$, for the prompt $(\gamma + jet)$ process is shown in Figure (7.9), with statistical errors only and with statistical and systematic errors.

From. Figure (7.9) we see that the photon transverse energy distribution is again of a similar shape to that seen in the inclusive analysis, with a dip in the lowest energy bin, which is not however statistically significant. It is suggested that this feature is largely a result of a significant background subtraction in this bin, and indeed it is seen to an even larger extent if the cross section is allowed to descend to 4 GeV. The upwards systematic error in this bin is larger than any other seen on the plot, although again no clear pattern is seen. The effect of the

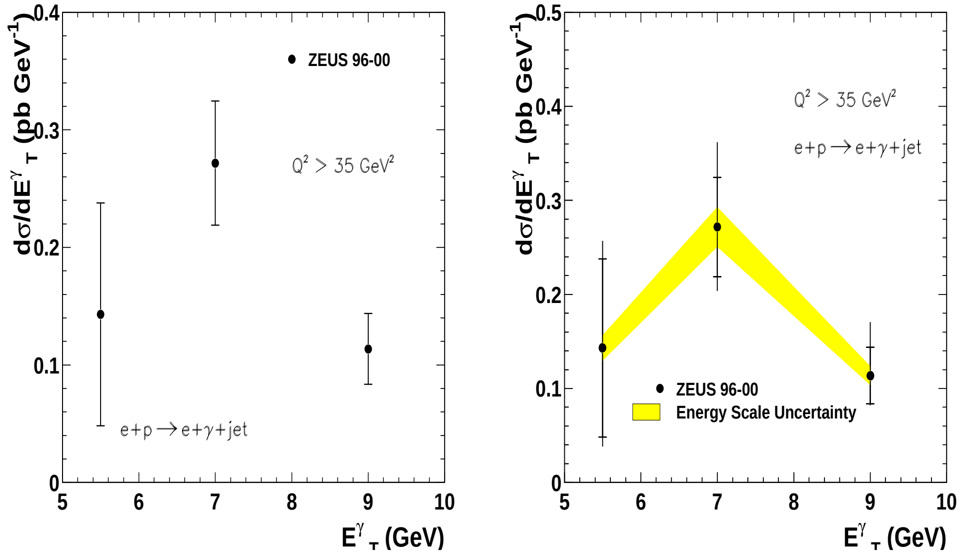

Figure 7.9: *Differential Cross Section, $d\sigma/dE_T^{\gamma}$ for the prompt $(\gamma + jet)$ process with a) Statistical Errors only and b) Including systematic uncertainties and the effect of calorimeter energy scale variation.*

$E_T^\gamma(GeV)$	$d\sigma/dE_T^\gamma(pbGeV^{-1})$
$5.0 < E_T^\gamma < 6.0$	$0.143 \pm 0.095^{+0.063}_{-0.045}$
$6.0 < E_T^\gamma < 8.0$	$0.272 \pm 0.053^{+0.073}_{-0.043}$
$8.0 < E_T^\gamma < 10.0$	$0.113 \pm 0.030^{+0.048}_{-0.001}$

Table 7.2: *Differential cross section for production of prompt photons accompanied by one jet, in bins of photon transverse energy.*

calorimeter energy scale is again small and lies completely within the statistical errors. A general decrease from low to high transverse energies can be seen, as would be expected.

The measured total cross section for production of prompt photons accompanied by one and only one jet is calculated from this differential cross section to be:

$$\sigma(ep \rightarrow e\gamma jet) = (0.91 \pm 0.15(stat.)^{+0.19}_{-0.10}(sys.))pb \qquad (7.4)$$

Numerical values for this differential cross section in bins of the photon transverse energy are given in Table (7.2).

7.3.3 Jet Pseudorapidity

For the $(\gamma + jet)$ process, the variables describing the jet kinematics are available for study alongside those of the photon. It is interesting to look at the same quantities for the jet, the pseudorapidity and the transverse energy. The cross section is measured for jets in the pseudorapidity region $-1.5 < \eta^{jet} < 1.8$ with transverse energy greater than 6 GeV. The measured differential cross section, $d\sigma/d\eta^{jet}$, with statistical errors and with systematic errors and calorimeter energy scale variation are shown in Figure (7.10).

From Figure (7.10) it is observed that the jet pseudorapidity distribution has a rather ragged shape, although with large errors in some bins, but there

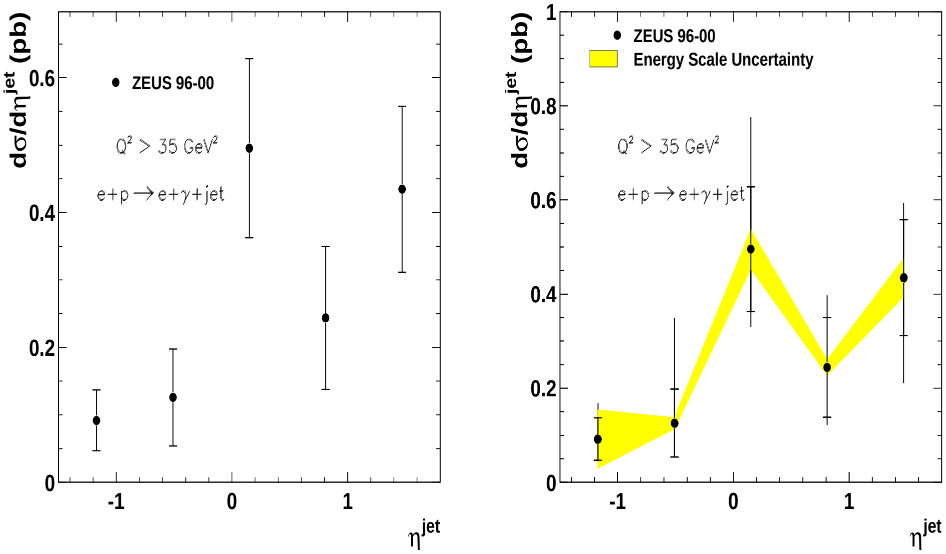

Figure 7.10: *Differential cross section, $d\sigma/d\eta^{jet}$ with a) Statistical errors only and b) Systematic uncertainties and the effect of varying the calorimeter energy scale.*

η^{jet}	$d\sigma/d\eta^{jet}(pb)$
$-1.5 < \eta^{jet} < -0.84$	$0.092 \pm 0.045^{+0.062}_{-0.019}$
$-0.84 < \eta^{jet} < -0.18$	$0.125 \pm 0.072^{+0.21}_{-0.10}$
$-0.18 < \eta^{jet} < 0.48$	$0.496 \pm 0.133^{+0.25}_{-0.10}$
$0.48 < \eta^{jet} < 1.14$	$0.244 \pm 0.106^{+0.11}_{-0.06}$
$1.14 < \eta^{jet} < 1.8$	$0.435 \pm 0.123^{+0.10}_{-0.19}$

Table 7.3: *Differential cross section for production of prompt photons accompanied by one jet, in bins of jet pseudorapidity.*

is a larger number of jets found towards the forward direction, with very few in the backwards region. As before. no obvious pattern is spotted among the systematic errors and the effect of varying the calorimeter energy scale is small and fully contained inside the statistical error bars.

The measured total cross section for production of prompt photons accompanied by one and only one jet is calculated from this differential cross section to be:

$$\sigma(ep \to e\gamma jet) = (0.92 \pm 0.15(stat.)^{+0.24}_{-0.15}(sys.))pb \tag{7.5}$$

Numerical values for this differential cross section in bins of the jet pseudorapidity are given in Table (7.3).

7.3.4 Jet Transverse Energy

The differential cross section, $d\sigma/dE_T^{jet}$ is measured for jets in the pseudorapidity range descibed previously with transverse energy, $E_T^{jet} > 6GeV$. The cross sections displayed show energies up to 16 GeV as no significant number of jets with higher energies are observed in the data, although no explicit upper limit is enforced. The measured cross sections are shown in Figure (7.11) with statistical

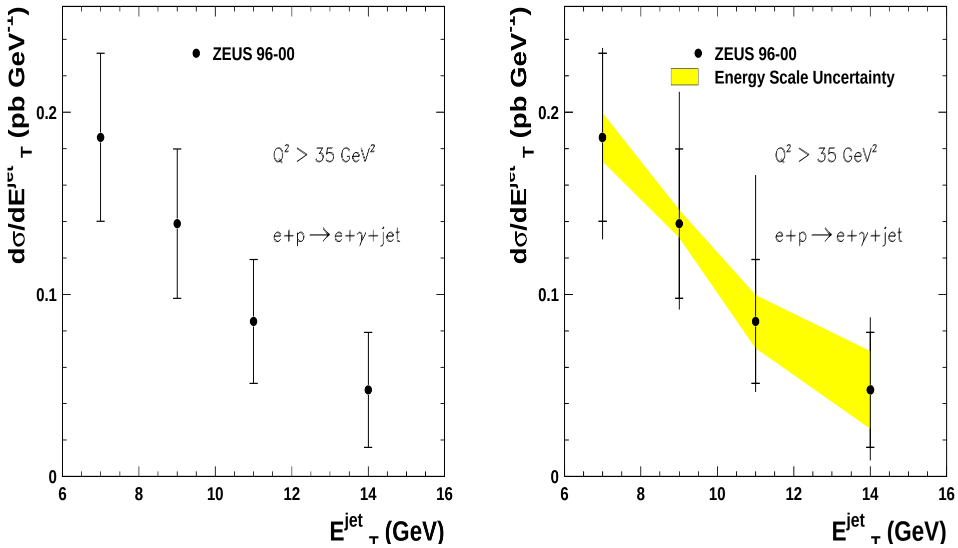

Figure 7.11: *Differential cross section, $d\sigma/dE_T^{jet}$ with a) Statistical errors only and b) Systematic uncertainties and the effect of varying the calorimeter energy scale.*

errors only and with systematic uncertainties and the effect of calorimeter energy scale variation.

From Figure (7.11), the shape of the distribution is observed to be a gently falling slope, with the number of jets found decreasing as the energy is increased. The gradient of the slope implies a reasonably hard energy spectrum. As with the previous cross sections, no pattern to the systematic uncertainties is observed and the uncertainty associated with the calorimeter energy scale is small compared to the size of the statistical errors.

The measured total cross section for production of prompt photons accompanied by one and only one jet is calculated from this differential cross section to be:

$$\sigma(ep \rightarrow e\gamma jet) = (0.82 \pm 0.14(stat.)^{+0.19}_{-0.09}(sys.))pb \qquad (7.6)$$

$E_T^{jet}(GeV)$	$d\sigma/dE_T^{jet}(pbGeV^{-1})$
$6.0 < E_T^{jet} < 8.0$	$0.186 \pm 0.046^{+0.017}_{-0.30}$
$8.0 < E_T^{jet} < 10.0$	$0.139 \pm 0.041^{+0.060}_{-0.023}$
$10.0 < E_T^{jet} < 12.0$	$0.086 \pm 0.034^{+0.072}_{-0.019}$
$12.0 < E_T^{jet} < 16.0$	$0.048 \pm 0.032^{+0.024}_{-0.022}$

Table 7.4: *Differential cross section for production of prompt photons accompanied by one jet, in bins of jet transverse energy.*

This cross section value is a little lower than those for the other cross sections, due to slight differences in background subtraction for the different plots with perhaps a small contribution from a few events which are located at energies beyond the range of plot. Although no explicit upper cut on the transverse energy of jets is imposed, less than 1% of jets are to be found in this region. This is true for both data and Monte Carlo measurements and the effect on the cross section is expected to be very small.

Numerical values for this differential cross section in bins of the jet pseudorapidity are given in Table (7.3).

7.4 Comparison to Monte Carlo Predictions

It is both interesting and informative to compare the final data measurements to the predictions of the two leading order Monte Carlo models, PYTHIA and HERWIG, previously used.

7.4.1 Absolute Predictions of Monte Carlo Models

Initially, the comparison is made to the absolute predictions of both models. These comparisons are shown in Figure (7.12).

In each distribution in Figure (7.12) it is observed that both models predict

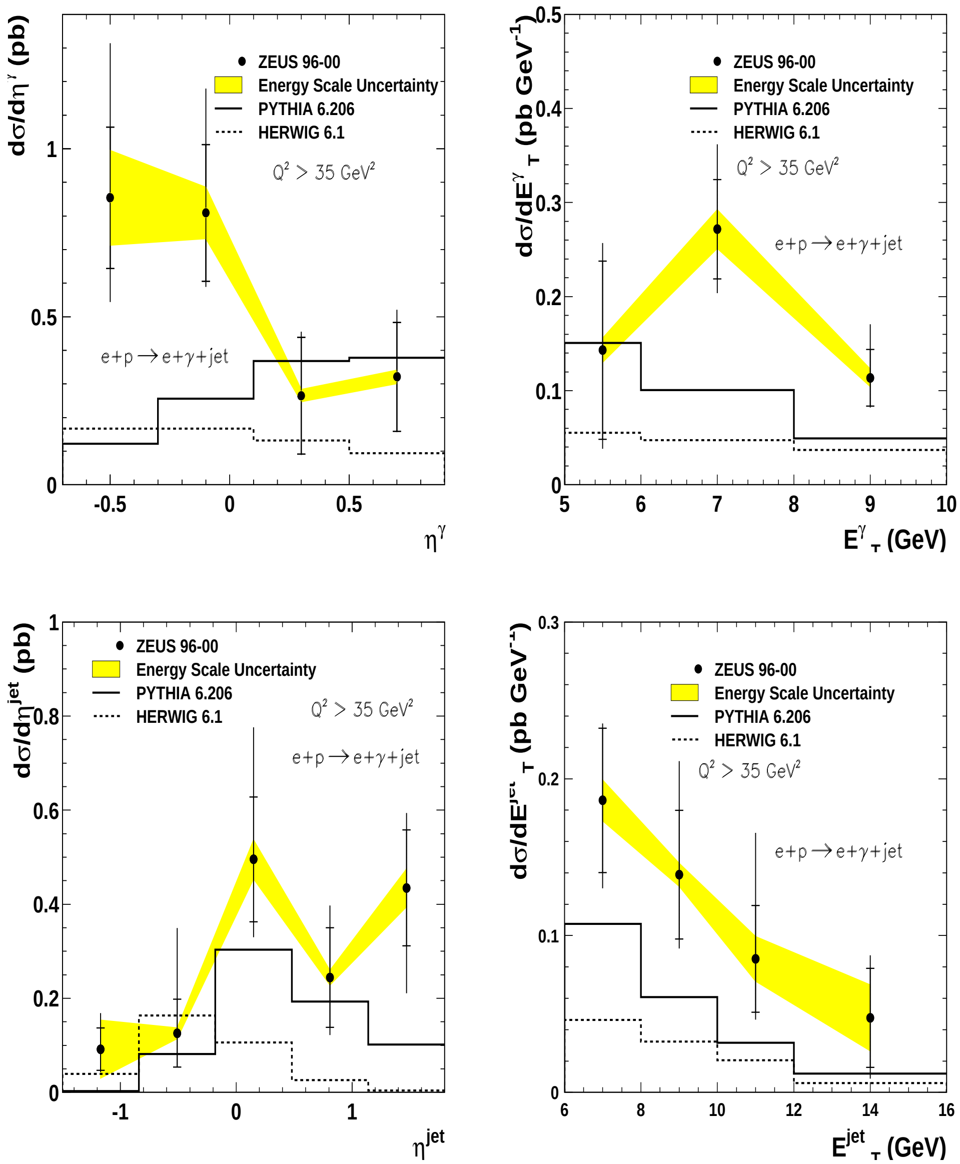

Figure 7.12: *Comparison of measuerd differential cross sections for the* $(\gamma + jet)$ *process to absolute predictions from Monte Carlo models. PYTHIA v6.206 and HERWIG v6.1 are used. The cross sections shown are, from top left a)* $d\sigma/d\eta^{\gamma}$, *b)* $d\sigma/dE_T^{\gamma}$, *c)* $d\sigma/d\eta^{jet}$ *and d)* $d\sigma/dE_T^{jet}$

a lower overall cross section than the data, with the HERWIG prediction significantly below the PYTHIA prediction. To better evaluate the shapes of the distributions, the histograms are normallised to the area of the data cross section.

The total cross section predicted by PYTHIA is $0.45pb^{-1}$ and the total cross section predicted by HERWIG is $0.22pb^{-1}$ with a value of around $0.90pb^{-1}$ for data.

7.4.2 Normalised Monte Carlo Cross Sections

The Monte Carlo curves are normalised to have the same area as the data and then comparisons to this normalised Monte Carlo distributions are made for the four $(\gamma + jet)$ differential cross sections. These comparisons provide a better idea of the success of each model in predicting distribution shapes and are shown in Figure (7.13).

It is seen that for the photon pseudorapidity distribution HERWIG does a reasonable job of reproducing the correct shape, but the prediction from PYTHIA is peaked in the wrong direction, suggesting an enhancement of prompt photon production in the forward region. Both models provide a reasonable description of the photon transverse energy distribution. Looking at the jet pseudorapidity spectrum, it is observed that HERWIG is much more strongly peaked in a backwards direction than the data. PYTHIA does a better job here. Both models do a reasonable job of describing the jet transverse energy distribution in the lower energy bins although too few jets are found in the highest bin.

7.5 Comparison to Theoretical Calculations

When the prompt photon is produced accompanied by a jet, the measured cross section can be compared to $O(\alpha^2\alpha_s)$ parton level theoretical calculations. These comparisons, which show the absolute predictions of the theory are shown in Figure (7.14).

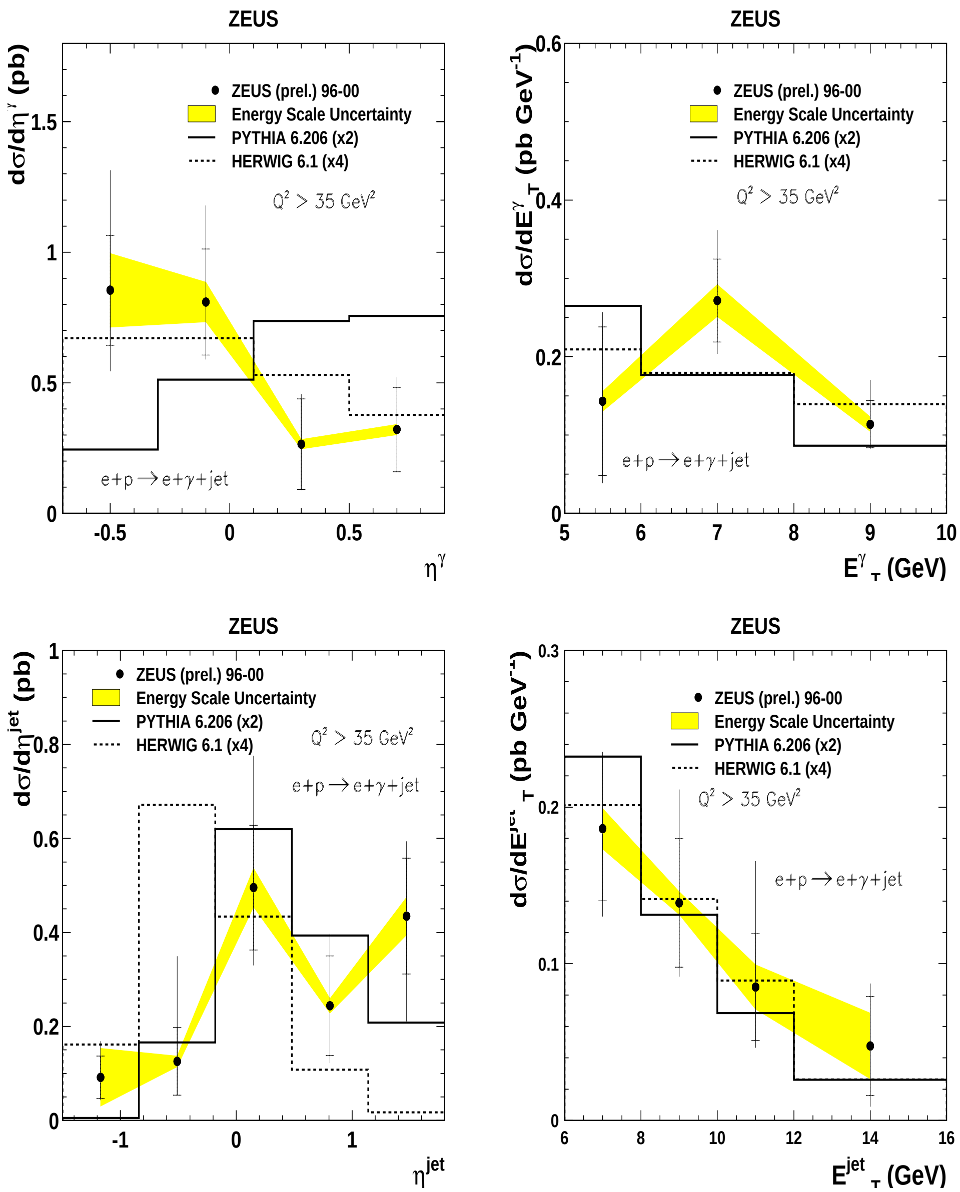

Figure 7.13: *Comparison of measuerd differential cross sections for the* $(\gamma + jet)$ *process to normalised predictions from Monte Carlo models. PYTHIA v6.206 and HERWIG v6.1 are used. The cross sections shown are, from top left a)* $d\sigma/d\eta^{\gamma}$*, b)* $d\sigma/dE_T^{\gamma}$*, c)* $d\sigma/d\eta^{jet}$ *and d)* $d\sigma/dE_T^{jet}$

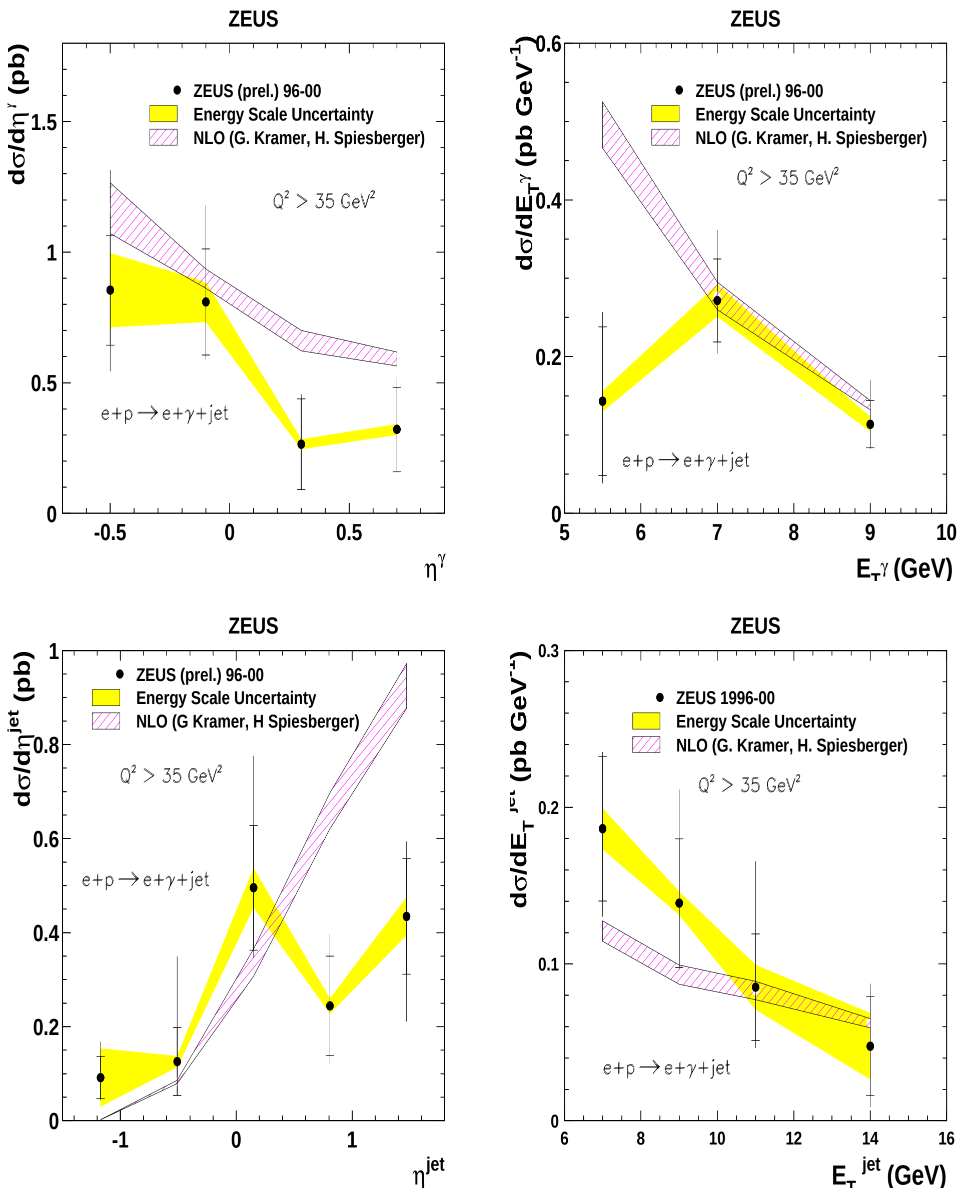

Figure 7.14: *Comparison of experimentally measured cross sections for the* $(\gamma + jet)$ *process to* $O(\alpha^2\alpha_s)$ *parton level theoretical calculations. From top, a)* $d\sigma/d\eta^\gamma$ *b)* $d\sigma/dE_T^\gamma$ *c)* $d\sigma/d\eta^{jet}$ *d)* $d\sigma/dE_T^{jet}$

It is observed in Figure (7.14) that the absolute prediction of the theoretical model is close to the value of the data without need for normalisation. In each case a similar shape is observed in both data and theory distributions. It is noted that the theoretical jets have a harder transverse energy distribution than those observed in the data and are found at higher values of E_T^{jet}. It is also observed that the theoretical prediction of the photon transverse energy is significantly higher than the data in the lowest energy bin and appears to be a more steeply falling slope.

A more detailed discussion of the results presented in this chapter and any conclusions to be drawn is found in Chapter 8.

Chapter 8

Conclusions

Prompt photon production has been observed and measured in deep inelastic electron-proton scattering for the first time. This measurement adds new information to current knowledge of prompt photon behaviour from previous studies. Both inclusive prompt photon events and prompt photons with an accompanying jet have been studied. In each case comparisons to the predictions of standard Monte Carlo models have been made. For the photon plus jet process, comparisons have been made to order $O(\alpha^2\alpha_s)$ theoretical calculations. Measurements presented here were made using a data sample of $121pb^{-1}$ of data collected using the ZEUS detector between 1996 and 2000. No distinctions were made between data collected using a positron beam and data collected using an electron beam.

The inclusive prompt photon process ($ep \rightarrow e\gamma X$) and the prompt photon + jet process ($ep \rightarrow e\gamma jet$) have been studied and differential cross sections have been produced after a subtraction of the neutral meson background. Data from running periods of different proton energies are combined and the Monte Carlo and theory curves are combined in the same ratio.

8.1 Inclusive Prompt Photon Production

8.1.1 Cross Sections

Two differential cross sections are measured for the inclusive prompt photon process, $ep \rightarrow e\gamma X$, in terms of the pseudorapidity and transverse energy of the prompt photon, $d\sigma/d\eta^{\gamma}$ and $d\sigma/dE_T^{\gamma}$. It is observed that the photon pseudorapidity spectrum shows an enhancement of prompt photon located in the rear direction. It is also observed that the transverse energy distribution is a shallow slope from low to high values.

8.1.2 Comparison to Monte Carlo Models

On comparison to the predictions of standard Monte Carlo models it is observed that the data are significantly higher than the values suggested by the Monte Carlo. As shown in Appendix A, PYTHIA gets the Q^2 and y distributions correct, showing that the underlying dynamical model may be correct. HERWIG, which gets the rapidity of the photon shape right, is wrong on Q^2 and y and further off in normalisation.

8.2 Prompt Photon + Jet Production

8.2.1 Cross Sections

Measured cross sections with respect to the photon pseudorapidity and transverse energy show similar shapes to those seen in the inclusive analysis. This is as expected as this process is a complete set within the set of inclusive events. It is seen that the photon and jet are peaked towards opposite ends of the allowed rapidity ranges.

8.2.2 Comparison to Monte Carlo Predictions

It is observed that the value of the Monte Carlo predictions for both PYTHIA and HERWIG is lower than the data, but much closer than for the inclusive process. In shape, it is seen that HERWIG predicts successfully the pseudorapidity distribution of the photon, but is incorrect in predicting the pseudorapidity spectrum of the jet. PYTHIA has almost the opposite effect, showing some success in describing the jet pseudorapidity distribution of the jet while predicting a peak for the photons in completely the opposite end of the pseudorapidity range.

8.2.3 Comparison to NLO Theory Calculations

The theoretical calculations are performed at the parton level only and include no attempt to estimate the hadronisation effects in the data. However, a comparison between data at the hadron level and theory at the parton level is still valid. Theoretical predictions show values encouragingly close to the data without the need for normalisation. The theory predicts a harder jet transverse energy spectrum, extending to higher E_T^{jet} values than the data.

8.3 Overall Conclusions

The production of prompt photons in deep inelastic lepton-proton scattering has been observed and measured for the first time. Comparisons to standard leading order Monte Carlo, PYTHIA, which uses the LUND string model, and HERWIG which uses a clustering method for hadronisation. Prompt photon events can be generated using both models. However, neither model reproduces all the relevant data distributions with complete success. Having observed that each model exhibits strength in different areas it is expected that a cross section measurement which encompasses both models in the systematic uncertainty will take account of this.

8.4 The Future

A clear prompt photon signal has been observed at HERA and it is hoped that the higher volume of data provided by the accelerator upgrade will be helpful in reducing the dominant statistical error seen in this analysis. With the availability of improved Monte Carlo models it is foreseen that a background subtraction using full event Monte Carlos rather than single particles can be successfully developed. Further investigation of other variables may yield new information on the behaviour of prompt photon events. Prompt photons are an important background to several other processes and an improvement in understanding will lead to better methods to suppress these events when desired. Work is also underway to improve the modelling of the neutral meson background for new measurements.

Appendix A

Monte Carlo

Event generators bridge the gap which exists between theoretical calculations and experimental measurements. They apply perturbation theory whenever possible and supplement this with models and parameterisation to provide a reasonably reliable estimate of the structure of an event. Event generators are programs based on Monte Carlo random number generation methods which are able to provide large samples of specific types of physics events.

Once events have been generated they are passed through the ZEUS detector and trigger simulation program, which is based on GEANT 3.13 [32]. There are thus two levels on which Monte Carlo can be considered - the hadron level which is the generated events without detector information and the detector level which is events which are intended to simulate the data as closely as possible. Events at hadron level represent the truth of the process without the migration and detector losses which invariably occur as events progress. The difference between the hadron level and the detector level is used to correct for detector effects.

The use of several types of Monte Carlo program during the execution of this analysis is necessary to obtain the final results. Monte Carlo simulations are used primarily for the five following things:

* Correction of cross sections to hadron level (Chapter 6). This is performed

with two types of Monte Carlo. PYTHIA v6.206 and HERWIG v6.1 are used to generate events containing prompt photons.

* Reconstruction of photon energy (Chapter 4). Single photon events are used for this.

* Reconstruction of hadronic jet energy (Chapter 4). Propmt photons events from PYTHIA are used for this.

* Subtraction of neutral meson background (Chapter 5). Three types of single particle Monte Carlo are needed here.

* Estimation of contamination from ISR and FSR events (Chapter 2). DJANGOH is used for this.

A.1 Prompt Photon Monte Carlo

Two standard Monte Carlo generators are employed to produce the prompt photon events which are used to correct the data cross sections to hadron level. PYTHIA [33] and HERWIG [34] are the only two generators which include explicitly the prompt photon process. The version of PYTHIA used is the most recent version, v6.206 [35] which produces prompt photon events dealing correctly with the two hard scales involved in the process. This analysis is a first measurement with low statistics, so small detector variations between 1996 and 1997 are neglected, as is the change from positrons to electrons for the 1998-99 running period. HERWIG is used as a systematic check to establish the level of dependence on the chosen Monte Carlo.

A.1.1 PYTHIA

The version of PYTHIA chosen is used because of its correct treatment of the virtual photon at the vertex and of the two hard scales present in the interaction.

	Number of Events	Cross Section (pb)
PYTHIA v6.206 (1996/97), $E_p = 820 GeV$	200,000	4.01
PYTHIA v6.206 (1998/00), $E_p = 920 GeV$	400,000	4.07

Table A.1: *Summary of PYTHIA Monte Carlo generated at $E_p = 820 GeV$. Numbers refer to events generated, before isolation cuts are applied.*

Previous versions have not done this and as a result have produced an unrealistic Q^2 distribution. Events are generated with a hard scattering subprocess of $\gamma^* + q \rightarrow \gamma + q$ within a deep inelastic electron-proton interaction. Figure (A.1) shows the process generated.

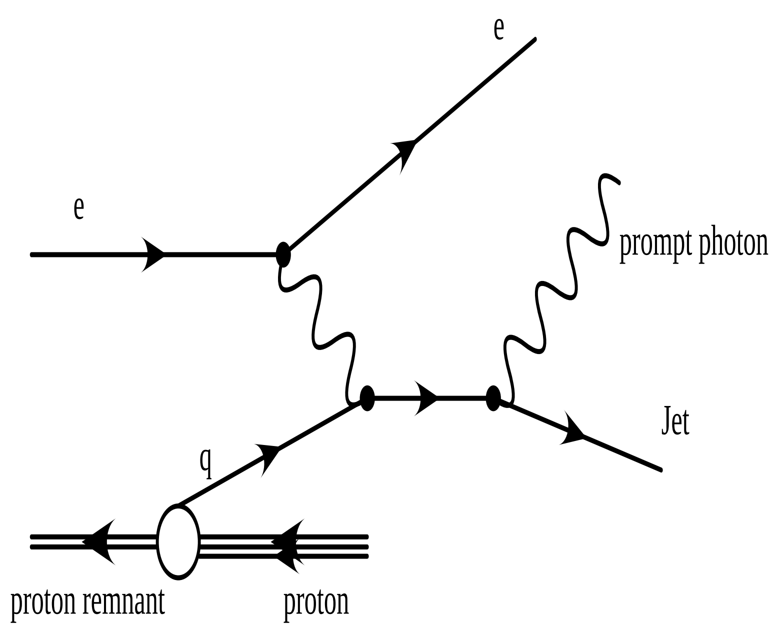

Figure A.1: *Prompt Photon process at order as modelled within PYTHIA v6.206 and HERWIG v6.1.*

A summary of the prompt photon events generated from PYTHIA can be found in Table (A.1).

It is seen from Table (A.1) that there is very little difference in the generated cross section when the proton energy is increased from 820 to 920 GeV. These quoted cross sections refer to events generated before full selection and isolation cuts have been applied.

PYTHIA Parameters

Fragmentation into hadrons within PYTHIA is performed using the LUND string model [36] as it is implemented in JETSET [37]. The Monte Carlo events are generated to provide events with $Q^2 > 35GeV^2$. No explicit restrictions on the x or y values are imposed during the generation process. Events are generated with proton energies of 820 GeV and 920 GeV and mixed in a ratio of 2:1 to reflect the proportions of ZEUS data from different running energies. Event generation is carried out using the gamma/e mode as the incoming flux and the virtual photon is factored off from the hadronic system. This allows a unified description of DIS and photoproduction.

Kinematic Control Plots

It is important to investigate how well PYTHIA events model the data before using it for acceptance correction and obtaining cross sections. Firstly, the Q^2 and $y_{electron}$ distributions which describe the event kinematics are studied. The comparison is for data after background subtraction as the Monte Carlo is pure prompt photon events. A comparison of Q^2 and $y_{electron}$ can be found in Figure (A.2).

It is observed from the plots in Figure (A.2) that PYTHIA recreates the Q^2 spectrum of the data sucessfully within the errors and shows a reasonable reproduction of the $y_{electron}$ distribution.

Prompt Photon Reproduction in PYTHIA

It is also necessary to investigate how well PYTHIA models the behaviour of the prompt photon candidates found in the data, by studying the E_T^γ and η^γ

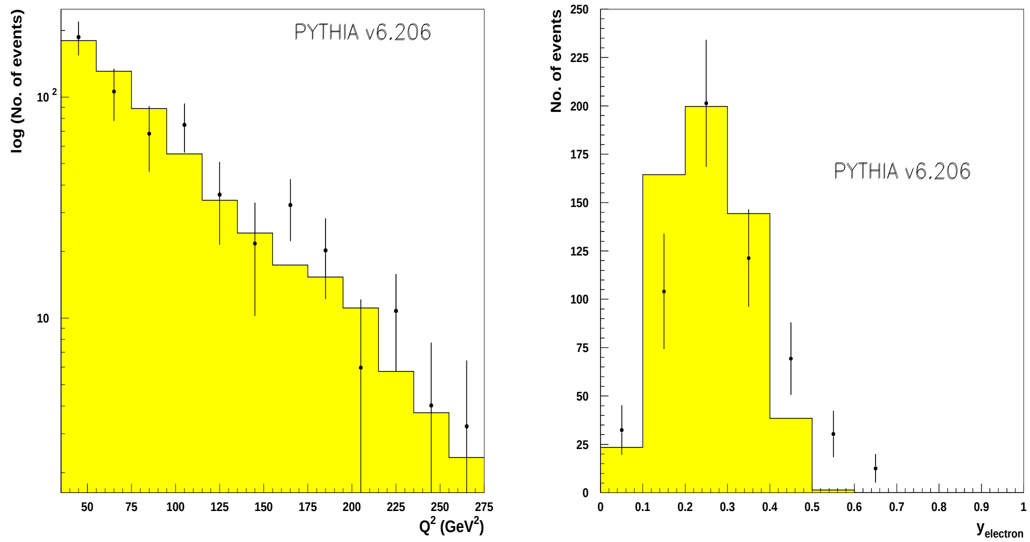

Figure A.2: *Comparison of ZEUS data and PYTHIA for a)* Q^2 *and b)* $y_{electron}$ *for the inclusive prompt photon process.*

distributions. These are shown in Figure (A.3) again for events from inclusive prompt photon process to suppress the effect of lower statistics.

It is seen in Figure (A.3) that the distinctively hard E_T spectrum of the data prompt photon is well modelled by the PYTHIA events. However, studying the η distribution it is observed that the data show an enhancement in the backward region, while the PYTHIA is essentially flat, with a slight increase in the forward direction.

Jet Control Plots

Finally, it is also important to study the reproduction of jet variables in the PYTHIA event description. As with the photon the study is restricted to E_T^{jet} and η^{jet}. Figure (A.4) shows the comparison, using in this case $(\gamma + jet)$ events to supply the jet information.

It is observed in Figure (A.4) that the description of the jet transverse energy is

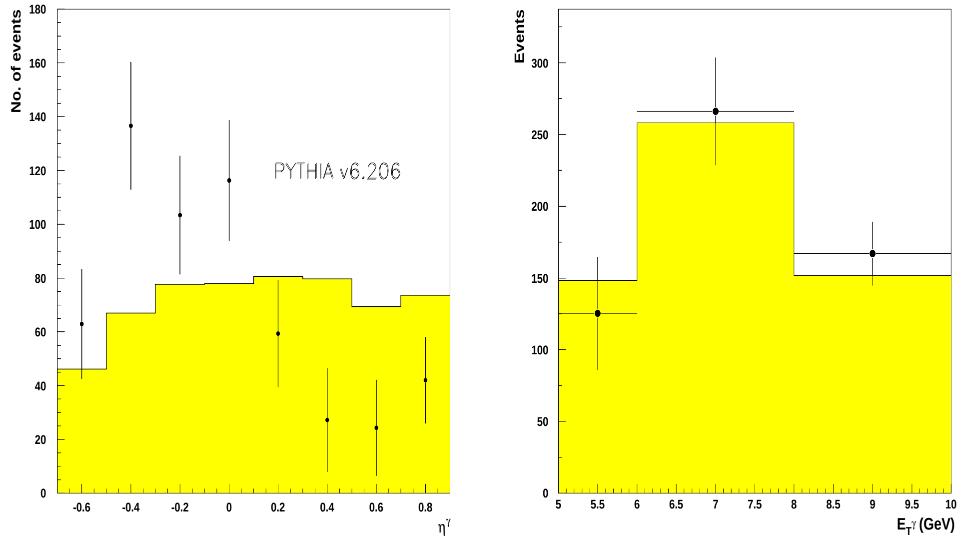

Figure A.3: *Control plots of a) E_T^γ and b) η^γ showing the behaviour of PYTHIA prompt photon events and comparison to ZEUS data.*

slightly lower than the data at low energy values and the pseudorapidity spectrum is not peaked so strongly forward as in the data.

A.1.2 HERWIG

As the PYTHIA distribution for the photon pseudorapidity does not provide a complete description of data, it is necessary to look at a second Monte Carlo to provide an estimate of the model dependence of the final cross section. Direct prompt photon production is also available in HERWIG but no other standard generators.

The summary of the HERWIG Monte Carlo production is given in Table (A.2)

From Table (A.2), it is again seen that the increase in proton energy between the two running periods has only a small effect on the cross section generated.

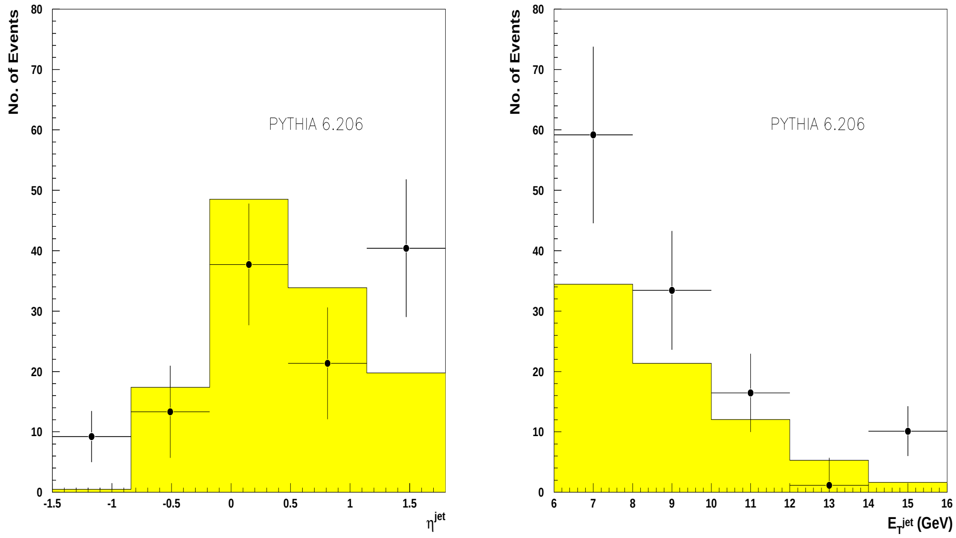

Figure A.4: *Control plots of a) E_T^{jet} and b)η^{jet} showing the behaviour of jets within PYTHIA in comparison to ZEUS data.*

	No. of Events	σ (pb)
HERWIG 6.1 (1996/97), $E_p = 820GeV$	100,000	15.40
HERWIG 6.1 (1998/00), $E_p = 920GeV$	200,000	15.95

Table A.2: *Summary of HERWIG Monte Carlo prompt photon events generated.*

HERWIG Parameters

As with PYTHIA, HERWIG events are generated with no restrictions on x or y and to provide events with $Q^2 > 35GeV^2$. Events are generated at both relevant proton energies, 820 GeV and 920 GeV. Fragmentation into hadrons within HERWIG is implemented using a cluster model [38].

Kinematic Control Plots

As with PYTHIA, the distributions of Q^2 and $y_{electron}$ show well HERWIG reproduces the event structure, in particular the success of the description of the

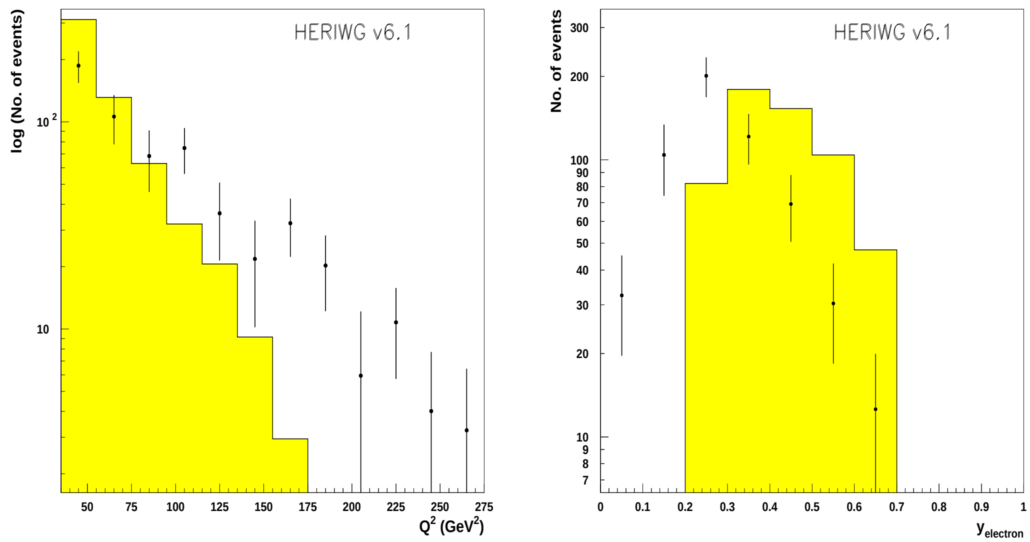

Figure A.5: *Comparison of HERWIG and ZEUS data for a)* Q^2 *and b)* $y_{electron}$

general event kinematics. These comparisons are given in Figure (A.5).

Immediately, from Figure (A.5), it is obvious that HERWIG fails to show the correct distribution shape. The curve is much more steeply falling, with a lack of events at higher Q^2 which are present in the data. Looking at the distribution of $y_{electron}$ it can be observed that the HERWIG plot is offset to the right of the data and the agreement is significantly poorer than for PYTHIA.

Prompt Photon Reconstruction in HERWIG

It is also necessary to look at the photon dependent distributions, specifically the transverse energy and pseudorapidity to establish the comparison with data and with PYTHIA. This is shown in Figure (A.6), again using inclusive prompt photon events.

It is seen in Figure (A.6) that there is little difference in the behaviour of the photon transverse energy distribution for both Monte Carlos. However it is observed that HERWIG produces a better fit to the photon pseudorapidity

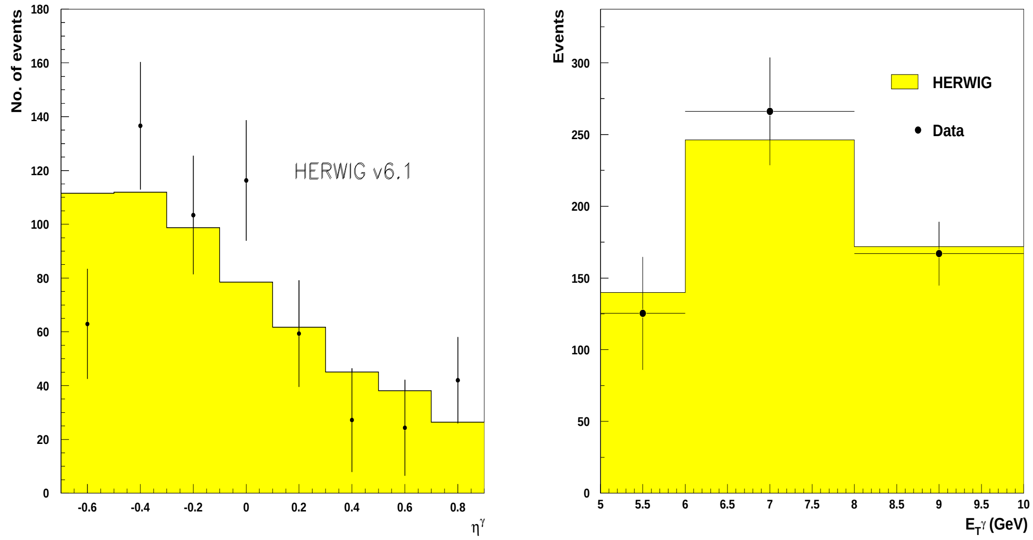

Figure A.6: *HERWIG control plots of photon parameters. a)*η^{γ} *and b)*E_T^{γ}

spectrum, showing an enhancement in the rear direction.

Jet Reconstruction in HERWIG

Finally, the same jet variables of transverse energy and pseudorapidity are comapred to the HERWIG prediction. These comparisons are displayed in Figure (A.7).

Figure (A.7) shows that the η^{jet} distribution shows a clear peak towards the central rapidity region and does not describe the data well. The E_T^{jet} plot has a similar appearance to that for PYTHIA although the difference at low E_T is slightly larger.

A.1.3 Summary - Prompt Photon Monte Carlo

It has been found that both PYTHIA and HERWIG do a reasonable job of reproducing the important data distributions, differing from each other in the level of their agreement for a few key plots. Overall, it is thought that PYTHIA performs slightly better and should be usd to carry out the acceptance correction

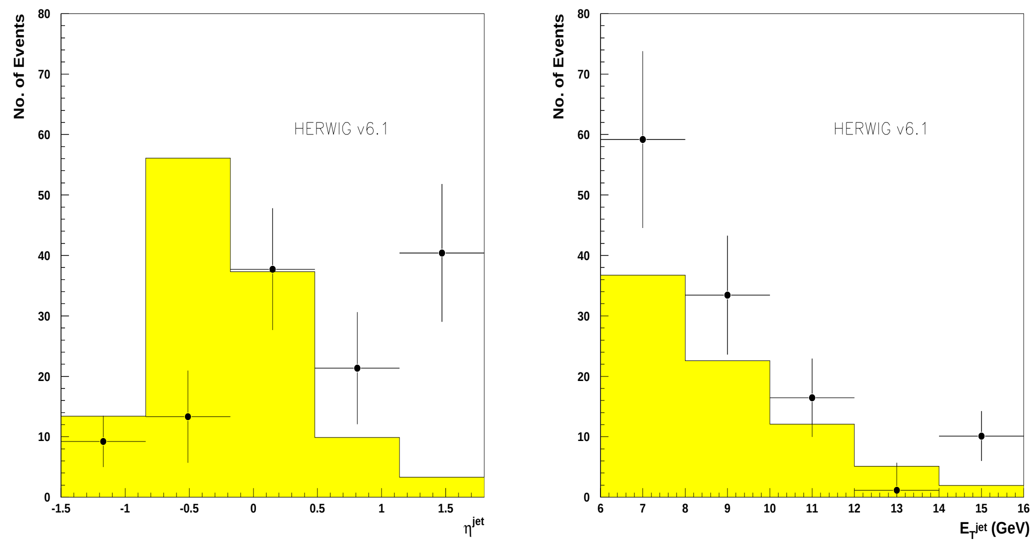

Figure A.7: *HERWIG control plots of jet parameters. a)*η^γ *and b)*E_T^γ

to hadron level, but that using HERWIG as a systematic uncertainty will provide in the end a systematic error bar which encompasses the full range of Monte Carlo agreement which exists. It is clear that neither Monte Carlo model is completely adequate in reproduing the data and that a theoretical model should be considered.

A.2 Single Particle Monte Carlo

A neutral meson background to the prompt photon candidates is fitted using single photon events with a combination of the most likely background particles. It was discovered that there was no significant difference between single particle events processed with a 1997 detector configuration and those with a 1998 detector configuration so for simplicity only one type is used. A summary of the single particle events used is given in Table (A.3)

The E_T distribution of the single particle events is reweighted according to

Particle Type	No. of Events	E_T distribution
γ	100,000	Flat, $3 < E_T < 20$ GeV
π^0	100,000	Flat, $3 < E_T < 20$ GeV
η	100,000	Flat, $3 < E_T < 20$ GeV

Table A.3: *Summary of Single Particle Monte Carlo used for neutral meson background subtraction.*

the data distribution in the region corresponding to each particle type.

A.3 DJANGOH

DJANGOH [39, 40, 41] events are used to simulate the behaviour of initial and final state radiated photons within standard neutral current DIS events. Feynman diagrams of the radiative processes generated are shown in Figure (A.8).

In total, 100,000 DJANGOH events were generated with $Q^2 > 35 GeV^2$. A summary of the initial and final state radiative events produced is given in Table (A.4).

Process Type	No. of Events	Cross Section (nb)
ISR	31409	11.6
FSR	19582	7.5

Table A.4: *Summary of Initial- and Final State Radiation Events generated using DJANGOH.*

The cross sections for these radiative processes are large compared to the prompt photon process. However, when selection cuts used in analysis are applied to these events, none survive.

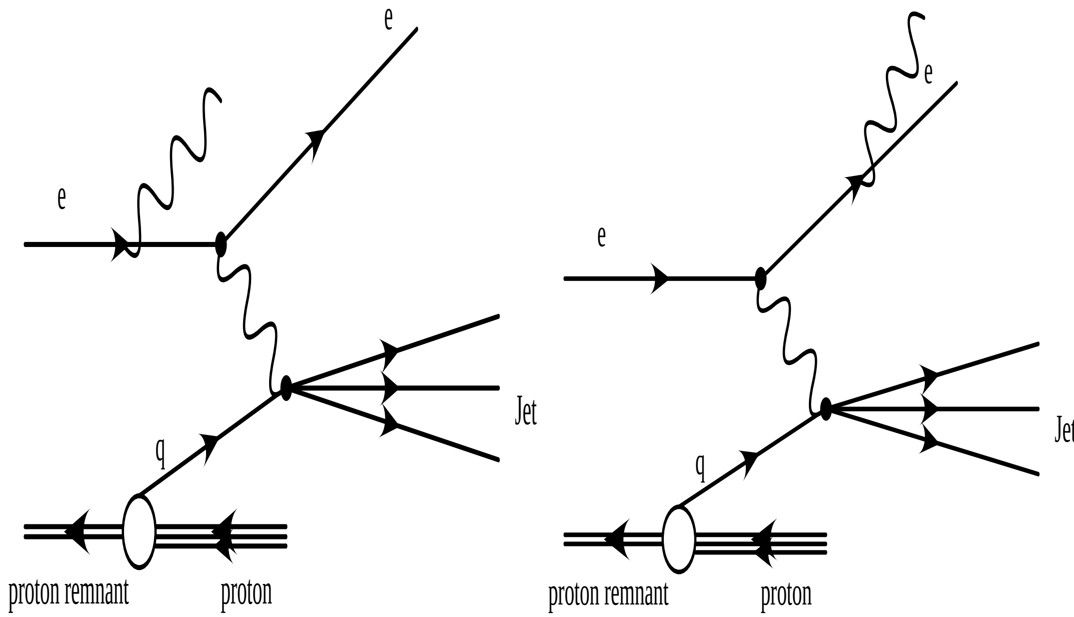

Figure A.8: *Photons produced from a) the incoming electron line and b) the scattered electron line in NC DIS events*

Bibliography

[1] CDF Coll., F. Abe et al., Phys. Rev. Lett. 73 2662 (1994).

[2] CDF Coll., F. Abe et al., *Properties of Photon Plus Two Jet Events in PP Collisions at* $\sqrt{s} = 18.$ *TeV* FERMILAB-PUB-97-106-E, Phys. Rev. **D57** 67 (1998).

[3] CDF Coll., F. Abe et al., *The Jet Pseudorapidity Distribution in Direct Photon Events in PP Collisions at* $\sqrt{s} = 1.8$ *TeV* FERMILAB-PUB-98-009-E, Phys. Rev. **D57** 1359 (1998).

[4] D0 Coll., *The Isolated Photon Cross Section in the Central and Forward Rapidity Region in PP Collisions at* $\sqrt{s} = 1.8$ *TeV* FERMILAB-PUB-96/072-E, Phys. Rev. Letters 77 5011 (1996)

[5] D0 Coll., *The Isolated Photon Cross Section in PP Collisions at* $\sqrt{s} = 1.8$ *TeV* FERMILAB-PUB-99/1354-E, Phys. Rev. Lett. 81 2786 (2000).

[6] J. Jalilian-Marian, K. Orginos and I. Sarcevic *Prompt Photons at RHIC*, hep-ph/0010230v2 October 2000

[7] A. Bazilevsky for the PHENIX Coll. *Prompt Photon yield and Background Study in PHENIX at RHIC*, RIKEN Review No. 28 (May 2000)

[8] ZEUS Coll., J. Breitweg et al., *Observation of isolated high-Et photons in photoproduction at HERA*. Phys. Lett. **B 413**, 201 (1997), hep-ex/9708038.

[9] ZEUS Coll., J. Breitweg et al., *Measurement of inclusive prompt photon photoproduction at HERA*. Phys. Lett. **B 472**, 175 (2000), hep-ex/9910045.

[10] ZEUS Coll., S. Chekanov et al., *Study of the effective transverse momentum of partons in the proton using prompt photons in photoproduction at HERA.* Phys. Lett. **B 511**, 19 (2001), hep-ex/0104001.

[11] H1 Coll. *Inclusive Prompt Photon Production at HERA*, Conference Paper 1007, ICHEP 2002, Amsterdam.

[12] A. Gehrmann-De Ridder, G. Kramer and H. Spiesberger, *Photon plus jet cross sections in deep inelastic ep collisions at order* $O(\alpha^2\alpha_s)$. Nucl. Phys. **B 578**, 326 (2000).

[13] G. Kramer and H. Spiesberger, private communication (2002).

[14] ZEUS Collaboration, *The ZEUS Detector, Status Report 1993*, DESY (1993).

[15] N. Harnew et al., *Vertex triggering using time difference measurements in the ZEUS central tracking detector.* Nucl. Inst. Meth. **A 279**, 290 (1989);

[16] B. Foster et al., *The performance of the ZEUS central tracking detector z-by-timing electronics in a transputer based data acquisition system.* Nucl. Phys. Proc. Suppl. **B 32**, 181 (1993);

[17] B. Foster et al., *The design and construction of the ZEUS central tracking detector.* Nucl. Inst. Meth. **A 338**, 254 (1994).

[18] A. Andresen et al., *Construction and beam test of the ZEUS forward and rear calorimeter.* Nucl. Inst. Meth. **A 309**, 101 (1991); A. Caldwell et al., *Design and implementation of a high-precision readout system for the ZEUS calorimeter.* Nucl. Inst. Meth. **A 321**, 356 (1992); A. Bernstein et al., *Beam tests of the ZEUS barrel calorimeter.* Nucl. Inst. Meth. **A 336**, 23 (1993).

[19] M. Derrick et al., *Design and construction of the ZEUS barrel calorimeter.* Nucl. Inst. Meth. **A 309**, 77 (1991);

[20] D.Kisielewaska et al., *Fast Luminosity Monitoring at HERA*, DESY - HERA Report 85-25.

[21] L.A.T. Bauerdick, A. Fox-Murphy, T. Haas, S. Stonjek and E. Tassi *Event Indexing Systems for Efficient Selection and Analysis of HERA Data*, DESY01-045; www-zeus.desy.de/ZEUS_ONLY/analysis/zes/index.html

[22] www.objectivity.com

[23] ZEUS Collab., S.Chekanov et al. *Measurement of the neutral current cross-section and F_2 structure function for deep inelastic e^+p scattering at HERA.* Eur. Phys. J. **C 21**, 443 (2001). hep-ex/0105090.

[24] H. Abramowicz, A. Caldwell and R. Sinkus *Neural Network based electron identification in the ZEUS calorimeter* Nucl. Inst. Meth. **A 365**, 508 (1995).

[25] J. Repond, An electron finding routine, included in the ZEUS PHANTOM library.

[26] LAZE (Look At Zeus Events) is an event display for ZEUS analysis that specialises on two-dimensional projections, most of which one cannot get by a simple geometrical projection from the three-dimensional representation.

[27] P.J. Bussey, A jet finding algorithm, included in the ZEUS PHANTOM library.

[28] J. Huth et al. in proceedins of the Summer School on High Energy Physics, Snowmass 1990

[29] P. Bussey, S. Lee and K. Umemori *Prompt photon measurements in photoproduction at HERA (accompanying notes)* ZEUS Note 99-046.

[30] S. Lee *Prompt Photons in Photoproduction* Thesis, 2000

[31] D.E. Groom et al. (Particle Data Group), Eur. Phys. Jour. **C15**, 1 (2000)

[32] R. Brun et al., GEANT3, Technical Report CERN-DD/EE/84-1, CERN, 1987.

[33] T. Sjostrand, *High-energy physics event generation with* PYTHIA 5.7 *and* JETSET 7.4. Comp. Phys. Comm. **82**, 74 (1994).

[34] G. Marchesini et al., HERWIG: A MONTE CARLO EVENT GENERATOR FOR SIMULATING HADRON EMISSION REACTIONS WITH INTERFERING GLUONS. Comp. Phys.Comm. **67**, 465 (1992).

[35] T. Sjostrand, private communication, 2002.

[36] B. Andersson et al., *Parton fragmentation and string dynamics.* Phys. Rep. **97**, 31 (1983).

[37] T. Sjostrand, *The Lund Monte Carlo for jet fragmentation and e^+e^- physics:* JETSET VERSION 6.2 Comp. Phys. Comm. **39**, 347 (1986); T. Sjostrand and M. Bengtsson, *The Lund Monte Carlo for jet fragmentation and e^+e^- physics:* JETSET *An update.* Comp. Phys. Comm. **43**, 367 (1987).

[38] B. R. Webber, *A qcd model for jet fragmentation including soft gluon interference.* Nucl. Phys. **B 238**, 492 (1984).

[39] K. Charchul, G.A. Shuler and H. Spiesberger, *Combined QED and QCD radiative effects in deep inelastic lepton-proton scattering: The Monte Carlo generator DJANGO6.* Comp. Phys. **81**, 381 (1994).

[40] A. Kwiatkowski, H. Spiesberger and H.J. Mohring, HERACLES*: An event generator for ep interactions at HERA energies including radiative processes (version 1.0).* Comp. Phys. Comm. **69**, 155 (1992). Also in *Proc. Workshop Physics at HERA*, 1991, DESY, Hamburg.

[41] G. Ingelman, A. Edin and J. Rathsman, LEPTO 6.5*: A Monte Carlo generator for deep inelastic lepton-nucleon scattering.* Copm. Phys. Comm. **101**, 108 (1997).